MEASUREMENT OF VERY SLOW FLOWS IN ENVIRONMENTAL ENGINEERING

Thesis submitted

in fulfillment of the requirements for the degree of

Doctor of Philosophy

by Andrew Skinner

Faculty of Engineering, Computer and Mathematical Sciences

School of Civil, Environmental and Mining Engineering

The University of Adelaide, North Terrace Campus

South Australia

December 2009

Measurement of Very Slow Flows in Environmental Engineering

By: Andrew John Skinner

B.Tech., M.Eng. (Electronic Engineering), FIEAust., CPEng

Thesis submitted in fulfillment of the requirements for the degree of Doctor of Philosophy

LIBRARY COPY after examination

Faculty of Engineering, Computer and Mathematical Sciences
School of Civil Environmental and Mining Engineering
The University of Adelaide SA 5005 Australia

Correspondence to: -
Andrew Skinner
Engineering Director
Measurement Engineering Australia
41 Vine Street
PO Box 476
MAGILL, South Australia 5072
Telephone: +61 8 8332 9044
Facsimile: +61 8 8332 9577
Web: www.mea.com.au
Email: andrew.skinner@mea.com.au

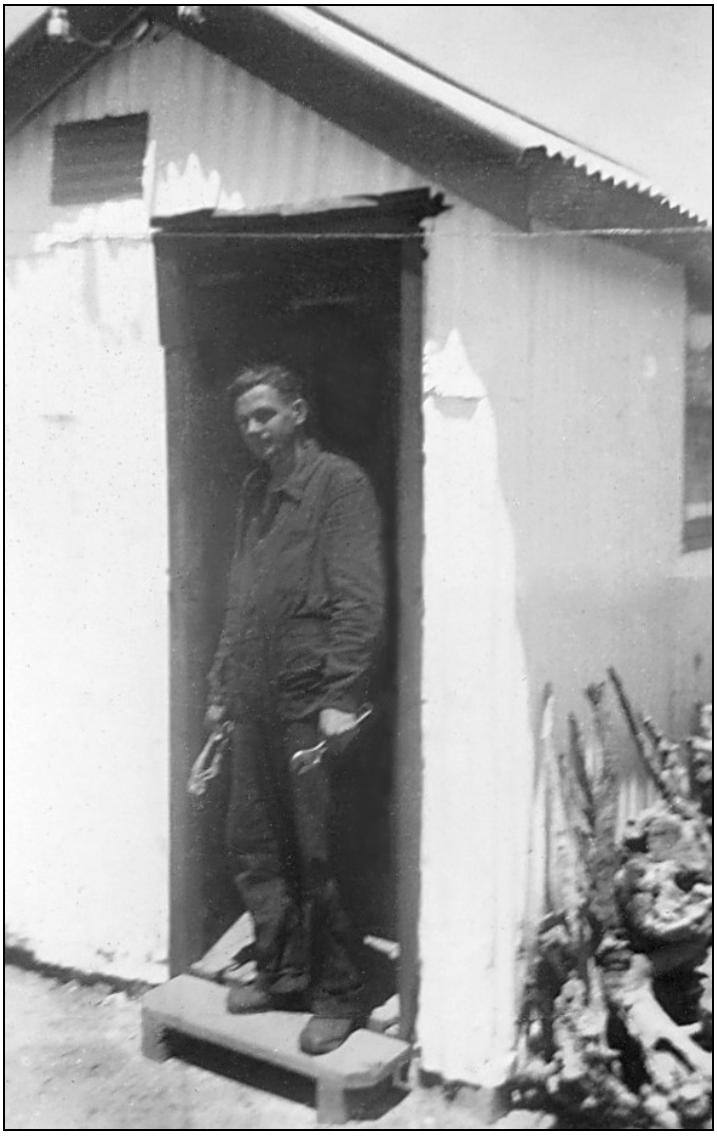

I dedicate this thesis to my father

John Francis Skinner

24th September 1923 – 3rd March 1983

who left school after Grade 7 to train in the hard school of engineering
in a country garage in the Western Australian wheat-belt town of Merredin.

He went on to build up a highly-regarded ‘custom engineering’ firm
capable of building specialist machines for industry and universities.

Sadly, he never lived to see his eldest son do the same in the field of
measurement engineering.

He left me the skill in my hands,
an imagination tuned for building gadgetry
and the sense that with hard work anything is possible.

Table of contents

MEASUREMENT OF VERY SLOW FLOWS IN ENVIRONMENTAL ENGINEERING..... I

TABLE OF CONTENTS IV

TABLE OF FIGURES.....VI

STATEMENT X

ACKNOWLEDGMENTS XI

ABSTRACT 1

CHAPTER 1. INTRODUCTION 5

CHAPTER 2. LITERATURE REVIEW 11

2.1 VERY SLOW FLOWS IN STRATIFIED LAKES 12
2.2 'RATE-OF-HEAT LOSS' FLOW METERS IN THE LITERATURE 14
2.2.1 Thermistor flow meters in the literature 15
2.2.2 The most basic thermistor flow meter 17
2.2.3 A simple temperature-compensated thermistor flow meter 17
2.2.4 An effective temperature-compensated thermistor flow meter 18
2.2.5 The LaBarbera and Vogel bridge 19
2.2.6 The Yang et al bridge 21
2.2.7 Digital thermistor bridge circuits 22
2.2.8 A transient response thermal flow sensor using intertwined PRTDs 23
2.2.9 A thermal gas-flow sensor using the digital oscillator technique 24
2.3 'TEMPERATURE RISE' OR 'THERMAL-FIELD DISTORTION' FLOW METERS 24
2.4 'TIME-OF-FLIGHT' THERMAL FLOW METERS 27
2.5 SUMMARY OF LITERATURE REVIEW FINDINGS 27
2.5.1 Thermistor resistance-temperature characteristics 27
2.5.2 The limitations of analog thermistor bridge flow meters 29
2.5.3 Thermistor flow meters for very slow flows 30
2.5.4 The problem of buoyancy in 'Rate of Heat Loss' sensors in open water bodies..... 32
2.5.5 Future directions from the literature 32

CHAPTER 3. USING SMART SENSOR STRINGS FOR CONTINUOUS MONITORING OF TEMPERATURE STRATIFICATION IN LARGE WATER BODIES..... 37

3.1 BACKGROUND 37
3.1.1 Development of a new SFVC ADC for sensors 38
3.1.2 The AD652 Synchronous Voltage-to-Frequency Converter: Product Description 39
3.1.3 An early SVFC thermistor ADC design 41
3.1.4 Development of an integrated temperature sensor 43
3.1.5 Use of 'standard curves' for linearizing non-linear sensor response 45
3.1.6 Improving sensor resolution and linearity 46

CHAPTER 4. AN AUTOMATIC SOIL PORE-WATER SALINITY SENSOR BASED ON A WETTING FRONT DETECTOR..... 51

4.1 BACKGROUND 51
4.1.1 Extending the ADC form to differential and AC excitation measurements..... 52

CHAPTER 5. A LOG-ANTILOG ANALOG CONTROL CIRCUIT FOR CONSTANT-POWER WARM-THERMISTOR SENSORS – APPLICATION TO PLANT WATER STATUS MEASUREMENT 59

5.1 BACKGROUND 59
5.1.1 Generating constant-power in a thermistor flow meter 61
5.1.2 The dual element heat source: thermilinear thermistor devices 63
5.1.3 The switched heat source 67
5.1.4 The dual current heat source 69
5.1.5 A switched bridge constant-power thermistor flow meter..... 70
5.1.6 An inverse square root circuit using analog hardware multipliers 76

5.1.7 Solving the inverse square-root function using digital multipliers ... *77*
5.1.8 A log-antilog inverse square-root circuit ... *78*

CHAPTER 6. EVALUATION OF A WARM-THERMISTOR FLOW SENSOR FOR USE IN AUTOMATIC SEEPAGE METERS ... **81**

6.1 BACKGROUND ... 81
6.1.1 Motivation for the development of a groundwater seepage meter ... *83*
6.1.2 Expanded Proof of the Varying Head Flow Controller ... *84*
6.1.3 'Plunging flow calibrator' control circuit ... *85*
6.1.4 The workbench… ... *88*
6.1.6 Transient flow calibration apparatus ... *89*
6.1.7 Flow transition from laminar to turbulent in the control pipe ... *91*

CHAPTER 7. A NULL-BUOYANCY THERMAL FLOW METER: APPLICATION TO THE MEASUREMENT OF THE HYDRAULIC CONDUCTIVITY OF SOILS ... **95**

7.1 BACKGROUND ... 95
7.1.1 Seepage meters and mechanical valves ... *95*
7.1.2 Buoyant plumes under downward flow conditions ... *97*
7.1.3 Flows in the landscape – 'hydraulic conductivity' and drainage meters ... *98*
7.1.4 Permeameters and the measurement of hydraulic conductivity ... *103*
7.1.5 Early results: problems with thermal stratification in the test rig ... *105*
7.1.6 Reducing thermal background temperatures ... *106*
7.1.7 Flow instability ... *107*
7.1.8 Plume stability ... *108*

CHAPTER 8. CONCLUSIONS AND FUTURE WORK ... **113**

CHAPTER 9. REFERENCES ... **119**

APPENDIX A: SELECTED FIELD DATA FROM TEMPERATURE SENSOR STRINGS ... **133**

APPENDIX B: BINARY LOGARITHMS FOR SOLVING THE STEINHART-HART EQUATION ... **139**

B1. Natural and binary logarithms ... *139*
B2. Deriving binary logarithms in a microcontroller ... *141*
B3. Approximating the binary logarithm with a simple arithmetic function ... *143*
B4. Solving for error terms in the Simple logarithm ... *144*
B5. Using a look-up table to reduce errors in the Simple logarithm ... *145*

APPENDIX C: THERMISTOR FORMULAE IN EXCEL SPREADSHEETS ... **149**

APPENDIX D: FAILURE OF MONOTONICITY IN THE ADC ... **151**

APPENDIX E: SAP FLOW BIBLIOGRAPHY ... **155**

Table of Figures

Figure 1 A simple constant-temperature hot wire/hot film anemometer, using an adjustable resistance to force a constant temperature onto the hot wire as described by Lomas (1986) and reproduced from Sheldrake (1995). Setting the variable resistance R_3 to a particular value forces the control loop to adjust the bridge voltage to impress a voltage across the hot-wire R_W, thus raising it to a constant temperature as it dissipates power. The bridge voltage E is the output signal, and varies as the fluid flow rate changes the rate-of-heat loss from the sensor element. 15
Figure 2 The simplest possible method of creating a warm thermistor flow meter, adapted from Molina, Victoria and Ibanez (1994). The voltage regulator impresses a DC voltage across the thermistor and the ammeter measures the current flow to ground as a flow-dependent signal. This method is dependent upon isothermal fluid temperature. 17
Figure 3 The Vogel (1969) warm thermistor flow meter 18
Figure 4 The Riedl and Machan (1972) Bridge Flowmeter. These early flow-monitoring bridge circuits were always in self-heating mode, and were unable to report on the temperature of either the water or the heated thermistor. Instead, their output was proportional to power dissipated by the self-heated thermistor. R_1=100Ω (adjustable), *R2*=1500Ω, *R3*=1200Ω, *T1*=100Ω thermistor, *T2*=1000Ω thermistor, *T1*=3000Ω thermistor at 25°C 19
Figure 5 The LaBarbera and Vogel (1976) bridge. A and B are the flow meter with voltage-to-frequency converter C and frequency-to-voltage converter D 20
Figure 6 The active-bridge flowmeter of Yang, Kummel and Soeberg (1988). R_m is the measurement thermistor and R_r is the reference thermistor 21
Figure 7 Pulsed thermistor bridge of Briggs-Smith and Piscitelli (1981) 23
Figure 8 Pulsed double-PRTD thermal flow meter of Sonnenschmidt and Vaneslow (1996). The double PT100 on the left has dimensions in millimetres. The wires are two intertwined spirals of the same diameter. 24
Figure 9 Industrial thermal flow meter of the type described by Baker (1995) 25
Figure 10 Thomas flow meter, with a heating element inside the pipe and thermocouples used to measure the induced temperature gradient. From Baker (1995) 25
Figure 11 The Laub flow meter placed the heating and sensor coils on the outside of the pipe for safety reasons. From Baker (1995) 25
Figure 12 Monolithic flow sensor of Yang and Soeberg (1992) – circuit and physical layouts – operating in transit-time flow mode 26
Figure 13 Resistance versus temperature response of a 1kΩ@25°C NTC thermistor measured with a 10μA excitation current 28
Figure 14 Error curves for the Rield-Machan Bridge over the limited temperature range of 5°C to 35°C for a mixture of commercial thermistor values *T1*, *T2* and *T3* with optimal fixed resistor values in *R1*, *R2* and *R3*. 29
Figure 15 Lewis (on the left) of the University of Adelaide installing an early raft-based stratification system in the Myponga Reservoir in South Australia. The multi-channel ADC electronics is installed in the enclosure at the rear of the raft. The multiple individual thermistors can be seen hanging over the front of the raft (white cables). 38
Figure 16 The AD652 Monolithic Synchronous Voltage-to-Frequency Converter used as the basis for the development of a new type of charge-balance ADC for environmental sensors. 40
Figure 17 An early SVFC thermistor ADC design. It is essentially a buffered voltage divider network followed by an active-low SVFC ADC formed by the integrator and comparator. V_{ref} is 1.23V and is derived ratiometrically from the LM2951 +5V regulator powering the thermistor divider, the comparator reference and the microcontroller. This design was used with remote thermistors on the end of a two-wire cable, often up to 30m from the ADC located in an enclosure on a surface raft as in Figure 15 or on a wooden pole driven into the sediment. 42
Figure 18 The remote thermistor of Figure 17 – submersed in the water column - was almost always operating at a different temperature to the electronics on the surface raft. This necessitated a separate measurement of the temperature of the ADC electronics. This was accomplished by this parallel ADC channel using a PNP diode-connected bipolar transistor as a temperature sensor. Small changes in the thermal voltage *kT/q* of the transistor's base-emitter voltage due to temperature fluctuations changed the input current of the ADC and hence its *count* output. This particular circuit gave rise to the possibility of a ground-referred thermistor in place of the PNP+R_{in} combination to measure temperature in an isothermal environment created by potting the ADC, thermistor, 5V regulator and microcontroller in close proximity. This reduced the difficulties in finding a convergent solution to the 7-parameter calibration associated with this separate temperature measurement solution. 42
Figure 19 Twenty-four sensor circuit boards are shown before being broken-out from the PCB panel form in which they are manufactured. They are shown linked by ribbon cable (top) to power, program and test them prior to encapsulation. They are then potted inside a threaded PVC tube with a cable-gland and

O-ring at each end. A heavy-walled adhesive heatshrink is then shrunk over the whole assembly to form a third level of waterproofing (bottom). 44
Figure 20. The 'count versus temperature' transfer functions of 26 randomly selected production sensors all follow the same basic curvature. Applying small offset and gain terms to each curve matches all sensors over the operating temperature range to within ±0.006°C, while effectively linearizing the calibration process. 45
Figure 21 A sensor string bundled together for two-point in-field calibration at the Torrens Lake in Adelaide South Australia 47
Figure 22 A 15-bit integrated thermistor temperature charge-balance ADC, published in IEEE Sensors in December 2006 48
Figure 23 An improved 16-bit integrated thermistor temperature charge-balance ADC, developed and field tested extensively after the original sensor was published in IEEE Sensors in December 2006. The separation of the op-amp and comparator (previously in a single 8-pin DIP package) resolved issues with 'flat-spots' in the temperature response curves due to internal IC feedback problems on the shared supply pin at harmonics of the SVFC clock, as explained in Appendix D 49
Figure 24 The Murray-Darling Basin in south-eastern Australia covers 14% of the county's total land area and is home to 11% of the Australian population. The Darling (2740km), Murray (2530km) and Murrumbidgee (1690km) are Australia's three longest rivers. 52
Figure 25 A 16-bit charge-balance ADC for platinum resistance temperature measurement. The bias current generator injects a 1mA current into the PRTD to offset the 1kΩ (0°C) baseline resistance of the PRTD; the ADC only responds to differential resistances above this value in the temperature range 0°C to 50°C 53
Figure 26 Drive circuitry for a four-electrode platinum electrical conductivity sensor. The EC sensor is driven by a 250 Hz push-pull square-wave via op-amp drivers U1A and U1B whose ground current is approximately equal to the AC current flowing through the conductivity cell. This conductivity current is rectified by the op-amp's output stage and is reflected through a 200:1 current-mirror into the input current side of the 16-bit charge-balance ADC. The LTC6078 micro-power dual op-amp was chosen for its very small quiescent current (an error term in the load current of the conductivity cell). 53
Figure 27 Two wetting-front detectors were installed at Oxford Landing in early 2009, with salinity sensors inserted in early July 2009 in the throats of the WFDs in place of the usual float rods. Continuing drought over the region has meant that insufficient rainfall has fallen to create a wetting front to provide field results in time for thesis publication. The 200-mm depth WFD is installed on the left, and the deeper 400-mm device on the right. Standard vacuum-based soil solute sampling tubes in the bottom left of the photo were installed at these same depths for comparison. The logging system is not shown. 54
Figure 28 Various commercial sap-flow systems (clockwise from top-left): Dynamax 'heat-balance' sap flow sensor, Greenspan 'heat pulse' sap flow sensors, sap flow measurements in large trees present extra challenges! Granier (thermal diffusion) sap flow sensors, physical model of the 'heat-balance' sap flow sensor, sap flow diagram for a tree, Granier sensors (centre). The white band around the tree in the photo on the bottom right-hand side is a 'dendrometer'; an instrument for the continuous monitoring of tree girth, and an indirect method of monitoring plant water status. 60
Figure 29 A thermilinear thermistor, consisting of a high-resistance thermistor thermally and electrically bonded to a low-resistance thermistor. 63
Figure 30 Constant power flow meter using a thermilinear element as a combined sense and heater 65
Figure 31 Block diagram of chopper-based single thermistor constant power heat source (power drive not shown) 67
Figure 32 Dual-current source constant-power thermistor heater. Details of the unity-gain buffer and synchronous demodulator are not shown. 69
Figure 33 Block diagram of the constant power thermistor bridge with inherent temperature measurement. The detail of the inverse square-root circuit is shown in Figure 34 71
Figure 34 Inverse square-root circuit using analog four-quadrant multipliers 77
Figure 35 Two reservoirs open to atmosphere have surface water heights of h_0 and h_3 above a nominal reference plane. The reservoirs are connected between heights h_1 and h_2 (in meters) by a pipe inside of which friction (viscous) forces result in an effective 'head loss' h_L. 84
Figure 36 'Plunging-probe' sensor calibration rig for generating very slow linear velocities for a warm-thermistor probe in an isothermal still water tank. A shaft-encoder [1] having a pulley wheel [2] of 500mm circumference, precision bearings and 1 mm resolution is driven by a DC-Micromotor [3] coupled to a precision all-metal spur gear head [4]. A beaded line [5] is balanced across this pulley wheel by lead counterweight [6] and the lead weight [7] on the stainless-steel shaft [8] carrying the thermistor. The motor raises and lowers the probe through the very still temperature-stable water body in the 20-litre Dewar vessel [9]. The output of the constant-power bridge circuit [10] is recorded by the 6½-digit Keithley K2000 recording multimeter [11]. Power supply and control circuits are not shown. The actual apparatus is shown in Figure 39. 86
Figure 37 Logic-based control circuit for the plunging probe calibration rig 87

Figure 38 The Keithley K2000 6½-digit recording multimeter (top-centre) is programmed from a customized computer program to carry out 1024 measurements at a rate of (typically) every second, measuring the output voltage of the double-bridge constant-power circuit. The close-up of the control and measurement circuit on the right-hand side shows the bread-boarded circuit of the schematic shown in Figure 37. It's not lovely, but it worked. 88
Figure 39 The Unidata shaft-encoder (left-top) monitors the vertical height of the probe balanced across its pulley wheel, which is driven directly by the motor-gearbox unit (right-centre). The Dewer flask sits below the shaft-encoder, and the beaded cable supporting the sensor probe passes through a small hole in the cork lid. 88
Figure 40 A 'single-sweep' seepage meter calibration system. This step-change variable head seepage meter calibrator uses a Hagen-Poiseuille flow controller. A 240-litre container [1] holds a 900-mm depth of well-mixed water at room temperature. The thermistor sensor located at level [4] is submerged by 50 mm when the 1000-mm high x 27.5 mm diameter bore vertical calibration sensor standpipe [2] and electronic control circuit [5] are in the top left-hand position. In this initial position, water in the vertical sensor standpipe is at the same level as the surface of the water in the main tank. When the instrument is plunged to the lower right-hand position, an instantaneous differential head pressure '*H*' is applied to opposite ends of the (coiled) Hagen-Poiseuille flow control pipe [3], which has a 5-mm bore and a length of 33m. *H* is the 'final height' of the step-change in water pressure. The electronics has been incorporated into the standpipe base in order to stabilize its temperature. 89
Figure 41 The seepage meter standpipe can just be seen above the water level in the tank at left. 90
Figure 42 The standpipe is shown in the water column, with the electronics below and the Hagen-Poiseuille flow control pipe to the left (the latter was later replaced by 33 m of wound plastic pipe to lower the Reynolds Number below turbulent flow speeds). Rather than step-change height, the method shown here purged the vertical standpipe using compressed air. Uncapping the top of the standpipe allowed water to flow back in with a first-order time-constant. 90
Figure 43 The seepage meter standpipe is shown with the 'level sensing' thermistors arranged in a logarithmic spacing up though its height. The level sensor spacings were chosen to allow roughly equal time intervals for the arrival of the water-air front at each heated sensor as the water level rose up through the column with decaying velocity, flowing in from the main tank through the flow control pipe on the left. 91
Figure 44 At high flow rates in the 'control pipe' (between 0 and 180 s into the run), flow becomes turbulent (high Reynolds Number) and limits flows in the vertical seepage meter standpipe, as shown by the deviation and oscillations of the flow sensor traces with respect to the expected (red) curve. 93
Figure 45 A bi-directional flow cell and electronics, configured as a differential flow detector, with the upward flow sensor being the master in the control loop, as set by the switch. The voltage across the upward flow sensor would be imposed across the slave thermistor in the downward flow section of the inverted tube. The difference in the thermistor currents – as detected by the instrumentation amplifier – would be the signal. 97
Figure 46 Maximum thermistor temperature occurs at a 1.35 mm/s downward flow that exactly balances the natural convective upward flow for a 40 mW heat output. This leads to a stagnation zone around the thermistor tip that results in maximum heating of the sensor under any flow conditions. The red trace (squares) is the sensor response for upward flows. The blue trace (diamonds) is the sensor response for downward flows. The yellow trace (triangles) is the temperature difference between upward and downward flow values. 98
Figure 47 Calculation of drainage flux from ADC '*counts*' and 'temperature counts' of Figure 50. (Bond and Hutchinson 2006). *A*, *B*, *C* and *D* are calibration-derived coefficients. 100
Figure 48 The 'tube tensiometer' drainage meter is shown on the left of the figure; the electronics of Figure 50 is incorporated into the base of this device. The detail of the sensing tip can be seen on the right, with the single (white) SDI-12 cable for data and command interchange leaving the instrument for the soil surface. The black vent tubes are needed to allow gauge pressure measurements for depth recording and to allow air trapped in internal pore spaces to vent to atmosphere as air enters the drainage meter. (Bond and Hutchinson 2006) 101
Figure 49 The tube tensiometer drainage meter is inserted down an augured hole several meters deep. The two sensor 'tips' of highly conductive diatomaceous earth are formed in-situ to connect the drainage meter to the soil profile. (Bond and Hutchinson 2006) 102
Figure 50 Multi-channel SVFC ADC with temperature correction, used for 15-bit pressure/depth measurements in the CSIRO 'drainage meter', which consists of twin tube tensiometers incorporating electronic gauge-pressure transducers P1 and P2 to monitor a 0-1m water head in each tube. 102
Figure 51 The CSIRO disc permeameter (Perroux and White 1989) for the measurement of tension-infiltration rate into soil. A small negative pressure of a few centimetres of water head is applied to the supply membrane; this prevents water running down wormholes or cracks in the surface (preferential flow), allowing the determination of the soil's unsaturated hydraulic conductivity (matrix flow). 104
Figure 52. An unsaturated flow permeameter for irrigated agricultural soils. Arranging for the device to always overflow creates a constant head pressure ψ_H above the porous plug. The pressure drop across

the porous plug ψ_P (by Darcy's Law) is designed to exceed the positive head pressure ψ_H of free water above the plug. This ensures that water is drawn out of the instrument at a soil moisture tension ψ_S ($=\psi_H - \psi_P$) such that flows only occur in soil micropores rather than in cracks and macropores. 105
Figure 53 Temperature difference signals T_S-T_F versus velocity for four different power levels. Note that data recording actually begins at $t=0$ on the right-hand side of the plot (off-scale) when flow is at a maximum. The null-points are clearly shown for the higher velocities and higher power levels, but become increasingly indistinct at lower flows. The extra peaks at higher velocities around 1.8 mm/s result from initial thermal stratification of the water column above the sensor and correspond to a shift in the background temperature as the thermocline passes over the sensor. Legend colours are: Red: 97 mW, Blue: 77 mW, Yellow: 62 mW and Green: 48 mW 107
Figure 54. Flow response at constant power (97 mW) with normalised T_S; this small offset change is justified as T_S is arbitrarily chosen anyway with this method. If the theory was correct and the calibration rig working as expected all of these 'minima' should occur at the same velocity at this fixed power level. This is clearly not the case here, although many more weeks were to pass before the cause of this flow instability was discovered. 109
Figure 55. Flow response at constant power (97 mW) with 'normalised' TS and velocity. This allows the 'shape' of the response to be seen over 11 consecutive runs. These plots suggest that the inverted thermal plume is less stable when forced below the thermistor tip by overwhelming flows (to the right of the null-point) in comparison to more stable buoyant plume above the sensor tip (to the left of the null-point). The reasons for the double minima in run 11 (brown trace) and blurred minima in run 3 (dark blue trace) are unknown. 109
Figure 56 Future work: In concept, multiple doughnut-shaped salinity and temperature sensors for monitoring density stratification in estuarine river environments slide down the (looped and electrically insulated) mooring cable to the required depth. Such sensors can be pre-calibrated without first having to be assembled into waterproof strings. The mooring cable forms a single winding for the differential phase shift keyed (PSK) magnetic modem that transfers power to multiple sensors and allows bi-directional flow of measurement commands and data. Bio-film build up is ameliorated by exposure of the electrodes to UV LED radiation inside the measurement cell. Water is pumped through the cell using a thermal pump between measurement cycles. 116
Figure 57. Evidence of 'seiching' in the Torrens Lake during a lake-flushing exercise. The inflow hit the dam wall, creating reflections 133
Figure 58. Evidence of 'sensor calibration consistency' in a 16m-water column. Data prior to sunrise on the 28th May 2003 indicated that the top 14m of the water column mixed to within 0.02°C, vindicating the level of matching (±0.01°C) attained during design and calibration. Systems deployed in the Murray River in June 2009 demonstrated matching over similar depths to within ±0.004°C 133
Figure 59. A 'turn-over' event in early autumn at the White Swan Reservoir in Ballarat Victoria. The bottom 2m of the water column is over 1°C cooler than the 14m water column above it. As the surface layers cool, their density increases and the water column becomes unstable, leading to complete mixing around dawn on the 30th May 2003. 134
Figure 60. Evidence of a cold-water in-rush event from the catchment 'short-circuiting' the Happy Valley Reservoir by under-flowing the main water body. The 'curtain effect' of cooler waters at depth can be seen in the data on the sensors between 25m and 32m from midday on the 8th May 2005, reaching a peak around midnight on the 11th May 2005. 134
Figure 61 A radio-linked ship-to-shore buoy supporting a SDI-12 thermistor string. No data logging occurs on the buoy; instead, all data is transmitted immediately after each 15-minute measurement. 135
Figure 62 This Sealite buoy supports a full logging system, an integrated weather station capsule (Vaisala WXT-510) for air temperature, relative humidity, (drum-head) rainfall sensor, barometric pressure, ultrasonic wind speed and direction and separate global solar and net radiation sensors. All of these sensors are SDI-12 compatible, as is the electronic compass (seen through the instrument door) developed to give a local reference direction for the wind direction sensor. The data logger reads only SDI-12 sensors, and includes Next-G cellular-phone telemetry for remote data collection. 135
Figure 63 A spar-buoy supporting three separate thermistor strings having different anchoring arrangements to allow stratification monitoring in the epilimnion (surface layer), metalimnion (thermocline layer) and hypolimnion (bottom layer) of a reservoir, no matter how the water level changes. The perforated plate at the bottom of the buoy acts as a hydraulic damper to prevent the buoy 'bobbing' in rough water. The length of the chain wrapped around this damper plate is adjusted to change the flotation depth of the spar buoy, which sits low in the water (bottom, right) to allow correct operation of the net radiometer. The latter is part of the weather station cluster mounted on the buoy to monitor wind and solar energy. The station uses cellular phone long-haul telemetry and VHF ship-to-shore SCADA radio systems. 136
Figure 64 Comparison of natural (ln), binary (bln) and simple (sln) logarithms 141
Figure 65 Residual errors between real natural logarithms and the 'Simple log' binary approximation 144
Figure 66 Temperature errors resulting from use of the Simple equation in the first order R-T curve 145

Statement

This work contains no material that has been accepted for the award of any other degree or diploma in any university or other tertiary institution. To the best of my knowledge and belief, this thesis contains no materials previously published or written by another person, except where due reference is made in the text.

I give consent to this copy of my thesis, when deposited in the University library, being available for loan and photocopying, subject to the provisions of the Copyright Act 1968.

The author acknowledges that copyright of published works contained within this thesis (as listed on page 9 of this thesis) resides with the copyright holder(s) of those works.

I also give permission for the digital version of my thesis to be made available on the web, via the University's digital research repository, the Library catalogue, the Australasian Digital Theses Program (ADTP) and also through web search engines, unless permission as been granted by the University to restrict access for a period of time.

……..……..

Andrew John Skinner

Dated: -

Acknowledgments

That this thesis was possible at all owes much to my wife, Claudia. She was unfailingly supportive of a husband plodding through life under the combined stresses that a part-time doctorate added to the already volatile mix of running an engineering business full-time, community responsibilities, home renovations, a large vegetable garden, a family, ageing parents and her own studies and small business start-up. She has my special thanks and love.

I owe a particular debt of gratitude to my thesis supervisor, Professor Martin Lambert, as I shall explain.

There are no schools of 'measurement engineering' within modern universities. This is not surprising, as sensors and measurements are common to all the physical sciences, and their design requires input from the disciplines of physics, sensors, electronics, mechanics, software and firmware plus specialist fields such as fluid dynamics, limnology, meteorology and so forth. It made no sense to me to undertake a PhD degree in the electronic and electrical engineering schools where I had received previous Bachelor and Master's degrees, and in a field in which I already had a considerable amount of industrial experience in Australia, Papua-New Guinea and Canada. Rather, it seemed to me to be appropriate to seek a PhD supervisor in the area of water engineering where I could receive specialised supervision in the arcane art of fluid and thermal dynamics – areas in which I had no training or expertise, but which were critical to the perfection of a thermal sensor that would attempt to create a new 'slow flow' measurement record in the field of environmental engineering. I will be forever grateful to Martin for taking on the considerable risk of supervising an unknown student having such a tenuous connection to his own field of water engineering. I have never been disappointed in that decision. That a number of working instruments and original IEEE journal papers have come out of this PhD program owes much to Martin's patience, rigour and consistency and his willingness to accept the slow pace at which I was able to proceed.

My business partner, Joe Hoogland (and Managing Director of our company 'Measurement Engineering Australia'), put up with raids on the company's resources and my sometimes-distracted attention span. He was able to see the (very long) picture of having an Engineering Director who would one day understand the academic system at first hand and be trained in the rigours of research in that parallel universe.

Along the journey I had access to some very fine engineers working in the commercial arena, and some fine scientists who worked for the CSIRO. They let me pick

their brains, and expressed enthusiasm for my sometimes-quaint ideas. In particular, Dr Allan Wallace of Avocet Consulting in Adelaide South Australia provided invaluable CFD modeling in support of the experimental work, help with fluid dynamic concepts such as the Hagen-Poiseuille theory for the seepage meter and co-authorship on the 5th paper (Chapter 7) that supported my (then) vague ideas about a null-buoyancy flow meter principle.

Finally, there is a bunch of folk I don't know - the dozen or so reviewers and editors who read my prototype papers and offered ways to improve them. They contributed immeasurably to the quality of the final papers and hence to this thesis.

Abstract

Measurement of very slow flows in environmental engineering

Many of the flow metering techniques used in industrial applications have finite limits at slow fluid velocities in the order of 10 mm/s. By comparison, many environmental flow rates occur two or more orders of magnitude below this, examples being the rate of sap flow in plants, the percolation rate of rainfall into soil and through the landscape, flows in the benthic boundary layer of lakes, the movement of water through sandy river banks or in the swash zone of beaches, or the seepage rate of groundwater into river beds.

Unlike well-defined industrial flow measurement systems, nature is extravagant with her variability. To counter this, sensor systems in environmental engineering have to be widely flung, inexpensive and highly matched. 'Smart' sensors must therefore be simple designs having calibration techniques that can be highly automated. Additionally, such sensors must be able to compute real data locally, apply temperature corrections, compensate for inherent non-linearity and integrate without fuss into environmental logging systems. This thesis describes the development of sensors and experimental techniques in five very slow flow rate applications in environmental engineering via three published papers and two papers in submission: -

[1]Gravitational flows in a large stratified water body were identified using smart temperature strings; these sensors demonstrated new techniques for low-cost but high-precision thermistor temperature measurements, sensor temperature matching, the generation of complex algorithms within a simple sensor and a method for obtaining two-point calibrations for non-linear sensors. Field work with these sensor strings identified 'short-circuiting' of an urban reservoir during a storm event over the catchment which led to denser cold-water inflows moving along the bottom boundary layer of the lake.

[2]The movement of 'wetting fronts' in the soil below plants mobilizes toxic salts left behind in the soil profile by crop evapotranspiration processes that take up only fresh water. These problems are exacerbated in semi-arid areas under crops irrigated with

[1] Skinner, A.J. and Lambert, M.F. (2006). 'Using smart sensor strings for continuous monitoring of temperature stratification in large water bodies.' IEEE Sensors, Vol. 6, No. 6, December 2006

[2] Skinner, A.J. and Lambert, M.F. (2009). 'An automatic soil salinity sensor based on a wetting front detector.' IEEE Sensors, in submission, July 2009

brackish water. Automatic recording of soil salinity levels is possible using an instrument based on the combination of an EC (electrical conductivity) sensor with a platinum resistance temperature sensor within a funnel-shaped 'wetting front detector' buried in the soil. These two combined sensors extend the usage of the low-cost 16-bit charge-balance analog-to-digital converter developed for use in stratification measurements.

[3]Measurement of sap flow in irrigated agriculture for determining when to irrigate crops was found to be of limited use for determining 'when to water' because the flow signal is masked by the plant's genetically-coded regulatory systems. A new 'double bridge' analog control circuit for a self-heating thermistor was designed and described as a thermal diffusion sensor to study plant water status and the onset of irrigation stress in grapevines once sap flow had ceased. A laboratory experiment on a cut vine cane demonstrated that this thermal diffusion sensor was sensitive enough to track the response of the living cane to external forcing events that changed its plant water status.

[4]The same double-bridge thermistor control circuit was used to investigate the lower limits of very slow ***upward*** flow measurement for use in the funnels of automatic seepage meters designed to monitor groundwater flows into the bottom of rivers and lakes. Theoretical, CFD (computational fluid dynamics) and two different experimental studies showed that flows between 0.03 mm/s and 3 mm/s could be measured in the presence of buoyant thermal plumes from the self-heated spherical sensor in free water.

[5]A new type of null-buoyancy thermal flow sensor is described; it is designed specifically for the measurement of ***downward*** flows below 3 mm/s using a single thermistor. A typical application of such flow meter technology would be in the measurement of the hydraulic conductivity of soil to determine the rate at which rainfall can enter the landscape without run-off and erosion. The thermistor power dissipation is adjusted so that the upward thrust of the buoyant thermal plume from the warm thermistor sensor exactly counter-balances the downward bulk fluid velocity, resulting in flow stagnation at the sensor tip characterized by a corresponding local peak in the sensor's

[3] Skinner, A.J. and Lambert, M.F. (2009). 'A log-antilog analog control circuit for constant-power warm-thermistor sensors – Application to plant water status measurement.' IEEE Sensors, Vol. 9, Issue 9, September 2009

[4] Skinner, A.J. and Lambert, M.F. (2009). 'Evaluation of a warm-thermistor flow sensor for use in automatic seepage meters.' IEEE Sensors, Vol. 9, Issue 9, September 2009

[5] Skinner, A.J. and Lambert, M.F. (2009). 'A null-buoyancy thermal flow meter: Application to the measurement of the hydraulic conductivity of soils.' IEEE Sensors, in submission, August 2009.

temperature response. Power dissipation must increase with the square of an increasing flow velocity to maintain this null-point.

Chapter 1. Introduction

There exists a plethora of sensors for measuring flows in industrial situations, a much smaller number for measuring flows in hydrological applications, and a tiny number that are able to measure the very slow flows occurring in environmental applications. Yet these real and increasingly important environmental flows transport water, salts, leachates and nutrients in ecological systems such as soils, plants and water bodies. Typical of such very slow rates in nature are the rate of sap flow in plants, the percolation rate of rainfall into and through the landscape, flows in the benthic boundary layer of lakes, the movement of water through sandy river banks or in the swash zone of beaches, and the seepage rate of ground water into river beds.

Unlike well-defined industrial flow measurement systems, nature is extravagant with her variability. To counter this, sensor systems in environmental engineering have to be widely flung, inexpensive and highly matched. This demands special effort on the part of the sensor designer; designs must be honed-to-the-bone to cut component costs before commercial release, and calibration techniques need to be highly automated to reduce labour costs during manufacture. 'Smart' sensors are needed to compute real data right down at sensor level, rather than rely upon post-processing of data higher up the data collection chain to convert 'dumb' sensor outputs from voltages or counts into kPa, mm/s or °C. This requires sensors to 'own' their own specific calibration coefficients, and to be able to apply them locally through complex calculations that often include temperature correction and compensation for inherent non-linearity. Such calculations provide a particular challenge to sensor designers working without benefit of either computing power or program space for look-up tables or floating-point maths routines. Finally, environmental sensors have to be able to be hooked together in a simple fashion by field scientists unfamiliar with the complexities of electrical wiring and communication protocols. These 'smart' sensors need to be networked and logged and telemetered to software that can land data on the desktops of a plethora of users spread across all the physical sciences. Mother Nature herself seems to conspire against successful long-term measurement of her machinations; environmental measurement systems must operate through uncontrollable climatic extremes and attacks by a host of creatures from ants, foxes and cows to moulds and bacteria.

This thesis describes the development of sensor technology to measure very slow environmental flows and the saline fluxes that they transport. A variety of sensor technologies were developed to demonstrate that even simple sensors can be effective

measurement tools at these very slow flow rates. This 'thesis-by-publication' describes this body of work in three published and two submitted papers, leading up to the discovery of a new null-buoyancy method of slow flow measurement. Each chapter gave rise to a specific paper, and includes background material to round out the motivation and evolutionary steps behind a particular sensor's development.

Chapter 3 describes the development of a string of highly matched smart thermistor temperature sensors for measuring the vertical temperature profile – the thermal stratification – of a large water body. Thermal stratification coupled with high wind stresses on a lake surface may give rise to internal waves along the thermocline - the sharp temperature/density boundary between the warm surface and cool bottom layers in the water column. These internal waves can break along the sloping boundaries at the bottom layer of a lake, driving mixing events. Such internal waves have periods of about a day and can be seen by a thermistor string located within the main water column. Another type of very slow flow in lakes – a gravity current caused by plunging cold water inflows - gave rise to a benthic layer flow underneath a suburban reservoir that was detected during field deployment of one such smart sensor string (Appendix A).

This paper lays the groundwork for new high-precision low-cost measurement circuitry with the design of an analog-to-digital converter (ADC) based upon a modified form of a synchronous voltage-to-frequency converter (SVFC) coupled to a microcontroller. The paper develops the concept of 'bulk temperature coefficients' for reducing measurement uncertainty.

The Steinhart-Hart Equation is an inverse third-order logarithmic polynomial used to convert thermistor resistance to temperature. Appendix C provides Microsoft Excel formulae for solving this equation in spreadsheets. Appendix B describes attempts to use a variation of binary logarithms to solve this equation in a simpler fashion suitable for use in low-cost thermistor strings. These numerical methods were not ultimately used in a working sensor, but led instead to a slower but simpler 'method of differences' – a new and more general method of handling complex algorithms in dumb sensor microcontrollers. Generation of complex internal 'standard' calibration curves allowed linearization of non-linear sensors, opening up the possibility for a far simpler two-point calibration of these sensors in the field as well as the laboratory. A computer-controlled calibration process was able to match hundreds of these sensors to within ±0.006°C of each other without manual intervention. This is an important aspect of manufacturing low cost 'smart' sensors.

Failure of monotonicity in this ADC, described in Appendix D, resulted in a redesigned sensor having an increased sensitivity of 0.001°C, monotonic output and greater simplicity.

Development of a multi-channel ADC based on this original design was necessary during the development of a 'drainage meter' for monitoring the very slow flows (millimeters per day) that occur as moisture moves through the landscape. This instrument, developed by Dr Paul Hutchinson of CSIRO Land and Water, used twin tube tensiometers to measure the vertical hydraulic potential gradient in soils under crop root zones in a direct rendition of Darcy's Law for flows in porous materials. The resultant instrument was capable of indicating very slow drainage flows downward and evaporative fluxes upwards. However, without some knowledge of the local hydraulic conductivity of the soil – a subject tackled under a different guise in Chapter 7 - this instrument could only deliver qualitative rather than quantitative data. The instrument developed by CSIRO required highly matched pressure transducers to measure water level in each of two tube tensiometers. That the success of the new ADC and temperature matching described in Chapter 3 could not be reproduced in the drainage meter of Chapter 7 was a direct failure of the silicon pressure transducers selected. These exhibited a gross non-linearity in their temperature coefficients, which prevented adequate inter-sensor matching to the desired ±5 mm.

A far simpler method of measuring water level in the 0-1m range is developed in Chapter 6, where parallel self-heated thermistors were used to determine the time-constant of a falling-head flow calibrator.

Chapter 4 describes how this ADC was simplified and improved for thermistor temperature measurement and then extended to monitor four-electrode electrical conductivity (EC) using AC excitation and water temperature sensors based on platinum resistance sensors without recourse to the usual expensive instrumentation amplifiers. This sensor has been designed to be placed within a funnel-shaped 'wetting front detector' buried in the soil to automatically record the level of toxic salts accumulating then mobilized in soils under the slow flow conditions below plants in the landscape following rainfall or irrigation events.

These same salinity sensors are capable of monitoring other slow flows in nature, although applications are not described in detail in this thesis. Salinity strings, outlined under 'Future Work' in Chapter 8, are an extension of the temperature strings of Chapter 3 and would be useful for measuring the density stratification caused by both temperature and salt in the water column of estuarine and river systems where fresh water outflows

move over denser salt water inflows. Salinity measurements are also a natural adjunct to the very slow flows described in Chapter 6 on the development of seepage meters – instruments that monitor the interaction of fluid and salt fluxes between groundwater and surface water systems.

Chapter 5 introduces new warm thermistor analog control circuitry capable of operating over a wide dynamic range while holding thermistor power output constant and monitoring the internal temperature of the thermistor in either ambient temperature or self-heating modes. This sensor was used to demonstrate the value of thermal diffusion measurements when sap flow in irrigated vines had ceased – the basis of a new method of scheduling 'when to water'.

Chapter 6 makes use of this same circuitry to tackle flow measurements in the sub-3 mm/s flow range where buoyancy effects have traditionally limited thermal flow metering. Overcoming this 'slow-flow barrier' allowed the development of a seepage meter for measuring uni-directional groundwater inflows into a riverbed. This chapter uses a combination of physical, numerical and experimental techniques to show that a linear relationship exists between flow and specific temperature differences under flow and no-flow conditions. The novel calibration techniques that were developed were applicable to the new null-buoyancy thermal flow meter that is the outcome of this thesis.

Chapter 7 introduces a single thermistor sensor technology capable of monitoring the very slow downward vertical flows occurring in permeameters; instruments for the measurement of the hydraulic conductivity of soil. Permeameters are used to provide information on whether rainfall or irrigation would permeate the landscape or result in surface run-off. The thermistor drive circuitry of Chapter 4 and the variant of the calibration techniques from Chapter 5 are utilized in the control and calibration of the warm thermistor sensor. The power output from the warm thermistor in this new sensor technology is adjusted such that the up-thrust of the buoyant thermal plume exactly balances the bulk downward fluid velocity to create a stagnation point at the sensor tip. This results in a higher-temperature singularity at the null-point that corresponds to a unique flow velocity. Sensor power dissipation must increase according to the square of the fluid velocity. Experimental laboratory work was aimed at verifying the output of a CFD model extended from the earlier work described in Chapter 6 on seepage meters. An engineering analogy was developed by a co-author of the resulting paper to explain this phenomenon in terms of a heated sphere rising through a static fluid at its terminal velocity.

In all, a number of potential sensors are described in this thesis, each of which addresses a different aspect of the measurement of very slow flows in environmental engineering: -

1. temperature and salinity strings for indirectly monitoring slow flows in open water bodies,
2. a plant water-status sensor for monitoring tissue water potential once sap flow has stopped,
3. a seepage meter for monitoring flows between ground and surface water,
4. an array of simple water level sensors using self-heated thermistors to monitor vertical flows where a free-water surface occurs,
5. an automated soil salinity sensor for monitoring salt movement in the root zone of crops,
6. a drainage meter for monitoring very slow vertical flows in the soil profile, and
7. an automated permeameter for monitoring the rate at which rainfall can flow into the landscape.

List of papers

Skinner, A.J. and Lambert, M.F. (2006). 'Using smart sensor strings for continuous monitoring of temperature stratification in large water bodies.' IEEE Sensors, Vol. 6, No. 6, December 2006

Skinner, A.J. and Lambert, M.F. (2009). 'An automatic soil salinity sensor based on a wetting front detector.' IEEE Sensors, in submission, July 2009

Skinner, A.J. and Lambert, M.F. (2009). 'A log-antilog analog control circuit for constant-power warm-thermistor sensors – Application to plant water status measurement.' IEEE Sensors, Vol. 9, Issue 9, September 2009

Skinner, A.J. and Lambert, M.F. (2009). 'Evaluation of a warm-thermistor flow sensor for use in automatic seepage meters.' IEEE Sensors, Vol. 9, Issue 9, September 2009

Skinner, A.J. and Lambert, M.F. (2009). 'A null-buoyancy thermal flow meter: Application to the measurement of the hydraulic conductivity of soils.' IEEE Sensors, in submission, August 2009.

Skinner, A.J. and Lambert, M.F. (2009). 'An arithmetic solution to the Steinhart-Hart Equation for thermistors.' IEEE Sensors, in submission, December 2009. (Based on Appendix B)

Chapter 2. Literature Review

Measurement engineers get to poke about in everyone else's branch of science, and so wind up knowing a little about a lot. Their literature reviews should reflect this diversity.

Section 2.1 looks at the various flow regimes that occur in stratified lakes as background material for the development of thermistor strings described in Chapter 3 for the indirect monitoring of such very slow flows along the benthic boundary layer.

Section 2.2 reviews the development of 'rate-of-heat loss' thermal and warm thermistor flow sensors by previous researchers, where heat loss from a device held at some temperature above ambient is measured as an indicator of flow speed.

Section 2.3 reviews a different type of thermal flow sensor called a 'temperature rise' or 'thermal-field distortion' flow meter. Most often used in pipe-based flows, this technique has also been applied to sap flow measurement in trees. This principle measures flow velocity via the temperature difference between upstream and downstream thermometers equally spaced on either side of a constant power heat source in the flow stream.

Section 2.4 describes a third type of thermal flow meter – the 'heat pulse' flow meter – used to measure very slow flow rates of sap in trees and groundwater in seepage meter funnels. Here, the flow velocity is measured as the time taken for a sharp heat pulse injected into the flow stream to flow over a fixed distance between two asymmetrically placed temperature sensors upstream and downstream of the heat source.

This thesis presents a fourth type of thermal flow meter – a 'null-buoyancy' flow meter – particularly suited to very slow downward flows.

Other literature reviews have been included at the beginning of each chapter and in the introduction to each papers as they make much more sense when read in the context of the sensor development and evaluation work that follows: -

1) In Chapter 3, the basic operating principles of a particular commercial charge-balance analog-to-digital converter are reviewed. This device inspired the development of a new type of ADC suitable for lower-cost sensing technology and which evolved into the measurement core within the highly matched thermistor strings, drainage meter pressure sensors and salinity sensors described elsewhere in the thesis.
2) In Chapter 4, salinity measurements and soil salinity sampling methods are reviewed in the paper on a new soil pore-water salinity sensor

3) In Chapter 5, sap flow and plant water status measurement techniques are reviewed in the paper on the measurement of plant water status
4) In Chapter 6, various seepage meters in the literature are reviewed in the paper describing the evaluation of warm-thermistor technology for use in automatic seepage meters
5) In Chapter 7, the literature on permeameters and infiltrometers for the measurement of the hydraulic conductivity of soil is reviewed in the paper describing a possible sensor for use in the very slow downward flow measurements that would be needed in an automated permeameter

The literature fell into the background as new ideas (often triggered by the earlier work of various authors) were developed, but continued to serve as an early catalyst in choosing directions. The literature later provided guidance into the history of various instruments - sap flow sensors, seepage meters and permeameters - that generated specific applications upon which to trial very slow flow sensor technologies. That such applications are the focus of each paper arises from a very real need in the community to improve environmental measurement tools at a time when the planet's support systems are under increasing stress. To measure is to know.

2.1 Very slow flows in stratified lakes

Various authors (eg Rutherford *et al.*, 1993) have shown that thermal stratification of large water bodies can be measured continuously using multiple thermistors hanging vertically through the water column and attached to a data logger at the surface. Such sensor 'strings' present a useful but indirect picture of the internal wave-field in the off-shore regions of a temperature stratified lake, and can highlight the potential for basin-scale currents arising from various modes of seiching, Kelvin and Poincaré waves and forced gravity currents. Such sensor strings can also capture 'lake turn-over' events in polymictic and the more widely distributed warm monomictic lakes as winter approaches. Surface waters cool to a temperature below that of the bottom waters, creating a density instability that results in denser surface waters falling through less dense deeper waters, causing these lakes to mix thoroughly from top to bottom. In urban water storage reservoirs, this creates sharp changes in water quality that impact directly on down-stream water treatment plants.

Toxic blue-green algae blooms in the warm sunny surface layers of stratified lakes have traditionally been treated by copper-sulphate dosing, but more recently by bubble

plumes (Lemckert and Imberger 1993) or surface mixers (Lewis et al 2003). More intelligent and cost-effective thermal stratification sensor strings could improve our understanding of the three-dimensional internal processes within lakes by deployment of multiple strings across a wider area or where specific problems occur. Chapter 3 describes the development of such technology. Appendix A presents both sample data and instrument systems.

Thorpe (1999) reviewed the processes that result in internal wave generation, mixing and intrusions on the sloping sides of stratified lakes. Imberger (1998) reviewed the flux paths in stratified lakes, while focusing on the energy transfer mechanisms in the aftermath of wind-forcing events that created basin scale internal waves or simple gravitational seiching. Wüest and Lorke (2003) reviewed the turbulent mixing zones at the lake surface and above the bottom boundary layer, while noting that turbulence in the interior of lakes is extremely weak. Various researchers (Imberger and Ivey 1991, Lemckert and Imberger 1998 and Saggio and Imberger 2001), using portable flux profilers, had shown that turbulent patches do occur around the thermocline in off-shore areas of lakes as a result of breaking waves in the internal wave field. Lorke et al (2002), using high-resolution current profiler and temperature microstructure measurements, pointed out that even simple seiching motions in a lake created changes in turbulent fluxes of momentum and dissolved solids in the bottom boundary layer. Wüest and Lorke (2009) summarized the various flow regimes and exchange mechanisms in the bottom boundary layer of natural inland water bodies due to the action of seiches and shear-induced convection on sloping boundary layers. The authors saw insights into bottom-boundary layer processes as important prerequisites for understanding turbulent basin-scale diapycnal diffusivity in lakes and for quantifying biogeochemical fluxes and transformations (such as methane) in aquatic systems. Brand et al (2007), using a novel gas tracer method, presented high-resolution in-situ measurements at the bottom of a pre-alpine lake with shear velocities as low as 1.3 mm/s. It is clear from the literature that the hydrodynamics of the bottom boundary layer are of increasing interest to limnologists.

It is equally clear that there is a paucity of measurement tools capable of economically returning continuous long-term data records from the bottom boundary layer. While portable flux profilers have provided rich spatial data in the water column above a single point, the number of manual casts that can be made limits their temporal resolution. Acoustic Doppler Current Profilers (ADCPs) can gather longer-term records of flow and turbulence in the bottom metre or so of the water column, but the expense of such measurement stations limits their spatial replication throughout a large water body.

In the early stages of this thesis, the intention was to find a better way to use warm thermistor flow meters to make flow measurements on the bottom boundary layer of lakes and rivers. The limited operating temperature range of these analog bridge designs proposed by early authors in this field (eg Riedl and Machan, 1972) are described in Section 2.2. The intent was to create 'flow sensor strings' consisting of flow speed and direction sensors arrayed along a submerged hanging cable tailored especially for the very slow flows occurring in the bottom boundary layer of lakes, similar to the temperature strings developed in Chapter 3 of this thesis. This was not to be; once the first CFD models showed the warm plume above a self-heated thermistor it became apparent that the first order of sensor design needed to focus on vertical flows along the same axis as the buoyancy forces. The exclusively horizontal flows in lakes would need to wait while other vertical flow applications mapped out the scope of the buoyancy effects below 3 mm/s where earlier authors (e.g. MacIntyre 1986) had faltered in the measurement of very slow flows. Accordingly, chapters 6 and 7 explore both upward and downward flows.

2.2 'Rate-of-heat loss' flow meters in the literature

'Rate of heat loss' flow meters have traditionally measured the power dissipated into the flow stream from an electrically heated resistance element held at a high fixed temperature, or at a fixed over-temperature value with respect to ambient temperature. The classic thermoanemometer of this type is the hot-wire anemometer of Figure 1 used for measurement of instantaneous gas flow velocities and turbulence, and comprehensively described by Lomas (1986).

The tungsten wire used in hot-wire anemometry may have a diameter of only 4μm, a length of 1.25mm and an over-temperature operating set-point of 250°C. These very fine diameters give the hot-wire anemometer its excellent frequency response, and make it ideal for turbulence studies in clean gas streams ('dirty' gas streams can contaminate the wire). The small probes also offer very high spatial resolution. The hot-wire anemometer is, however, too fragile and unstable for long-term field measurements in open water bodies, and is unsuitable for flow measurements in electrically conductive fluids such as water.

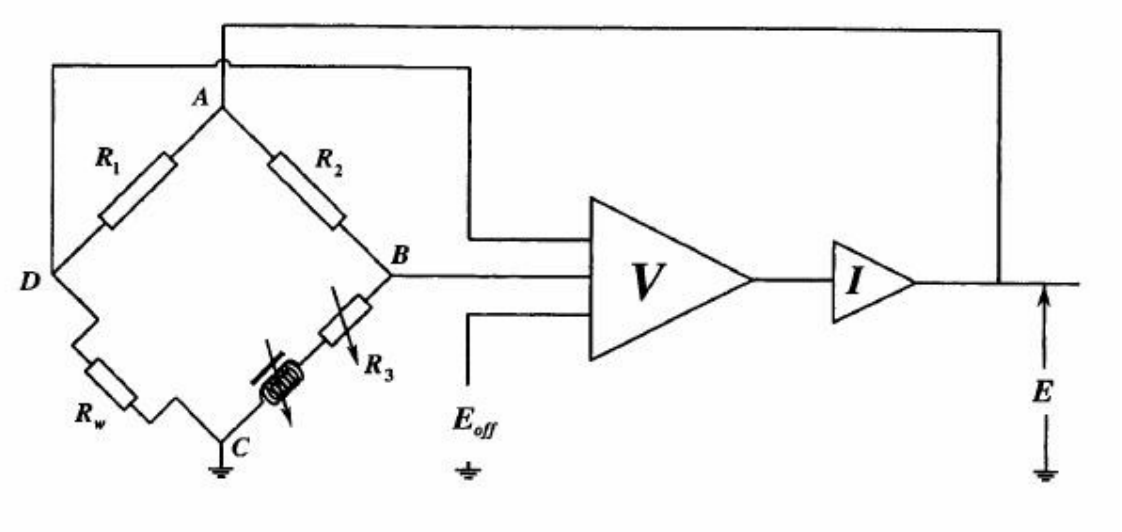

Figure 1 A simple constant-temperature hot wire/hot film anemometer, using an adjustable resistance to force a constant temperature onto the hot wire as described by Lomas (1986) and reproduced from Sheldrake (1995). Setting the variable resistance R_3 to a particular value forces the control loop to adjust the bridge voltage to impress a voltage across the hot-wire R_W, thus raising it to a constant temperature as it dissipates power. The bridge voltage E is the output signal, and varies as the fluid flow rate changes the rate-of-heat loss from the sensor element.

Such hot wire anemometers are characterized by the classic King equation (King 1914)

$$q_t = \Delta T\left(k + 2\left(kC_v \rho \pi d v\right)^{\frac{1}{2}} \right) \tag{2.1}$$

where the rate of heat loss per unit time q_t is proportional to the diameter d of the hot-wire in a fluid having velocity v, density ρ, specific heat at constant volume Cv and thermal conductivity k. It is also dependent upon the mean temperature elevation ΔT of the wire, which the sensor control circuit seeks to maintain above the ambient fluid temperature; it is known as a 'constant temperature' flow meter. The electrical power q_t needed to maintain this over-temperature ΔT is measured and converted to an output signal dependent upon flow velocity v.

2.2.1 Thermistor flow meters in the literature

Various authors have tackled the problem of continuous measurement of flow rates in open water bodies or closed pipe systems using warm thermistor rather than hot-wire flow meters. Thermistors have the advantage of rugged construction, inherently high resistance (simplifying measurement) and a resistance sensitivity to temperature an order of magnitude higher than metal sensors. The hermetic glass encapsulation found in glass rod thermistors provides excellent sealing against water ingress. The thermistor is more

difficult to use than a linear resistance element in a standard bridge circuit, because of the thermistor's high degree of non-linearity (Section 2.5.1). While the thermistor is the logical choice when building a flow meter for water rather than gas, most of the historical circuit designs continued to employ a form of the 'constant temperature' technique derived for hot-wire anemometers.

Catellani *et al.* (1982a, 1982b) produced a number of papers on the performance and temperature stability of an air mass flow meter based on the self-heated thermistor, providing some theoretical background to the response and accuracy of these devices. It is possible to make a crude flow meter circuit (Molina *et al.* 1994) by self-heating a thermistor with an applied voltage and measuring the resultant current flow. This technique relies upon fluid temperature being perfectly stable, which is rarely the case in natural water bodies. Riedl and Machan (1972), LaBarbera and Vogel (1976), Briggs-Smith *et al.* (1981), MacIntyre (1986), Kung *et al.* (1987), and Yang *et al.* (1988) attempted to monitor and correct for ambient fluid temperature by inserting a second ambient thermistor into a bridge circuit in a similar manner to that used for hot-wire anemometry. These flow sensor designs are described in more detail in the following sections. In general, a low-resistance thermistor was self-heated in one half of the bridge while higher resistance (non self-heating) thermistors were used in the other half of the bridge to compensate for changes in ambient temperature and to force a constant over-temperature condition ΔT upon the warm thermistor. Some measure of the bridge's power dissipation P was used to determine flow velocity v. These analog bridges all suffered from a limited operating temperature range, imposed by the necessity of matching two unmatched thermistors, having different material curves (thermistor beta values) and essentially operating at different temperatures and placed at different locations in the flow stream. Yang *et al.* (1988) provided possibly the best description of this body of work, and created an active two-thermistor analog bridge which they attempted to balance in such a way as to extend the operating temperature range while providing an output directly proportional to flow rate. These authors — measuring volumetric fluid flow Q in a pipe — used a simplified empirical form of the King Equation to describe the relationship between flow rate Q and rate of heat loss P at an over-temperature condition of $(T\text{-}T_A)$

$$P = \left(K_1 + K_2 \cdot \sqrt{Q}\right) \cdot (T - T_A) \tag{2.2}$$

where K_1 and K_2 are constants depending upon geometric factors, the structure of the surface of the measurement probe and the thermal properties of the liquid. T and T_A are

the temperature of the measurement probe and the fluid respectively.

The range of warm thermistor thermal anemometers described above typically operated over a flow velocity range between 3 mm/s and 50 mm/s. Their maximum frequency response was limited by the mass of the thermistor. Typical thermistors used had a diameter of 0.9 mm in a glass-encapsulated bead with a typical frequency response of less than 6 Hz.

2.2.2 The most basic thermistor flow meter

Molina et al (1994) - Figure 2 - built a crude thermo-anemometer based on an adjustable voltage regulator driving a warm thermistor probe through an ammeter to ground. Prior to each measurement they carefully adjusted the voltage across the thermistor according to the current ambient temperature of fluid in a static bath. The NTC thermistor was driven into an over-temperature (self-heating) mode. Measurements of flow were based on the variation in regulator output current once flow was imposed. The authors make no mention of the fact that output current is highly dependent on the ambient temperature of the fluid.

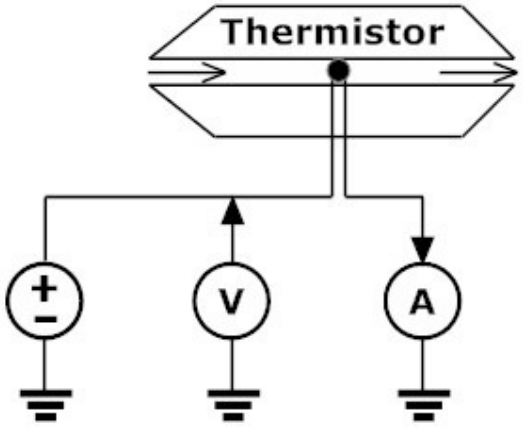

Figure 2 The simplest possible method of creating a warm thermistor flow meter, adapted from Molina, Victoria and Ibanez (1994). The voltage regulator impresses a DC voltage across the thermistor and the ammeter measures the current flow to ground as a flow-dependent signal. This method is dependent upon isothermal fluid temperature.

2.2.3 A simple temperature-compensated thermistor flow meter

A more logical development then is to use a second thermistor in the right hand reference half of a bridge circuit in constant temperature anemometry. A device with a similar transfer characteristic then compensates for the non-linear characteristics of the thermistor. The difficulty with this technique is that a thermistor's rate of change of resistance is much more sensitive to changes at colder temperatures than warmer temperatures; between 3...4% per °C at 25°C compared to a mere 2% per °C at 50°C.

Therefore two similar thermistors, one heated, and one a reference thermistor will invariably have different rates of resistance/temperature change even at small temperature separations of a few degrees.

Nevertheless, an anemometer of this type was built by Vogel (1969) for the measurement of airflow behind insects. This flow meter (Figure 3) used two same-value thermistors in a bridge circuit on each side of the top half of the bridge.

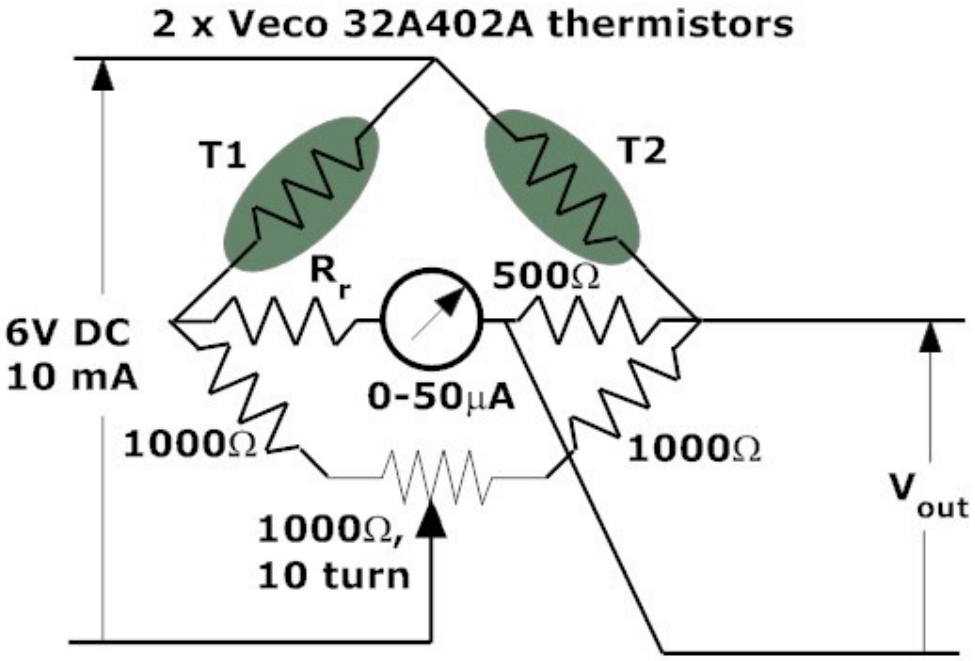

Figure 3 The Vogel (1969) warm thermistor flow meter

In this equal arm bridge both thermistors were heated equally by the current flowing through them. To get a flow signal from bridge imbalance, it was necessary to shield one of the thermistors from small airflows. The author did this by placing the reference-heated thermistor on the right hand side of the bridge inside a small piece of tubing so that no air flowed over it. Airflow over the exposed heated thermistor caused temperature depression, an increased resistance and a bridge imbalance that could be detected and calibrated as airflow.

2.2.4 An effective temperature-compensated thermistor flow meter

The first serious attempt to build a temperature-compensated warm thermistor bridge was made by Riedl and Machan (1972) and is shown in Figure 4. The authors used a 100 ohm low resistance thermistor in the left hand heated side of the bridge and used much higher resistance thermistors in the right hand side of the bridge to track ambient

temperature. Under zero-flow conditions the imbalance voltage from the bridge would always be zero if the thermistors were correctly matched.

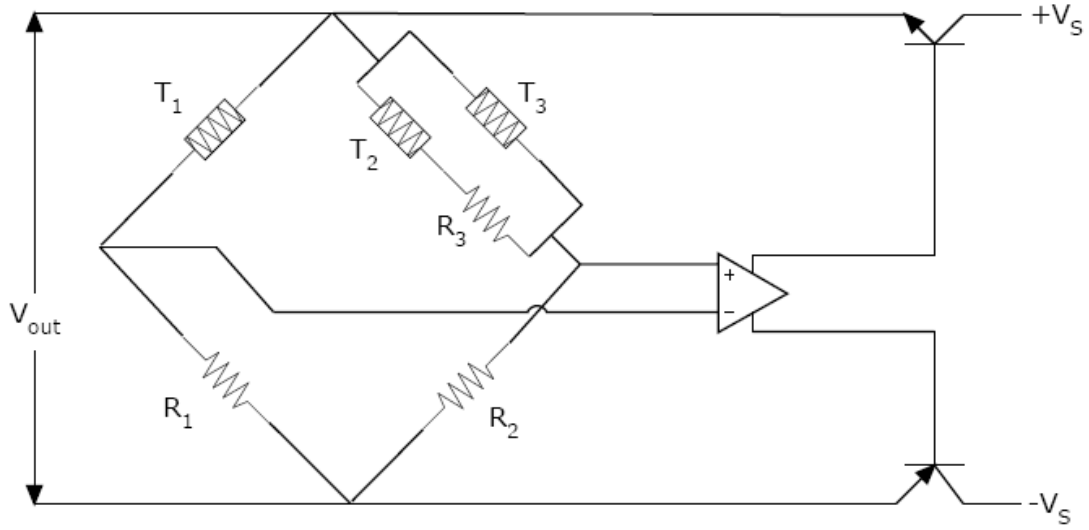

Figure 4 The Riedl and Machan (1972) Bridge Flowmeter. These early flow-monitoring bridge circuits were always in self-heating mode, and were unable to report on the temperature of either the water or the heated thermistor. Instead, their output was proportional to power dissipated by the self-heated thermistor. R_1=100Ω (adjustable), *R2*=1500Ω, *R3*=1200Ω, *T1*=100Ω thermistor, *T2*=1000Ω thermistor, *T1*=3000Ω thermistor at 25°C

This bridge uses active temperature compensation and operates in constant over-temperature mode. Flow rate is a function of bridge voltage V_{out} provided R_1 is adjusted to a value in the middle of the range of possible resistance values of the flow meter thermistor. The authors claim that the flow meter is "reasonably independent" of water temperature over the range 5°C to 35°C. The difficulty with this technique is that it works only over a limited range of ambient temperatures before thermistor mismatch errors become excessive. Riedl and Machan, to some extent, extended the operating temperature range by using two reference thermistors, along with parallel and series combination resistors, in their temperature compensation network on the right hand side of the bridge to better track the warm thermistor's response curve.

2.2.5 The LaBarbera and Vogel bridge

The Riedl and Machan bridge (1972) had multiple temperature-compensation thermistors to extend the operating temperature range, although these improvements to do not seem to have been taken up by later authors who referred to their original work. The uncommon differential input and output bridge drive circuitry of the Riedl and Machan bridge was improved by LaBarbera and Vogel (1976) by incorporating a bridge drive circuit proportional to the bridge imbalance. This is shown in Figure 5.

NOTE:
This figure is included on page 20 of the print copy of the thesis held in the University of Adelaide Library.

Figure 5 The LaBarbera and Vogel (1976) bridge. A and B are the flow meter with voltage-to-frequency converter C and frequency-to-voltage converter D

A forced null-balance is imposed upon the bridge by the single op-amp and PNP transistor ***Q1*** configured as an emitter-follower to change the bridge voltage as the heated thermistor responds to its external environment. Figure 5 from the original paper shows the various bridge components, plus the ancillary voltage-to-frequency converter circuitry designed to record flow rates to a tape recorder in the era before electronic data loggers were readily available.

This simplified circuit makes use of the bridge voltage as a measure of the power dissipated into the flow stream by the heated thermistor. The authors claim a velocity measurement range between 2 mm/s and 500 mm/s. However, LaBarbera and Vogel (1976) regressed to a single reference thermistor in the right hand reference half of the bridge rather than the combination thermistor method used by Riedl and Machan (1972). In this way they limited the temperature range over which the bridge could accurately operate. There is no reason that they could not have used the combination thermistors, unless it was a question of expense or complexity. Another source of error is the temperature-sensitive base-emitter drop in the transistor at the bottom of the bridge, and which controls the bridge current. This error term in the signal is added to the flow signal. Nevertheless, this same circuitry was used by McIntyre (1986) for the study of flow in a small lake.

2.2.6 The Yang et al bridge

The first real improvement in thermistor bridge circuitry came later with work by Yang, Kummel and Soeberg (1988) using a constant temperature bridge, but in this case using the more sophisticated circuitry shown in Figure 6.

These authors linearized the thermistor characteristic somewhat by including parallel resistors R_2 and R_6 across the warm and reference thermistors R_m and R_r respectively on both sides of the bridge. This technique desensitizes the thermistor characteristic somewhat, but it does improve the operating temperature range to between 10°C and 35°C.

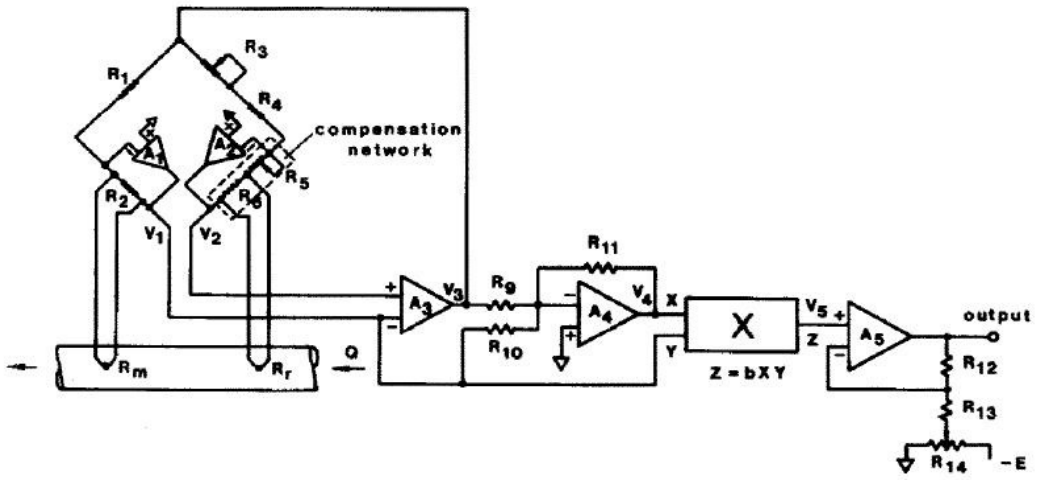

Figure 6 The active-bridge flowmeter of Yang, Kummel and Soeberg (1988). R_m is the measurement thermistor and R_r is the reference thermistor

The active drive across the thermistors clamps the left and right bridge junctions to ground potential, and force V_1 and V_2 to be equal by changing bridge voltage V_3 such that

$$V_{out} = V_o + (\frac{R_{12} + R_{13})}{R_{13}} \times C \times T_h \times K_2 \times Q^{0.5} \qquad (2.3)$$

where

Vo is the offset adjustment on the only adjustment, R_{14}

$$C = b \times R_1 \times \frac{R_{11}}{R_9}$$

b is a multiplier factor, such that $Z = b \times Y$

T_h is the temperature difference between the measurement (heated) thermistor T_H and the fluid temperature T_S, and remains constant

K_2 is a constant/coefficient

Q is the flow rate in m^3/s

This was an active bridge circuit and did away with some of the problems in the LaBarbera and Vogel (1976) circuitry by using a multiplier in the output circuitry to correct the flow characteristics of the bridge to convert the bridge voltage into a signal proportional directly to mass flow. Yang *et al* used this warm thermistor flow meter technique in a 2mm-bore pipe. Nevertheless, the technique is applicable to flow measurement in open bodies of water, and while somewhat more complex was an improvement in the quality of the constant temperature warm thermistor bridge.

2.2.7 Digital thermistor bridge circuits

Warm thermistor flow meter bridges up until 1981 were all analog bridges with a constant output proportional in some manner to flow.

One of the first attempts published to use a digital bridge - Figure 7 - was produced by Briggs-Smith, Piscitelli and Livrea (1981), using the pulsed thermistor technique for measuring very low liquid flow rates in a pipe. This device was used to measure a flow in a small 4-mm diameter pipe in a medical application. It used a temperature compensation thermistor located 6-mm upstream of the heated thermistor in the pipe and was able to make measurements in a volumetric flow range of 2 to 20 millilitres per minute. This volumetric flow rate equates to a minimum linear flow rate of 2.6 mm/s.

Curiously, the temperature compensation thermistor $\boldsymbol{T_C}$ has been placed downstream of the heated thermistor in the wake of the heat stream; this would likely create undesirable thermal feedback while failing to correct the probe for changes in upstream ambient fluid temperature.

This device is a primitive thermal-to-frequency converter, and is reliant upon a precision capacitor to maintain a stable pulse width over time. The properties of the reset transistor are also temperature-dependent. A more suitable circuit would be the synchronous voltage-to-frequency converter described in Chapter 3 of this thesis, as these use ratiometric voltage, clock and time references to cancel long-term drift. Rather than an integrator capacitor in the ADC, the thermistor might well be a ‘thermal capacitor’ oscillating between heated and cool states at a rate dependent upon thermal diffusivity into the flow stream.

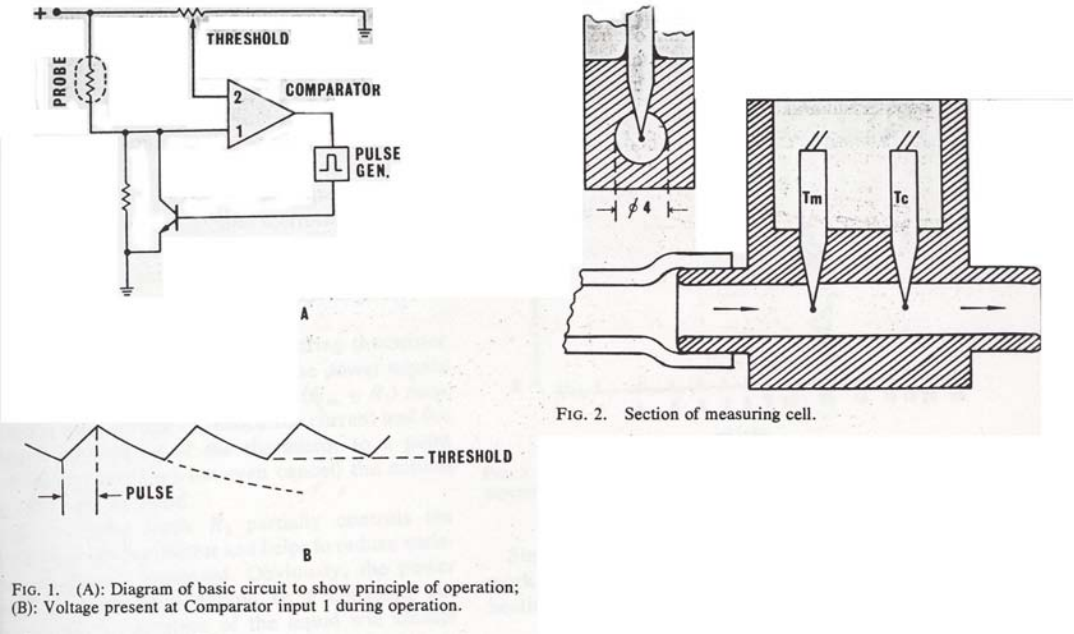

FIG. 1. (A): Diagram of basic circuit to show principle of operation; (B): Voltage present at Comparator input 1 during operation.

FIG. 2. Section of measuring cell.

Figure 7 Pulsed thermistor bridge of Briggs-Smith and Piscitelli (1981)

2.2.8 A transient response thermal flow sensor using intertwined PRTDs

Taking a completely different approach to the problem, Sonnenschmidt and Vanselow (1996) showed that it was possible to make very slow flow measurements using the transient response of a thermal flow meter rather than the steady state responses typified in all the previous bridge circuits discussed. Two platinum resistance temperature devices (PRTDs) were inter-wound within the sensor as shown in Figure 8; one acted as a switched heater driven by a high heating current, while the second monitored the temperature rise via a low excitation current below the self-heating threshold.

One of the PRTDs acted as the heater while the other sensor measured the temperature rise. The heater was pulsed on under constant power for a fixed period of time and the temperature rise was measured before and after. Temperature rise was plotted against flow rate, showing an inverse proportional relationship between the two. This system used computer controlled heat pulses to generate temperature steps, and so derive flow velocity information. Circuitry and operation were simplified because of the linear temperature-resistance response of the PRTD (compared to a thermistor), although PRTD sensitivity to temperature change (Ω/°C) is an order of magnitude less. [A similar flow meter principle using 'thermally-coupled thermistors' is explored in Section 5.1.2 in this thesis.]

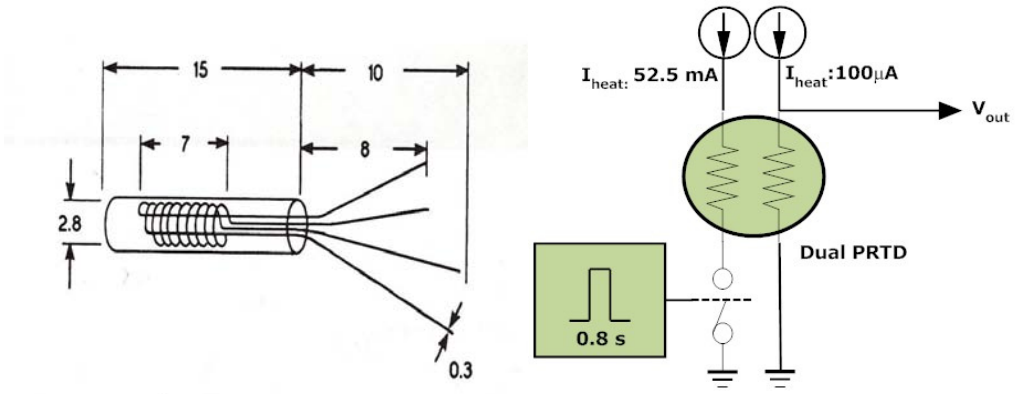

Figure 8 Pulsed double-PRTD thermal flow meter of Sonnenschmidt and Vaneslow (1996). The double PT100 on the left has dimensions in millimetres. The wires are two intertwined spirals of the same diameter.

2.2.9 A thermal gas-flow sensor using the digital oscillator technique

Van Oudheusden and Huijsing (1994) built a high sensitivity integrated gas flow sensor with and low response time using a pulse rate output. This was a device using the constant temperature operating principle, but it is interesting in that it used a digital technique using a thermal sigma delta technique to give a direct digital output rather than trying to convert the analog output of a bridge circuit into a digital signal. The device was built in silicon.

2.3 'Temperature rise' or 'thermal-field distortion' flow meters

Baker (2000) summarizes the characteristics of the second type of thermal flow meter that he terms a 'temperature rise flow meter'; this is shown schematically in Figure 9. This type of flow meter might also be referred to as a '***thermal-field distortion***' flow meter because the balanced heat field on either side of the heater under no-flow conditions is 'distorted' by fluid flow that carries heat downstream. This type of flow sensor uses matched temperature sensors (or differential temperature sensors such as thermocouples) to record both the magnitude and the direction of the flow. These systems are rarely used in open water bodies as they are better suited to the one-dimensional flows found in pipes.

Thomas (1911) created the first 'temperature rise flow meter' - shown in Figure 10 - for use in gas pipelines. This used an electrically heated grid in the pipe flow to heat the gas, and thermometers upstream and downstream to measure the resultant temperature gradient due to the energy transferred to the moving gas. The impact of his invention was limited by nervousness on the part of his masters in applying heat to the natural gas flowing in their pipelines.

Figure 9 Industrial thermal flow meter of the type described by Baker (1995)

Figure 10 Thomas flow meter, with a heating element inside the pipe and thermocouples used to measure the induced temperature gradient. From Baker (1995)

Laub (1947, 1956, 1957) placed the heat source and temperature sensors on the outside surface of the pipe, as shown in Figure 11. This removed a flow restriction within the pipe and the danger of electrical ignition in pipes carrying natural gas. The response time was slow because of the thickness of the pipe wall, and the output was unreliable because only the boundary layer was heated; this was affected by the Reynolds number, velocity profile and the viscosity of the gas.

Figure 11 The Laub flow meter placed the heating and sensor coils on the outside of the pipe for safety reasons. From Baker (1995)

These basic principles appeared again and again in the literature as the field of system-on-silicon and MEMS (micro electro-mechanical systems) burgeoned. Lammerink et al (1983), Van der Wiel et al (1993), Stenberg et al (1988) offer such examples, among many others. A typical example is given by Yang and Soeberg (1992) who built a monolithic flow sensor – shown in Figure 12 - for measuring millilitre per minute flows in liquid in a channel through the sensor.

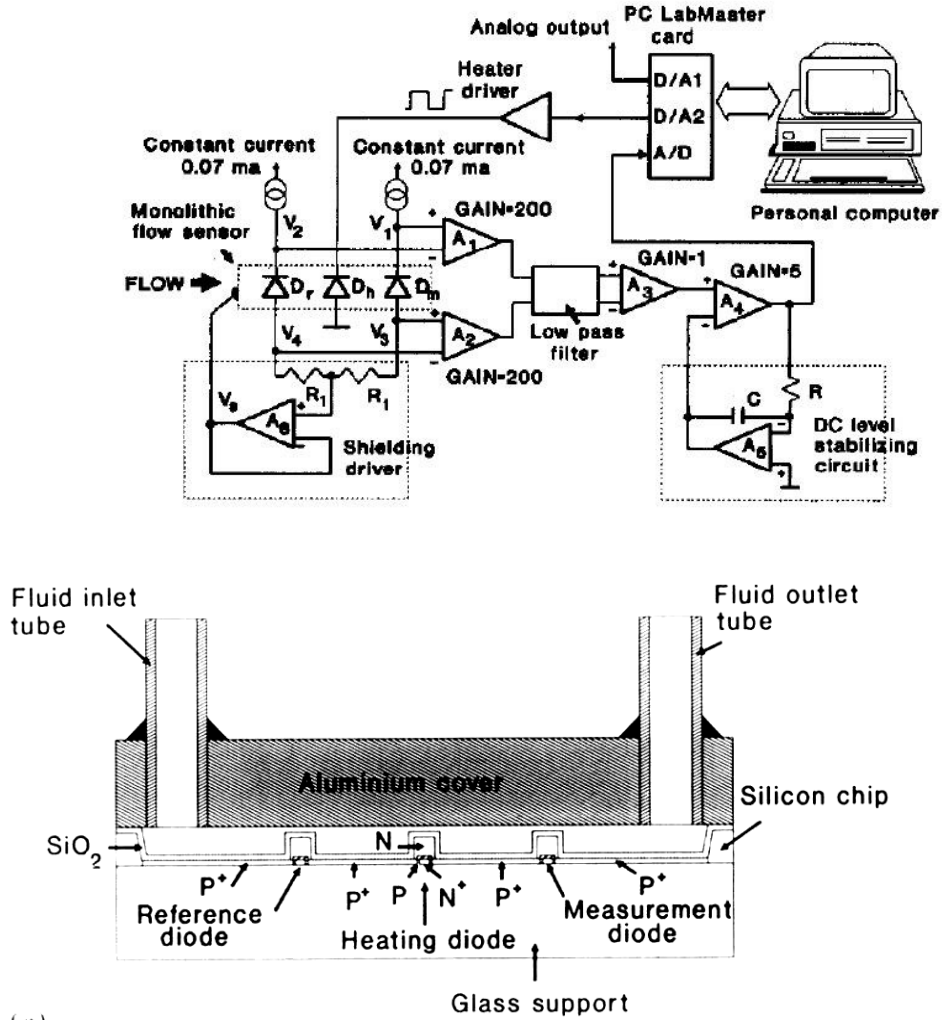

Figure 12 Monolithic flow sensor of Yang and Soeberg (1992) – circuit and physical layouts – operating in transit-time flow mode

Flows in this semi-conductor monolithic integrated flow sensor range down to 0.1 millimetre per minute flow rate. The device operates in both 'thermal transit time' ('heat pulse') mode for high accuracy and can also be used in 'thermal dilution' ('thermal field distortion') mode for high-speed measurements. The device uses on-chip diodes as the heaters and sensors, not because such diodes make particularly good temperature sensors,

but simply because they are easily fabricated in a sensor integrated onto a monolithic silicon chip.

"Heat balance" sensors (Baker and van Bavel, 1987) for sap flow measurements in growing plants are a variation of the Laub sensors. Manufactured by Dynamax USA, these sensors use additional radial heat flux measurements to determine sap flow by an energy balance method.

2.4 'Time-of-flight' thermal flow meters

'Time-of-flight' thermal flow meters are also known as 'heat pulse' flow meters and 'thermal transit time' flow meters. They measure the transit time of a sharp heat pulse injected into the fluid stream as it passes between two temperature sensors a fixed distance apart. Taniguchi and Fukuo (1993) used a heat-pulse flow meter in the throat of a seepage meter funnel to measure flow rates as low as 0.4 mm/s.

This work has been highly developed in sap flow measurements (comprehensively reviewed by Smith and Allen, 1996), culminating in the widespread usage of heat-pulse sap flow sensors (Edwards, 1986), dominating the other types of thermal sap flow sensors such as rate-of-heat loss sap flow sensors (Granier, 1985) and temperature-rise sap flow sensors (Baker and van Bavel, 1987). This body of work is vast; a separate 'sap flow' bibliography is provided in Appendix E: ***Sap Flow Bibliography***. While the heat-pulse technique has been widely used in scientific sap flow measurements, there is a real dependence on estimating the 'wounding factor' caused by inserting heated needles into the sap wood of a plant, rupturing xylem vessels and changing the heat transfer characteristics of the probes with time as calloused tissue forms around the probes. More importantly, the interpretation of sap flow data as an indicator of plant water stress is masked by the flow control mechanisms different crops use to regulate internal hydration (Loveys *et al* 2005).

2.5 Summary of literature review findings

2.5.1 Thermistor resistance-temperature characteristics

Thermistors feature a resistance sensitivity to temperature an order of magnitude higher than for the metal elements used in hot-wire anemometers, but this very non-linearity – shown in Figure 13 – limited the operating temperature range for early researchers in the field. This needs to be dealt with. These characteristics are well understood, however, via the Steinhart-Hart equation (Steinhart and Hart 1968) for converting thermistor resistance $\boldsymbol{R_T}$ to temperature $\boldsymbol{T}$. This is an inverse third-order logarithmic polynomial of the form

$$T(°C) = \frac{1}{a + b\ln(R) + c\ln(R)^3} - 273.15 \tag{2.4}$$

where ***a***, ***b*** and ***c*** are sensor-specific calibration coefficients used in converting thermistor resistance ***R*** (in ohms) to temperature ***T*** (°C). The constant ***273.15*** converts Kelvin temperature to Celsius. The conversion from temperature to resistance uses the same coefficients ***a***, ***b*** and ***c***

$$\alpha = \frac{a - \frac{1}{T + 273.15}}{c} \tag{2.5}$$

$$\beta = \sqrt{\left(\frac{b}{3c}\right)^3 + \frac{\alpha^2}{4}} \tag{2.6}$$

$$R(\Omega) = e^{\left(\beta - \frac{\alpha}{2}\right)^{\frac{1}{3}} - \left(\beta + \frac{\alpha}{2}\right)^{\frac{1}{3}}} \tag{2.7}$$

For sensing in the narrow range of water temperatures found in natural water bodies (-5°C to 45°C), this equation can be simplified by dropping the third order term $c.ln(R_T)^3$ and re-arranging the equation to

$$T(^0C) = \frac{a}{\ln(R_T) + b} - c \tag{2.8}$$

where ***a, b*** and ***c*** are coefficients determined during calibration. The coefficient ***c*** includes the conversion offset between Kelvin and Celsius temperature (K = ºC + 273.15).

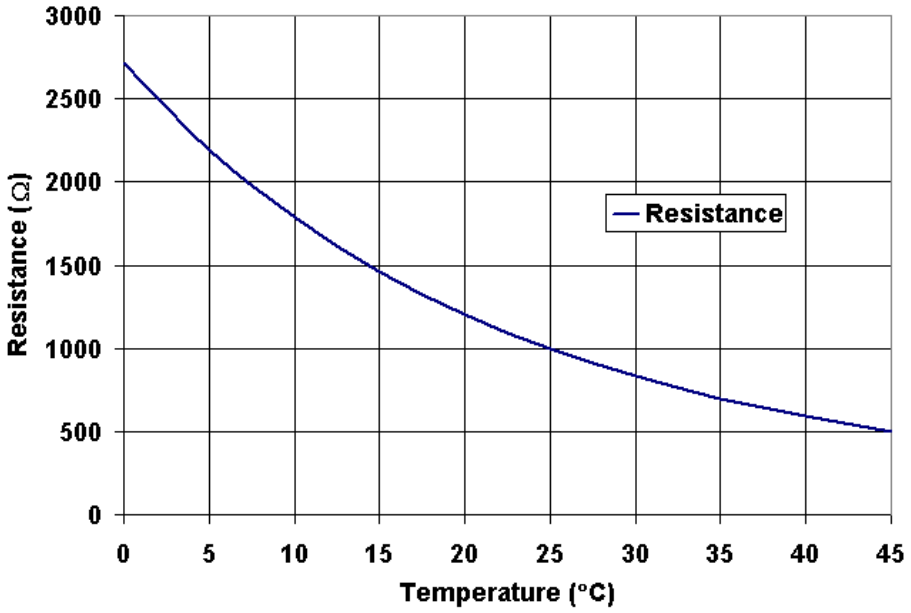

Figure 13 Resistance versus temperature response of a 1kΩ@25°C NTC thermistor measured with a 10µA excitation current

Whereas Equ. 2.4 fits data to ±0.0001ºC over the temperature range of -5°C to 45°C, Equ. 2.8 has an uncertainty of ±0.002ºC

2.5.2 The limitations of analog thermistor bridge flow meters

Returning to the prototypal Riedl and Machan analog thermistor bridge of Figure 4, errors due to non-tracking of the bridge as ambient temperature changes can be modeled using circuit analysis and thermistor resistance values calculated using Eqs. 2.5, 2.6, and 2.7 (both heated and unheated) over the ambient temperature range 5°C to 35°C. Would other thermistor/resistor combinations give smaller errors, given that the availability of different thermistor values has improved greatly in the intervening years? The bridge equation is: -

$$R_{T1} = R_1 * \left(\frac{1}{(R_2 / (R_2 + (R_{T3} * (R_{T2} + R_3) / (R_{T3} + R_{T2} + R_3))))} - 1\right) \qquad (2.9)$$

A non-linear regression program (based on Dennis *et al.* 1981) was used to determine the values of the series-parallel resistors. The error curves for the Rield-Machan Bridge over the limited temperature range of 5°C to 35°C for a mixture of commercial thermistor values ***T1***, ***T2*** and ***T3*** with optimal fixed resistor values in ***R1***, ***R2*** and ***R3*** can be seen in Figure 14. The best possible combination of ***T1***, ***T2*** and ***T3*** (***T1***=100Ω thermistor, ***T2***=1000Ω thermistor, ***T3***=2252Ω thermistor, all at 25°C) still gave errors greater than ±0.1°C, which are no better than those found by Riedl-Machan.

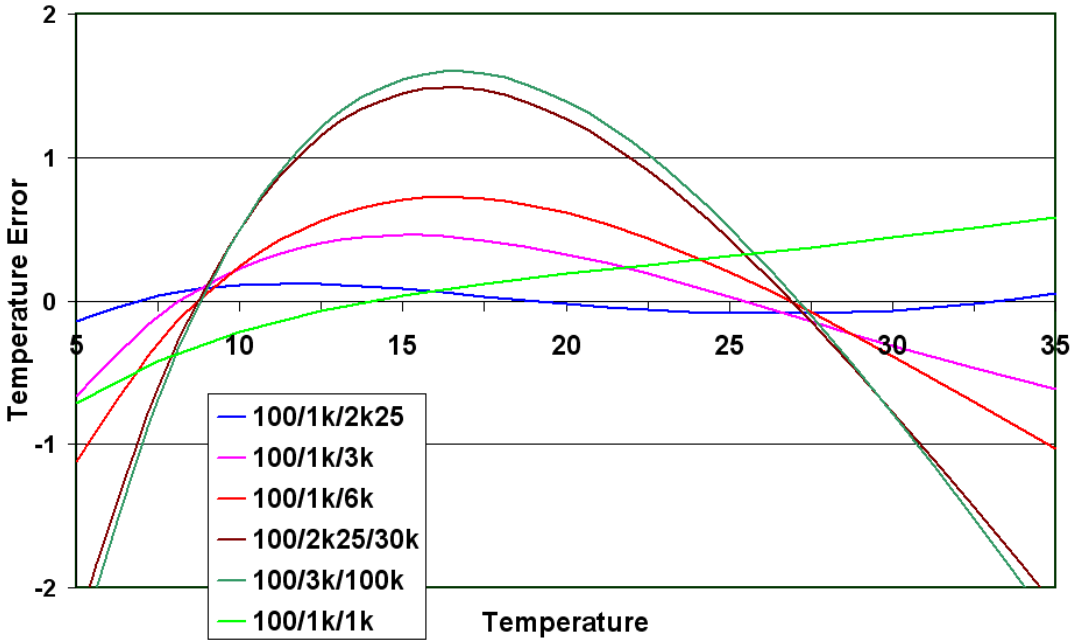

Figure 14 Error curves for the Rield-Machan Bridge over the limited temperature range of 5°C to 35°C for a mixture of commercial thermistor values *T1*, *T2* and *T3* with optimal fixed resistor values in *R1*, *R2* and *R3*.

A number of salutary lessons arise from this model of a simple analog-bridge thermistor flow meter: -

1. No account has been taken of the tolerance errors in the thermistors (up to ±20% in glass bead thermistors) or the various bridge resistors (typically ±1%); these are likely to increase the bridge tracking uncertainties.
2. This type of bridge has no ability to make a separate measurement of the ambient water temperature - a measurement that would be useful for correcting known errors in the bridge response.
3. The magnitude of the errors seen in Figure 14 range from ±0.2°C to ±2.0°C for a warm-thermistor flow meter operating with a limited 4-5°C over-temperature setting with respect to ambient.

One must therefore conclude that, while bridge compensation thermistors were a necessary evolutionary step in improving warm thermistor flow meters, little improvement is possible beyond the fairly coarse measurements made by this type of technology. Some other circuit and digital correction techniques will be necessary to make high-precision flow measurements using warm thermistor technology. These design challenges are addressed in Chapter 5.

2.5.3 Thermistor flow meters for very slow flows

The literature review suggests that a 'constant power' flow meter appears to have a number of advantages over a constant over-temperature flow meter. Yang et al (1998) - measuring volumetric fluid flow $\boldsymbol{Q}$ in a pipe - used a simplified empirical form of the King Equation to describe the (restated from Eq. 2.2) relationship between flow rate $\boldsymbol{Q}$ and rate of heat loss $\boldsymbol{P}$ at an over-temperature condition of $\boldsymbol{T}$-$\boldsymbol{T_A}$

$$P = \left(K_1 + K_2 \cdot \sqrt{Q}\right) \cdot (T - T_A)$$

where $\boldsymbol{K_1}$ and $\boldsymbol{K_2}$ are constants depending upon geometric factors, the structure of the surface of the measurement probe and the thermal properties of the liquid. $\boldsymbol{T}$ and $\boldsymbol{T_A}$ are the temperature of the measurement probe and the fluid respectively.

The original design concepts for the analog bridge developed during this thesis in Chapters 5, 6 and 7 began by re-arranging Eq. 2 such that the rate of heat loss $\boldsymbol{P}$ is kept constant, while the over-temperature value $\boldsymbol{T}$-$\boldsymbol{T_A}$ is monitored to determine flow speed $\boldsymbol{v}$

$$Q = \left[K_2 \cdot \left(\frac{P}{T - T_A} - K_1 \right) \right]^2 \tag{2.10}$$

Eq. 2.10 indicates an inverse square relationship between flow and measured temperature difference. While this grossly non-linear transfer function would severely limit the range of flow speeds over which the sensor could operate, it would greatly increase its sensitivity to the very slow flow rates often found in environmental flow measurements.

Secondly, a warm thermistor flow meter operating in constant power mode offered the promise of being less susceptible to the effects of bio-film build-up upon the probe surface when it is placed in a biologically active natural water body. The sensor would simply need to raise its internal temperature to continue to push a constant amount of heat into the flow stream, maintaining similar external heat fields to those developed during the calibration process, albeit from a slightly larger spherical volume. Bio-film build-up would result in a long-term drift of operating temperature (which could not be removed by post-processing of data), while allowing continued observations of short-term velocity changes. In constant over-temperature flow meters, by comparison, the sensor's internal temperature is purposefully held constant with respect to ambient temperature, despite being inside an insulating bio-film jacket. A larger portion of this fixed temperature gradient would appear across the bio-film, reducing the amount of heat injected into the fluid, so that the sensitivity of the instrument might be expected to fall away over time. The effects of biofilm build up on thermistor sensors have not been tested in the course of this thesis.

Finally, from a sensor design viewpoint, constant power flow meters use temperature measurements $\boldsymbol{T_A}$ and $\boldsymbol{T}$ rather than electrical power $\boldsymbol{P}$ as their output measurands. Therefore the calibration process depends upon a single common temperature standard. If measurement of both ambient temperature $\boldsymbol{T_A}$ and over-temperature $\boldsymbol{T}$ are both made at the same point with the same thermistor, errors due to mismatched thermistor pairs (found in the other constant temperature warm thermistor flow meters described in the previous sections) could be avoided, as could the spatial temperature variations. Temporal variations in fluid temperature remain a source of error, as these two temperature measurements $\boldsymbol{T_A}$ and $\boldsymbol{T_F}$ need to be made consecutively with a discreet time interval between them. In very slow flow situations, however, slowly changing background temperature gradients can be measured beforehand and extracted from the final measurement by extrapolation. This constant-power warm-thermistor flow

measurement technique therefore offered the possibility of simplifying the sensor calibration process to one of temperature measurement. Sensor output power - held constant by the control circuit – would not need to be measured or computed as the flow proportional variable, as is the case with constant over-temperature flow meters. The advantage of this technique is that a single thermistor is perfectly matched with itself, as one is measuring at two separate points along an established temperature response curve.

However, circuit requirements in a constant power flow meter would be more complex, as the feedback control system must seek to maintain the variable ***power*** at a constant value, rather than simpler variables such as thermistor voltage or current.

2.5.4 The problem of buoyancy in 'Rate of Heat Loss' sensors in open water bodies

However, a second problem, namely ***buoyancy***, affects the minimum flow speed detectable by thermal flow meters. Buoyancy effects occur because the warmer water surrounding the sensor elements expands and becomes less dense than the surrounding fluid, causing it to rise and taking heat away from the sensor.

Collis and Williams (1959) looked at two-dimensional convection for heated wires at low Reynolds numbers. They pointed out that free convection may have caused the departure from the logarithmic relationship for temperature difference versus flow rate in their sensor at flow speeds below 3mm/s. Hinze (1975) determined that free convection would contribute to heat transfer when the Reynolds number ***Re*** was less than the Grashof number ***Gr*** raised to the 1/3 power. For a thermistor bead with a diameter of 1.52mm and a 10°C overheat, ***Re*** equals $\boldsymbol{Gr}^{1/3}$ when the flow speed is 3 mm/s. MacIntyre (1986), using a two-thermistor bridge flow meter based on Figure 5, also pointed out a departure from the expected curvature at very low velocities. She attributed this to buoyancy effects. She also pointed out that the orientation of the probe affected the reading at very low flows because of buoyant pockets of water moving from the heated sensor to the reference sensor and changing the balance of the bridge.

'Rate of heat loss' sensors in open-water body flow meters would therefore appear to be limited by sensitivity to size and buoyancy effects to flow rates above about 3 mm/s. ***This thesis will specifically explore the measurement of flow rates below 3 mm/s where buoyancy forces have a significant effect on sensor response.***

2.5.5 Future directions from the literature

Application-specific literature reviews have been included elsewhere in this thesis at the beginning of each chapter. Taking these into account, and the preceding review, one must conclude that there has been little advance in the use of thermistors in flow metering

applications since the late 1980's, particularly in the largely unexplored territory of the very slow flows that occur in nature. One can only surmise that environmental monitoring programs have lacked the resources, personnel and funding that drove innovation in industrial flow metering. Yet these real and increasingly important environmental flows transport water, salts, leachates and nutrients in ecological systems such as soils, plants, surface and ground water systems.

The sensitivity of thermistors and analog circuitry might easily be overlooked amidst the frenzy of activity in modern digital electronics, telecommunications and computing. Yet analog circuits and devices offer the special advantages of infinite sensitivity and resolution within sensors and instruments operating in the very real analog environment that surrounds us. The aim of this thesis is to explore 'very slow flows in environmental engineering'. Therefore it seems appropriate to re-visit these older circuits with a view to improving them through the use of modern circuits, components and methods.

What is very clear from the literature on analog thermistor flow meters is that difficulties exist in pushing down to the measurement of ever-slower flow rates. Off-the shelf thermistors used in 'rate-of-heat loss' analog bridge circuits give only crude matching to ±0.1°C at best and are subject to further uncertainties because of the broad tolerance levels of typical submersible glass-bead thermistors. Difficulties in correcting these devices for temperature-dependent errors arise because these bridges cannot easily be switched between low power mode $\boldsymbol{P_A}$ to measure ambient temperature and high power flow measurement mode $\boldsymbol{P_H}$, where $\boldsymbol{P_A}$ is typically equal to $\boldsymbol{P_H/1000}$.

Spatial errors also occur with various authors reporting problems with the placement of the second ambient-correction thermistor in the flow stream. Either spatial temperature gradients occur naturally, or the heated plume from the measurement thermistor in the thermal flow meter affects the proximate ambient sensing thermistor to cause thermal feedback problems.

Finally, the need to match thermistors in this way has historically limited the temperature range over which these thermal flow meters have operated. Use of a single thermistor can mitigate this need to match thermistor response and thermal gradients as it is inherently self-referencing and will therefore operate over a far wider temperature range. Nevertheless, thermistor-matching techniques remain critical if the flow meter technique is to use the 'heat pulse' or 'thermal-field distortion' method used in sap flow and seepage meter applications by other authors. Such matching must, however, be a process of calibrating individual thermistors against a common standard in a well-mixed

isothermal bath, rather than a process of trying to select off-the shelf thermistors and matching them via a sorting process.

Thermal flow meters have relied on the traditional 'constant temperature' technique. Exploration of a 'constant power' technique seems merited on the grounds that thermistors located in natural water bodies are likely to experience the build-up of bacterial bio-films that will contribute to long-term drift.

The use of 'constant power' mode also offers the advantage of a single temperature calibration standard. 'Constant temperature' thermal anemometers, by comparison, seek to hold temperature constant while measuring both ambient temperature and delivering a power-based output.

A further limitation to the measurement of very slow flows has to be the essential nature of thermal flow sensors. In generating heat, they inevitably create a thermal plume whose buoyant convective up-thrust will carry heat away from the sensor, especially when cross-flows to be measured are likely to be slower than these self-same vertical buoyant plume flows. Rather than attempt to cancel these flows, methods need to be found to work with them if flows below 3 mm/s are to be measured.

Finally, analog circuitry offers wide dynamic range, infinite resolution and rapid response to a changing environment, especially when one is changing operation power levels over three orders of magnitude and still expecting to dig small temperature changes of a few thousandths of a degree out of the resultant signal.

These, then, are the electronic design challenges necessary to tackle very slow flows in environmental engineering. It is also clear that adequate modeling, laboratory, manufacturing, calibration and field techniques will need to be engineered to put such technology to use.

Chapter 3. Using smart sensor strings for continuous monitoring of temperature stratification in large water bodies

Skinner, A.J. & Lambert, M.F. (2006). Using smart sensor strings for continuous monitoring of temperature stratification in large water bodies. *IEEE Sensors, v. 6 (6), pp. 1473-1481*

3.1 Background

This first paper sets the scene for low-cost precision measurements in natural water bodies by describing the development of a thermistor string based upon a single 3-wire cable with sensors placed along it like beads on a necklace. The 'smart-sensor string' that evolved was predicated on the use of the 3-wire SDI-12 bus used by environmental data loggers to power and collect high-resolution data from sensors having in-built intelligence and calibration to a reference standard. That such measurements of thermal stratification in suburban water reservoirs were even necessary arose from work by Lewis *et al* (2003) within the Adelaide University in South Australia. Lewis' research investigated the performance of surface mixers in de-stratifying the vertical water column in order to reduce the growth of cyano-bacteria (blue-green algae) that was affecting water quality during the summer months in South Australia.

The high-resolution measurement circuits in the first systems – shown in Figure 17 – used the SDI-12 sensor bus to collect high-resolution temperature data. However, they

still used multiple thermistors hanging from a surface raft, had separate temperature compensation for thermal errors in the electronics located at the surface – shown in Figure 18 – and had no facility to compute thermistor temperature directly within the ADC's microcontroller. A photo of one such early raft-based system appears in Figure 15.

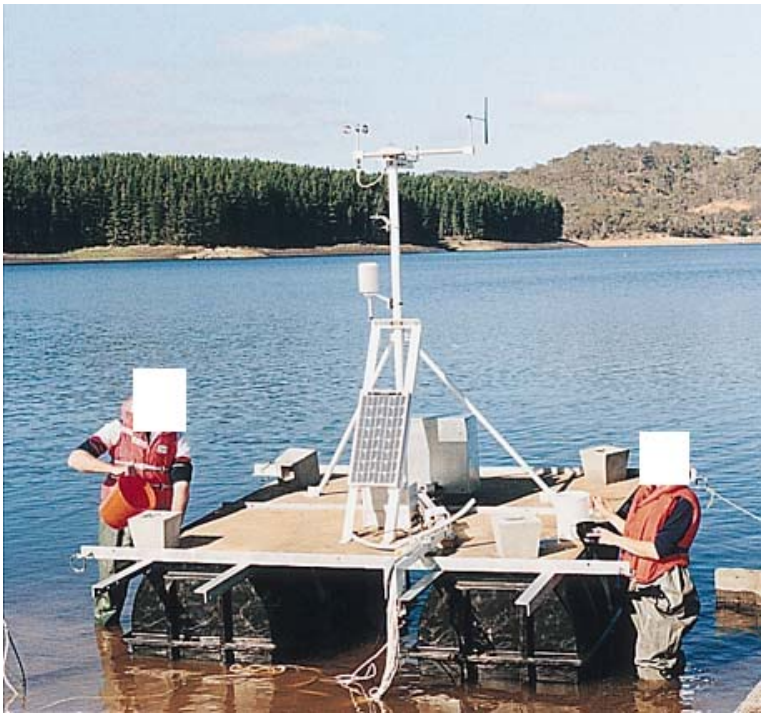

Figure 15 Lewis (on the left) of the University of Adelaide installing an early raft-based stratification system in the Myponga Reservoir in South Australia. The multi-channel ADC electronics is installed in the enclosure at the rear of the raft. The multiple individual thermistors can be seen hanging over the front of the raft (white cables).

Early calibrations required a 7-parameter non-linear regression which could not be easily automated because of the difficulties of setting starting parameters that gave a convergent solution. The calibration coefficients for each thermistor were stored in the destination computer, not in the sensor, giving rise to the need to post-process raw voltage data from the data logger to determine precision temperature values. Early development work led gradually to the increasing simplification and improvement to the measurement circuitry in the form of a switched bridge circuit as ratiometric measurements replaced external voltage references to the thermistor sensor ADC. Sensor resolution was improved (post publication, Figure 23) to 16-bits, 0.001°C, and no 'flat-spots' in the sensor response. The following background material describes the development process.

3.1.1 Development of a new SFVC ADC for sensors

Analog-to-digital converters (ADCs) have been around as long as digital electronic circuits have been used to make measurements. Resolution, speed and accuracy

have improved year after year while the cost and physical size of these devices has fallen. The literature on these devices is vast and all encompassing, so the question must be asked: why invent another ADC? The answer is that there ***is*** no justification in a commercial sense, but that the mental space to explore new ideas allowed by the PhD process also allowed investigation into the possibilities of reducing the cost of 'smart sensors' by integrating the ADC and the sensor element more closely with the sensor microcontroller. And so a highly linear and stable 16-bit ADC was developed, based on the addition of a single low-cost op-amp acting as a charge-balance integrator between the sensor and the microcontroller, enabling the construction of affordable smart sensors for environmental monitoring. That this design work succeeded at all owes much to the lack of commercial imperatives, deadlines and budgets. It owes almost nothing to the literature, which served only to provide the 'seed' circuit topology – the commercial Analog Devices AD652 synchronous voltage-to-frequency converter. A description of the commercial AD652 device, and how its design was simplified, appears in the following sections.

3.1.2 The AD652 Synchronous Voltage-to-Frequency Converter: Product Description

[This descriptive material, in quotation marks, closely follows the manufacturer's data sheet, Analog Devices AD652, 1995, Figure 16]

"The AD652 synchronous voltage-to-frequency converter (SVFC) is a powerful building block for precision analog-to-digital conversion, offering typical non-linearity of 0.002% (0.005% maximum) at a 100 kHz output frequency. The inherent monotonicity of the transfer function and wide range of clock frequencies allow the conversion time and resolution to be optimized for specific applications."

"The AD652 uses a variation of the charge-balancing technique to perform the conversion function. The AD652 uses an external clock to define the full-scale output frequency, rather than relying on the stability of an external capacitor. The result is a more stable, more linear transfer function, with significant application benefits in both single- and multi-channel systems."

"Gain drift is minimized using a precision low drift reference and low temperature coefficient, on-chip, thin-film scaling resistors. Furthermore, initial gain error is reduced to less than 0.5% by the use of laser-wafer-trimming."

"The analog and digital sections of the AD652 have been designed to allow operation from a single-ended power source, simplifying its use with isolated power supplies."

NOTE:
This figure is included on page 40 of the print copy of the thesis held in the University of Adelaide Library.

Figure 16 The AD652 Monolithic Synchronous Voltage-to-Frequency Converter used as the basis for the development of a new type of charge-balance ADC for environmental sensors.

Selected Product Highlights

1. "The use of an external clock to set the full-scale frequency allows the AD652 to achieve linearity and stability far superior to other monolithic voltage-to-frequency converters (VFCs). By using the same clock to drive the AD652 and set the counting period (through a suitable divider), conversion accuracy is maintained independent of variations in clock frequency.
2. The AD652 synchronous voltage-to-frequency converter (SVFC) requires only one external component (a non-critical integrator capacitor) for operation.
3. The AD652 includes a buffered, accurate 5 V reference."

Theory of Operation

"A synchronous VFC is similar to other voltage-to-frequency converters in that an integrator is used to perform a charge-balance of the input signal with an internal reference current. However, rather than using a one-shot as the primary timing element, which requires a high quality and low drift capacitor, a synchronous voltage-to-frequency converter (SVFC) uses an external clock. This allows the designer to determine the system stability and drift based upon the external clock selected. A crystal oscillator may also be used if desired."

(cont.) "The SVFC architecture provides other system advantages besides low drift. If the output frequency is measured by counting pulses gated to a signal that is derived from the clock, the clock stability is unimportant and the device simply performs as a voltage-controlled frequency divider, producing a high resolution A/D. If a large number of inputs must be monitored simultaneously in a system, the controlled timing relationship between the frequency output pulses and the user-supplied clock greatly simplifies this signal acquisition. Also, if the clock signal is provided by a VFC, the output frequency of the SVFC is proportional to the product of the two input voltages. Therefore, multiplication and A-to-D conversion on two signals are performed simultaneously."

"Since each reset pulse is identical, the AD652 SVFC produces a very linear voltage-to-frequency transfer relation. Also, because all reset pulses are gated by the clock, there are no problems with dielectric absorption causing the duration of a reset pulse to be influenced by the length of time since the last reset."

3.1.3 An early SVFC thermistor ADC design

The final thermistor temperature ADC developed in this chapter and reproduced in Figure 23 operates in a similar but simpler manner to the AD652 synchronous voltage-to-frequency converter (SVFC) described in section 3.1.2. The intermediate steps in its development can be seen in Figure 17 and Figure 18, but in summary a number of key modifications have been made to the original AD652 design: -

1. The sensor buffering stage required in Figure 16 is not required, as the integration current is controlled directly by the thermistor operating in constant-voltage mode. V_{in} in Figure 16 is grounded, R_{in} is replaced by a high-impedance thermistor, with the non-inverting input of the integrator setting the voltage across the thermistor.
2. Use of constant voltage mode eliminates the need for the switchable 1mA current source of Figure 16 between integrator input and output. Instead, the reset current is created during reset periods by switching the sensor microcontroller's port pin from a high-impedance input state during integration to an output drive state during reset. A fixed resistor between fixed voltage levels ensures a constant reset current.
3. The flip-flop logic of Figure 16 has been removed and replaced by firmware logic in the microcontroller.
4. Analog switches are replaced by the FET switches within the microcontroller.

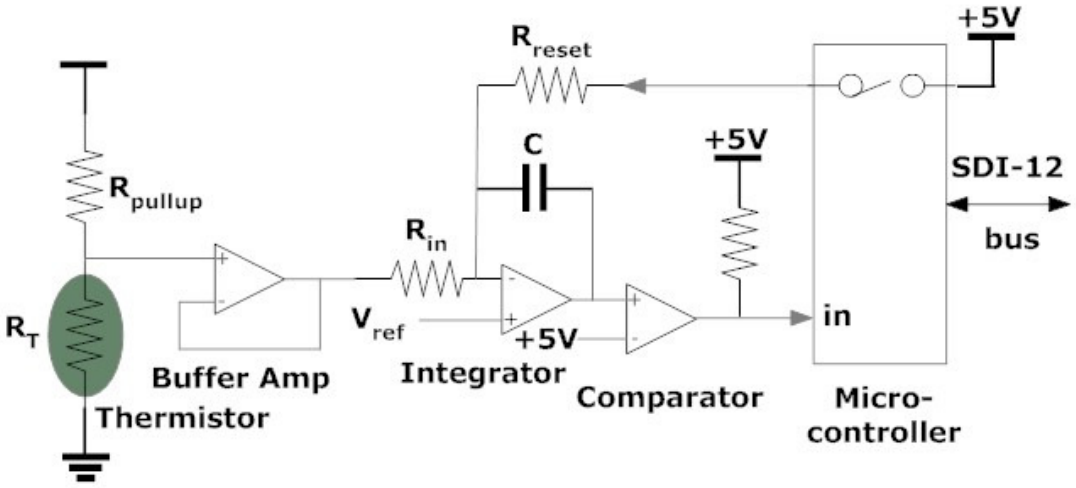

Figure 17 An early SVFC thermistor ADC design. It is essentially a buffered voltage divider network followed by an active-low SVFC ADC formed by the integrator and comparator. V_{ref} is 1.23V and is derived ratiometrically from the LM2951 +5V regulator powering the thermistor divider, the comparator reference and the microcontroller. This design was used with remote thermistors on the end of a two-wire cable, often up to 30m from the ADC located in an enclosure on a surface raft as in Figure 15 or on a wooden pole driven into the sediment.

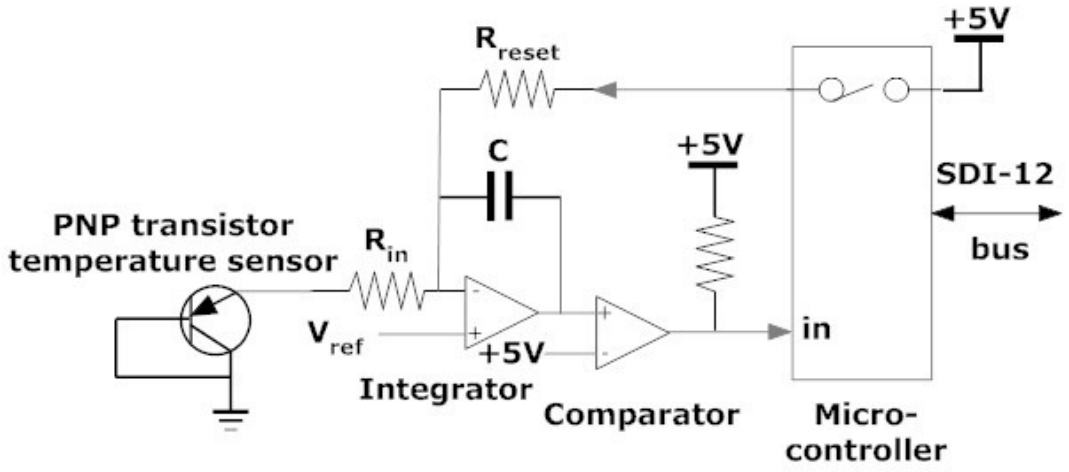

Figure 18 The remote thermistor of Figure 17 – submersed in the water column - was almost always operating at a different temperature to the electronics on the surface raft. This necessitated a separate measurement of the temperature of the ADC electronics. This was accomplished by this parallel ADC channel using a PNP diode-connected bipolar transistor as a temperature sensor. Small changes in the thermal voltage *kT/q* of the transistor's base-emitter voltage due to temperature fluctuations changed the input current of the ADC and hence its *count* output. This particular circuit gave rise to the possibility of a ground-referred thermistor in place of the PNP+R_{in} combination to measure temperature in an isothermal environment created by potting the ADC, thermistor, 5V regulator and microcontroller in close proximity. This reduced the difficulties in finding a convergent solution to the 7-parameter calibration associated with this separate temperature measurement solution.

5. Power provided to the ADC circuitry is derived directly from a microcontroller port pin; this allows power-down energy saving when measurements are not being made.

6. The crystal-locked frequency is derived from the microcontroller clock. Because the counter period and the reset pulse are both derived from the same clock, clock drift has no effect on the output '***count***' of the ADC
7. Ratiometric resistance networks referenced to the +5V microcontroller supply minimize errors. This design is essentially a 'switched bridge' ADC

Low-cost component temperature coefficients are corrected for in the calibration algorithm

In summary, the analog-to-digital converter is a modified charge-balance circuit consisting of an integrator followed by a comparator. Timing, logic and switching functions are implemented in the CMOS microprocessor. The same microcontroller processes measurement and communication commands on the SDI-12 interface bus.

3.1.4 Development of an integrated temperature sensor

Development of the final sensor shown in Figure 19 and Figure 21 and described in the IEEE Sensors paper at the end of this chapter required a number of new ideas. It seemed logical to embed the sensor and sensor electronics at a single point along a submersible rubber cable, if for no better reason than to reduce the tangle created by thirty thermistors of different lengths fastened along a mooring wire.

More importantly, potting the thermistor and ADC electronics at a single point reduced the number of calibration parameters needed from seven to two, as temperature corrections for the sensor electronics could now be included in the calibration of the sensor itself, provided that an iterative process was used in the computation to converge on a 'sensor temperature'. This opened the door to an automated calibration process, at the end of which sensor calibration coefficients could be written back into the EEPROM coefficient memory of the sensor.

The in-line sensors, once developed in hardware, had the ability to communicate over the SDI-12 bus, but this left little available program space to do the necessary on-board calculations of the final temperature. Much code space was being taken up by the natural logarithm function needed to calculate the Steinhart-Hart Equation.

A simpler approach was attempted using an approximation to a binary logarithm; this is described in ***Appendix B: 'Binary logarithms for solving the Steinhart-Hart Equation'***. This method left small temperature errors; these could be corrected by a look-up table when computing the basic logarithm. This in turn, allied to some background reading on the history of scientific invention and the first mechanical computers, led to the work of Charles Babbage in 1832 (Swade, 2000).

Figure 19 Twenty-four sensor circuit boards are shown before being broken-out from the PCB panel form in which they are manufactured. They are shown linked by ribbon cable (top) to power, program and test them prior to encapsulation. They are then potted inside a threaded PVC tube with a cable-gland and O-ring at each end. A heavy-walled adhesive heatshrink is then shrunk over the whole assembly to form a third level of waterproofing (bottom).

Babbage also attempted to compute complex trigonometric curves using the sort of simple arithmetic functionality available in mechanical systems and latter-day sensor microcontrollers. Research into the Babbage's 'Difference Engine' (which he only partially built) brought to light the 'Method of Differences' (the use of finite difference techniques) introduced by the English mathematician Henry Briggs in the sixteenth century. This method promised the possibility of generating precision calibration curves 'in-situ' within the sensor using nothing more than the simple addition processes already native to the sensor's microcontroller. Difficulties arose in the Method of Differences because it became necessary to fit a seventh-order polynomial to the curve of interest, using 32-digit numbers to prevent the result from diverging due to cumulative errors after thousands of additions. Excel works with only 64-bit numerical precision, whereas 128-bit precision was needed. Simulating 15-byte numbers in Excel and automating the addition processes to test for curve divergence errors solved this problem and gave some confidence that the method would work if implemented in the sensor operating code.

The Method of Differences allows a numerically-challenged sensor to calculate temperatures to the required precision of 0.001°C, albeit slowly. A faster technique was developed – in theory only - for calculating the current temperature relative to the previous computed temperature by allowing the table to unwind backwards, rather than always counting forwards from a low temperature starting point. However, this technique required extra RAM memory for the storage of an additional scratchpad table needed for subtractions. This was just unavailable in the low cost sensor's microcontroller, and therefore not implemented.

It also became obvious that the effort required to compute the starting value table for each individual sensor after calibration would be onerous in the extreme. Nor did this technique lend itself to easy automation because of the aforementioned difficulties of having to use 128-bit number systems to do the computations. So a promising new computational technique was sidelined because of the difficulties involved in using it to calibrate large numbers of individual sensors.

3.1.5 Use of 'standard curves' for linearizing non-linear sensor response

Calibration of early sensor strings showed that all sensors – despite the poor tolerances of their componentry – all followed a standard curve, albeit with slight apparent differences in offsets and gains (Figure 20). A simple linear regression of any of these curves to a nominal 'standard curve' always produced a simple linear fit; this opened up several new possibilities.

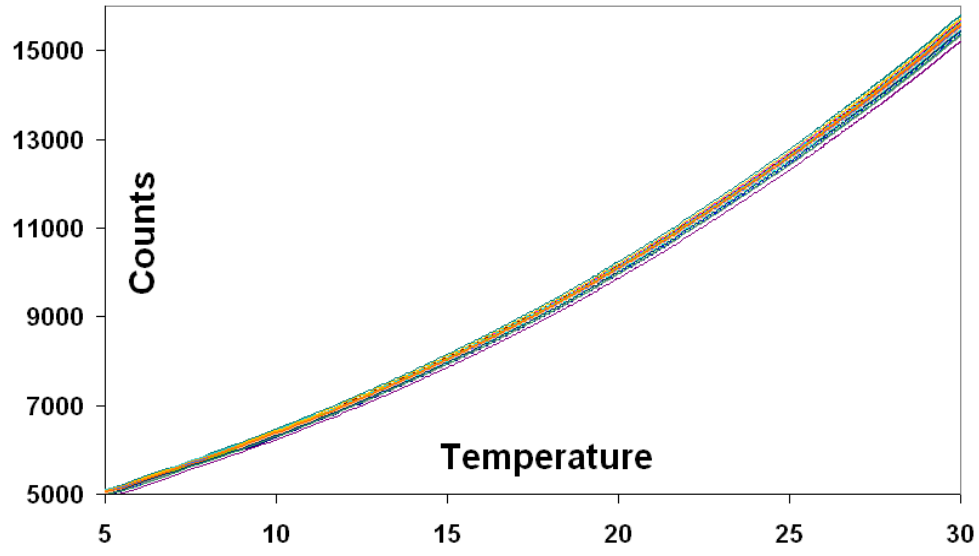

Figure 20. The 'count versus temperature' transfer functions of 26 randomly selected production sensors all follow the same basic curvature. Applying small offset and gain terms to each curve matches all sensors over the operating temperature range to within ±0.006°C, while effectively linearizing the calibration process.

Firstly, the Method of Difference technique already developed was capable of generating just such a standard curve, based on the response of a single sensor calibrated carefully over the full temperature range. This 'standard sensor' curve could be represented by a single standard 'starting value' table loaded along with the sensor's firmware, avoiding the issue of having to customise a table for each new calibration. But the second opportunity created by an apparently 'linear sensor' was two-fold. Laboratory calibration now became a two-point process, rather than a much longer multi-point non-linear regression problem. Even more importantly, probes could be 're-matched' in the field by bundling probes together and placing them above and below the thermocline[6] to obtain two different calibration points. This provided a field method (Figure 21) of correcting for long-term temperature drifts that cannot be accounted for in the initial calibration, and without having to return the sensor strings to the laboratory for long periods, with the associated loss of field data.

3.1.6 Improving sensor resolution and linearity

The evolution of these sensor strings continued after the IEEE Sensors paper was published. It was found that sensor resolution could be improved from 15-bits to 16-bits (0.003°C to 0.001°C) by simple firmware changes. While this measurement took a little longer, this was compensated for by returning to the use of natural logarithms and the full Steinhart-Hart calibration equation, rather than the simpler form used in the paper which took longer to compute. All this was made possible by the commercial release of a microcontroller with double the program memory space.

The problem of 'flat-spots' of a few milliKelvin in the sensor's response curve was traced to an internal feedback phenomena within the power-supply pin inside the ADC's LM392 op-amp/comparator chip shown in Figure 22. This problem disappeared when these two components were physically separated as seen in Figure 23. (For details, see ***Appendix D: 'Failure of monotonicity of the ADC'***). This cut component cost even further by using a single external op-amp and the microcontroller's on-board comparator to produce a 16-bit temperature-compensated ADC. The ADC design effort could now be justified retrospectively; it was cheaper and more stable than commercial ADCs of similar resolution, although significantly slower.

While circuit and firmware algorithms were being refined, so too were the mechanical assembly and calibration processes. Various metal and plastic instrument

[6] The thermocline is the sharp temperature boundary in a temperature-stratified water body between the sun-warmed upper layer (the epilimnion) and the cold stable bottom layer (the hypolimnion)

housings were tried before settling upon the pressure-proof method described in the paper and shown in Figure 19 and Figure 21.

Field results from the paper can be found under ***Appendix A: 'Selected field data from temperature sensor strings'***. The field results justify the level of precision sought and achieved in matching and operating these sensor strings, and demonstrated how other environmental sensors – such as the seepage meter described in this thesis – could be satisfactorily connected via a 3-wire rubber cable while fully submersed in a natural water body.

Figure 21 A sensor string bundled together for two-point in-field calibration at the Torrens Lake in Adelaide South Australia

NOTE:
This figure is included on page 48 of the print copy of the thesis held in the University of Adelaide Library.

Figure 22 A 15-bit integrated thermistor temperature charge-balance ADC, published in IEEE Sensors in December 2006

Finally, many buoy structures were developed to support these sensor strings but are not included in this thesis, although they complete the picture describing the lengths one must go to in order to successfully evolve and deploy new field instrumentation. A selected sample of these may be seen in ***Appendix A: 'Selected field data from temperature sensor strings'***.

In summary, the IEEE Sensors paper arising from this chapter on smart-sensors describes

1. a charge-balance 15-bit ADC based upon an op-amp/comparator combination,
2. ratiometric reference points using voltage dividers across the sensor microcontroller's 5V supply rather than more expensive voltage reference sources
3. a new 'standard curve' generator for simplifying calibration in laboratory and field to a two-point calibration

4. the concept of a bulk circuit temperature coefficient to correct circuit thermal drift by ensuring close thermal-coupling of the thermistor temperature element with the ADC circuit
5. new submersible sensor encapsulation techniques
6. sensor matching to within ±0.006°C by common calibration in an isothermal water bath

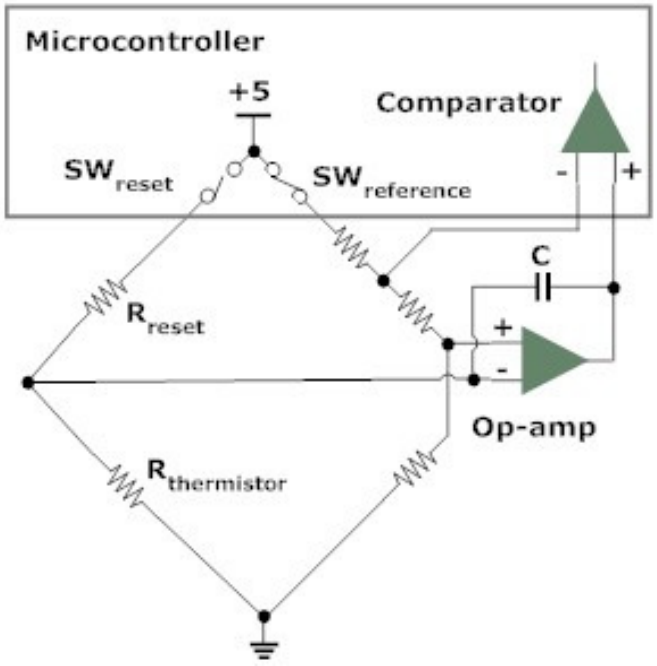

Figure 23 An improved 16-bit integrated thermistor temperature charge-balance ADC, developed and field tested extensively after the original sensor was published in IEEE Sensors in December 2006. The separation of the op-amp and comparator (previously in a single 8-pin DIP package) resolved issues with 'flat-spots' in the temperature response curves due to internal IC feedback problems on the shared supply pin at harmonics of the SVFC clock, as explained in Appendix D

Circuit concepts from this charge-balance ADC were extended and improved for use in creating a four-electrode electrical conductivity (EC) sensor and platinum resistance temperature sensor (PRTD) for use in quantifying the salt levels in water or soils. These circuits are described in detail in Chapter 4.

Paper
Skinner, A.J. and Lambert, M.F. (2006). 'Using smart sensor strings for continuous monitoring of temperature stratification in large water bodies.' IEEE Sensors, Vol. 6, No. 6, December 2006

Chapter 4. An automatic soil pore-water salinity sensor based on a wetting front detector

Skinner, A.J. & Lambert, M.F. (2009). An automatic soil pore-water salinity sensor based on a wetting-front detector.
IEEE Sensors, v. 11 (1), pp. 245-254

4.1 Background

The 1.06 million square-kilometer Murray-Darling Basin shown in Figure 24 in south-eastern Australia contains 71% of Australia's irrigated crops and pastures, accounting for 41 per cent of the nation's gross value of agricultural production (Australian Bureau of Statistics 1992). Rising salinity levels at the western outflow end of the catchment are a serious cause for concern (Jolly *et al.*, 1997). Hundreds of tonnes of salt per day have historically entered the bottom reaches of the Murray River in South Australia alone. Tree clearing for agriculture has resulted in widespread dry-land salinity, but irrigation areas alongside the river have exacerbated this problem. Plants increase soil salinity by extracting fresh water from brackish water during transpiration, leaving salts behind to accumulate in the soil. The use of already-saline irrigation water on perennial crops necessitates the addition of a 'leaching fraction' to the amount of irrigation water applied; this extra water is designed to flush toxic salts out below the crop root-zone. Such root-zone leaching has the unintended consequence of putting pressure on local aquifers, leading to mobilization of groundwater towards the river at the lowest point at the landscape. This adds further salt to the river water, which is in turn recycled further downstream onto other crops and other aquifers. Monitoring the build-up of salt in soils

under irrigated agriculture has, however, been far more complicated than the measurement of salt in the irrigation water itself.

The paper at the end of this chapter takes up this theme, and develops such sensors based on the wetting-front detectors developed by CSIRO's Dr Richard Stirzaker.

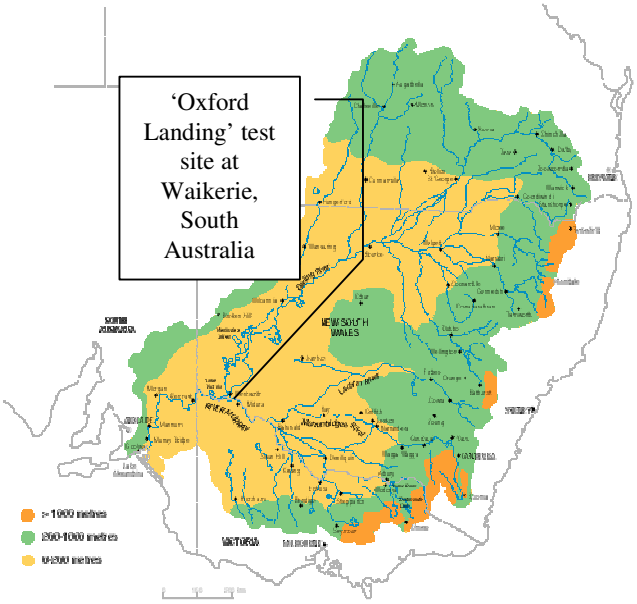

Figure 24 The Murray-Darling Basin in south-eastern Australia covers 14% of the county's total land area and is home to 11% of the Australian population. The Darling (2740km), Murray (2530km) and Murrumbidgee (1690km) are Australia's three longest rivers.

4.1.1 Extending the ADC form to differential and AC excitation measurements

While Chapter 3 has described a very simple ADC for sensors measuring thermistor resistance, semi-conductor temperature sensors and sensor output voltages, the real challenge remained to extend these principles to differential measurements that would normally require an instrumentation amplifier, and sensors requiring AC excitation. In the paper at the end of this chapter, both of these principles are developed and proven in the creation of a salinity sensor used for monitoring salt levels in soil pore water.

Specifically, PRTDs (platinum resistance temperature devices) are commonly operated in bridge circuits where the small differential voltage that represents the full measured temperature range must be extracted in the presence of a high common-mode voltage (equal to half the bridge voltage) using an instrumentation amplifier. Figure 25 shows an alternative method of measuring temperature using a PRTD integrated into a modified form of the charge-balance ADC switched bridge of Figure 23. One additional op-amp is used; this creates a 1-mA sensor offset current through the PRTD to null the

common-mode resistance of 1kΩ, creating a common-mode voltage drop of 1.0V across the PRTD at 0°C.

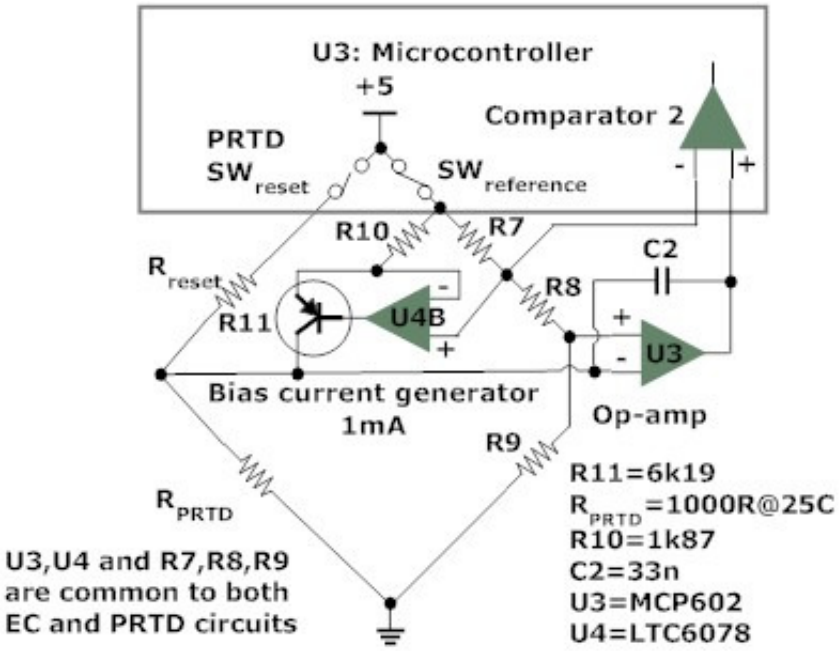

Figure 25 A 16-bit charge-balance ADC for platinum resistance temperature measurement. The bias current generator injects a 1mA current into the PRTD to offset the 1kΩ (0°C) baseline resistance of the PRTD; the ADC only responds to differential resistances above this value in the temperature range 0°C to 50°C

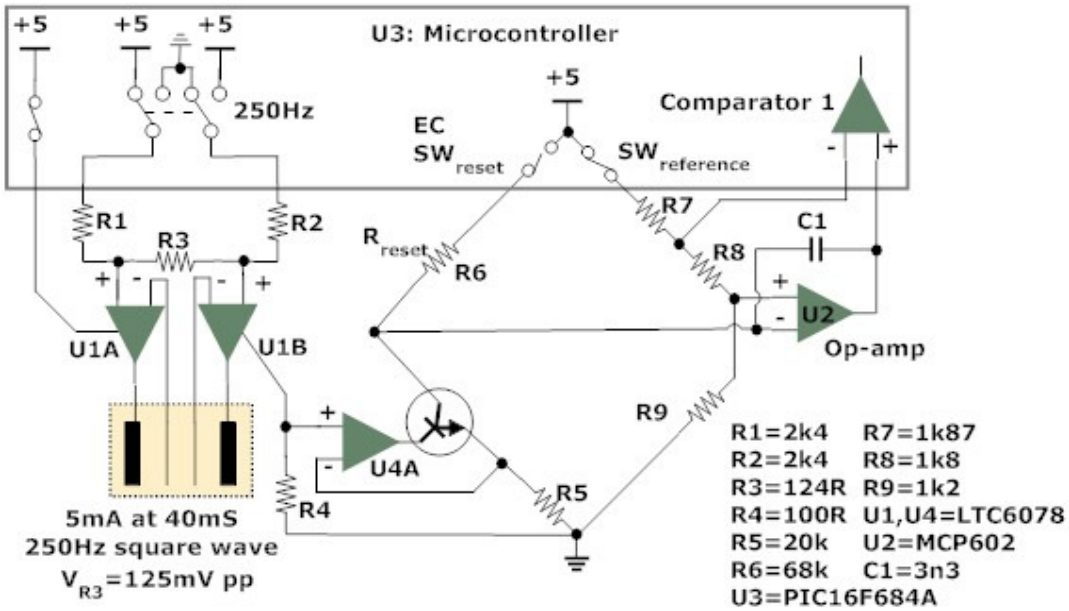

Figure 26 Drive circuitry for a four-electrode platinum electrical conductivity sensor. The EC sensor is driven by a 250 Hz push-pull square-wave via op-amp drivers U1A and U1B whose ground current is approximately equal to the AC current flowing through the conductivity cell. This conductivity current is rectified by the op-amp's output stage and is reflected through a 200:1 current-mirror into the input current side of the 16-bit charge-balance ADC. The LTC6078 micro-power dual op-amp was chosen for its very small quiescent current (an error term in the load current of the conductivity cell).

The electrical conductivity of solutions is used as a measure of their total dissolved salts, and AC excitation is used to prevent polarization of the electrodes. In this design (Figure 26), the current flowing through the electrodes flows in the ground pin of the amplifier IC as a rectified DC signal directly proportional to EC, which is then reflected via the 200:1 current-mirror into the ADC bridge circuit.

A detailed description of these two sensor circuits is given in the paper at the end of this chapter. Matching of the PRTD temperature sensors at a mid-point temperature after an end-point linear calibration routine was ±0.004°C, demonstrating a satisfactory resolution and linearization. The uncertainties in the EC calibration with an eleven-point linearity test using solutions between 0.147 mS/cm to 18 mS/cm gave a sensor matching to within ±1% of full-scale.

Severe drought conditions in the Murray-Darling Basin since 2006 have meant that winter rainfall events that would normally trigger a wetting-front at the test site at Oxford Landing (Figure 27) have been absent since the field installation of the first salinity sensors.

Figure 27 Two wetting-front detectors were installed at Oxford Landing in early 2009, with salinity sensors inserted in early July 2009 in the throats of the WFDs in place of the usual float rods. Continuing drought over the region has meant that insufficient rainfall has fallen to create a wetting front to provide field results in time for thesis publication. The 200-mm depth WFD is installed on the left, and the deeper 400-mm device on the right. Standard vacuum-based soil solute sampling tubes in the bottom left of the photo were installed at these same depths for comparison. The logging system is not shown.

Paper
Skinner, A.J. and Lambert, M.F. (2009). 'An automatic soil salinity sensor based on a wetting front detector.' IEEE Sensors, in submission, July 2009

.

Chapter 5. A log-antilog analog control circuit for constant-power warm-thermistor sensors – Application to plant water status measurement

Skinner, A.J. & Lambert, M.F. (2009). A log-antilog analog control circuit for constant power warm-thermistor sensors application to plant water status measurement.
IEEE Sensors, v. 9 (9), pp. 1049-1057

5.1 Background

A large part of the effort expended in this study has been in the development of a suitable warm-thermistor drive circuit capable of making flow and temperature measurements from a single thermistor. Designs proposed in the literature lacked point-source precision, accuracy and the flexibility to monitor both the ambient and self-heated temperature of the thermistor's environment while operating over widely different power levels. Until such a circuit design existed, no experimental slow flow work could commence. The evolution of this circuit took many years and a description of that process, while lying at the very core of the thesis, can only be presented here in abbreviated form. The paper that arose from this chapter presents the final circuit choice – an analog double-bridge for measuring thermistor temperature during either ambient temperature sensing or constant-power self-heating mode. This circuit allows milliKelvin temperature measurement resolution from a single thermistor while having a non-linear voltage-controlled gain input to allow power to be switched over a range of 1:1000.

That this second paper focuses on irrigated grapevines ties this thesis back to its beginnings; the original pre-thesis research was directed at finding simpler circuits for sap flow measurement as an irrigation-scheduling tool. All three sap flow sensor methods in common use (thermal diffusion, heat pulse and thermal-field distortion, reviewed by

Smith and Allen, 1996) required highly-matched temperature circuits and a controlled constant-power heat pulse. The science of plant physiology has also evolved. Loveys *et al* 2004 (including Skinner) showed that plant water status would be a better measurement to make than transpiration measurements because the genetic coding of the grapevines regulated sap flow in such a way that sap flow became a poor indicator of plant water stress. One needed to wait until sap flow had ceased in the early morning hours to make sensible measurements of the internal water tension within the plant tissue.

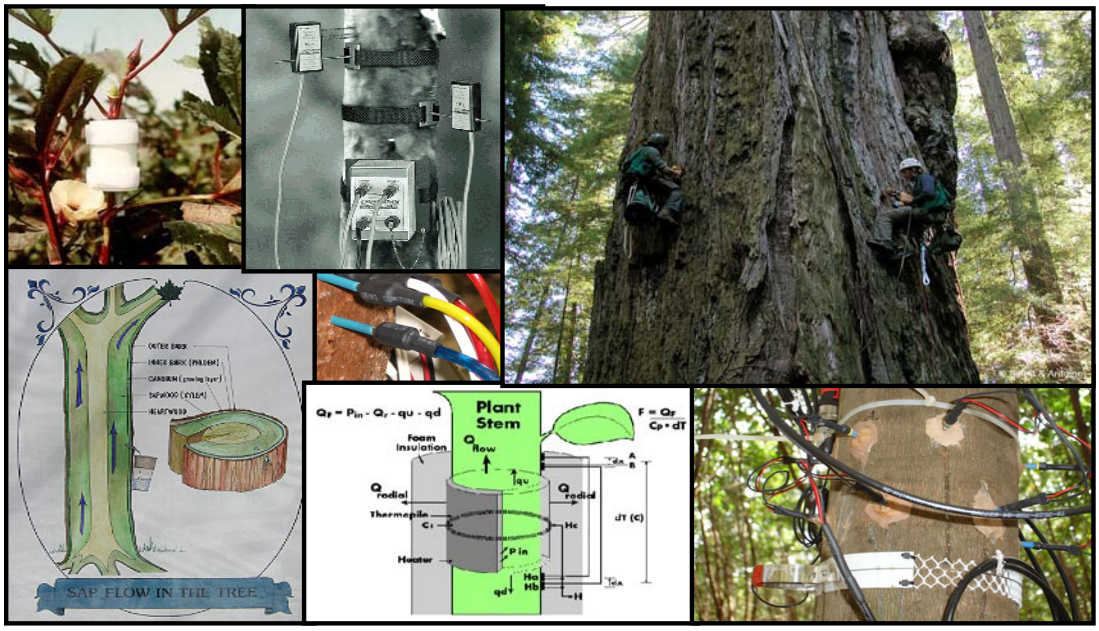

Figure 28 Various commercial sap-flow systems (clockwise from top-left): Dynamax 'heat-balance' sap flow sensor, Greenspan 'heat pulse' sap flow sensors, sap flow measurements in large trees present extra challenges! Granier (thermal diffusion) sap flow sensors, physical model of the 'heat-balance' sap flow sensor, sap flow diagram for a tree, Granier sensors (centre). The white band around the tree in the photo on the bottom right-hand side is a 'dendrometer'; an instrument for the continuous monitoring of tree girth, and an indirect method of monitoring plant water status.

A substantial literature has developed in the past twenty years on the scientific use of sap flow sensors; this is given for reference purposes in Appendix E, courtesy of Professor Brian Loveys of CSIRO Plant Industries and lead author of the aforementioned paper. Figure 28 shows a photographic array of the three basic sensor types in commercial form; thermal diffusion, heat balance and heat pulse sap flow sensors.

Other fascinating techniques exist for measuring plant water status, such as the temperature differential method using infra-red measurement of the plant canopy (cooled by evapotranspiration processes in the leaves) and microphony – the acoustic recording of the formation of embolisms at excessively high tensions within the narrow-capillary sap-conducting xylem vessels. This thesis remains focused on thermal techniques because of

their ability to non-destructively interact with plant tissue provided a satisfactory method can be found of inserting thermistor devices into a plant without causing local damage and tissue wounding or lignification that might ultimately impact upon calibration and measurement repeatability.

The following chapter describes the evolution of ideas behind the development of sensitive thermistor drive circuitry described in the IEEE Sensors paper at the end of the chapter.

5.1.1 Generating constant-power in a thermistor flow meter

This section begins with a restatement of the findings from the literature review that call for a new thermistor drive circuit to tackle very slow flows and thermal diffusion measurements using thermal techniques.

Constant power – rather than constant temperature – excitation in warm-thermistor flow meters has the advantage that internal sensor temperature rather than sensor power dissipation varies with flow. It is then possible to compare two temperatures with a common calibration and common units of measurement. The traditional approach taken in the literature has been to use a second ambient temperature sensing sensor operating at such low power levels that no temperature errors arise from internal self-heating. This ambient temperature thermistor has to be highly matched with the heated thermistor and located outside the influence of its heat field yet near enough to reduce errors due to the inevitable temporal and spatial thermal gradients.

Alternatively, a single thermistor can be heated and cooled to make the same measurement, albeit with a time lag between the two measurements. Such time lags are, fortunately, of little concern in large water bodies many times the mass of the thermistor sensor as the heat capacity and thermal conductivity of water is such that temporal temperature gradients over a few seconds are small.

Constant power excitation can also offer a solution to the long-term problem of bacterial bio-film build up on the sensor in natural water bodies; these films can cause variability in thermal resistance between the heated thermistor and the flow medium. Constant power heat sources merely raise their internal temperature to maintain the same external heat field (albeit from a slightly larger diameter sphere), while constant temperature thermistors suffer from an insulating effect that acts as a temperature divider between the internal thermistor and the external fluid, limiting heat flow.

The constant-power flow meter circuits developed in this thesis aimed for fast response and high temperature resolution (±0.001°C) as the sensor adapts to changes in

both flow-rate and ambient temperature. Power output must be constant under all conditions and switchable over a wide range of about 1:1000 in order to allow both ambient temperature and self-heated temperature measurement from a single point source.

In the course of this research, a procession of circuits was developed to implement a constant power flow meter. Each circuit had a number of advantages and disadvantages in comparison to the previous model but in general represented a positive evolutionary step. The key criteria for evaluating each circuit were simplicity, low-cost, accuracy, precision and freedom from the effects of electrical and thermal noise. Four preliminary thermistor drive-circuit configurations were investigated and discarded before selection of the fifth and final circuit published in the IEEE Sensors journal:-

1. In the first, a thermi-linear pair uses bonded-bead thermistors as separate sensor and heater elements, allowing continuous fast-response heat output from a point source thermistor heater. Mismatching of thermistor materials creates temperature-dependent errors.
2. In the second circuit, a single bead-in-glass thermistor is used as both sensor and heater, with time-division multiplexing between sensor and heater modes made possible by the use of a sample-and-hold network to capture the thermistor's internal temperature. This circuit eliminates mismatch errors, but thermal-droop and response-time errors are introduced.
3. In the third circuit, the thermistor is heated continuously while the thermistor resistance is sensed by zero-power AC excitation that can be captured through a series blocking capacitor and synchronously demodulated by a lock-in amplifier. This circuit satisfies design criteria of steady-state output and no mismatch but is expensive to implement and suffers from a degraded signal to noise ratio.
4. The fourth circuit uses variable bridge excitation to hold the thermistor in a constant power state and an inverse square root circuit transfer function to obtain it. This fourth circuit uses an in-built high-resolution sigma-delta analog-to-digital to obtain the operating temperature of the heated thermistor. A variation on this circuit replaces the expensive analog inverse square-root circuit with a digital algorithm in the sensor microcontroller. This circuit suffers, however, from a very slow time-constant in the order of 5-10 seconds.
5. The final (published) circuit is a double-bridge log-antilog analog circuit for single thermistor drive capable of high speed, 1000:1 power level switching, non-linear

control input and in-circuit thermistor temperature monitoring to better than ±0.001°C.

Some common principles emerged in the designs of these constant power circuits. Firstly the thermistor dissipating this constant power has the independent variable in a circuit having the input property of 'resistance'. This thermistor's resistance dissipates heat when the voltage across it results in a current flow through it. The resistance changes due to environmental factors such as the external temperature of the fluid, the temperature rise due to self-heating, the insulating effects of the thermistor bead encapsulant, thermal conductivity and heat capacity of surrounding materials and the convective cooling effect of flow over the sensor. The value of the excitation voltage or current to be applied is the output of a feedback circuit whose input measures the resistance of the thermistor to be heated such that the input resistance must be sensed in the presence of the excitation signal. Furthermore, the relationship between the sensor excitation signal and the heater excitation signal must be one of two forms of square-root function because the relationship between resistance and power is always a square term of the excitation current or voltage

$$P = I^2 R = \frac{V^2}{R} \tag{4.1}$$

Finally – as will become obvious in the examples below – if the sensor excitation is a voltage then the sensor heater excitation must be a current, and vice versa.

5.1.2 The dual element heat source: thermilinear thermistor devices

An obvious technique for knowing the temperature of the heated thermistor inside its encapsulant is to bond a second thermistor heat sensor directly to it and to measure the heated thermistor's temperature directly. For this to work, the sensor and heated thermistors have to be highly coupled thermally yet electrically isolated. Such dual element thermistors are available (e.g. from YSI Incorporated in Yellow Springs Ohio USA and shown schematically in Figure 29) for a use in linear-response thermistor networks. They are known as thermilinear networks. Typically these thermistors have two hemispherical beads bonded together with a common central conductor and an overall diameter of about 2mm inside an epoxy encapsulant.

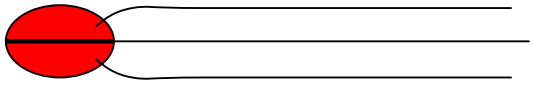

Figure 29 A thermilinear thermistor, consisting of a high-resistance thermistor thermally and electrically bonded to a low-resistance thermistor.

Two common thermilinear thermistors have a 1k and a 10k pair and a 6k and a 30k pair as shown in Table 1: -

Table 1 Resistance values of two YSI thermilinear components

Thermilinear Component	Resistance of T_1 @ 25°C	Resistance of T_2 @ 25°C
YSI 44018	6,000Ω	30,000Ω
YSI 44019A	1,000Ω	10,000Ω

The lower resistance thermistor can carry a higher current, and therefore dissipate a higher power level, in a flow sensor powered by a 12-volt battery-powered field system. For example, a 1k-10k thermilinear pair with 10mA flowing through the 1k thermistor will dissipate 100mW, while a 100μA sensing current through the 10k thermistor will dissipate only 100μW, or 1/1000th of the power in the heater. Thermistors in a still-water environment typically exhibit a linear temperature rise of 1°C per 10mW of power dissipated so that temperature rise in these two thermistors will be 10°C and 0.01°C respectively. That is, the self-heating due to the current through the sensing thermistor is negligible compared to that occurring within the heated thermistor.

In the block diagram of Figure 30 the ambient sensing thermistor is excited by a 100μA constant-current source I_{ref}. The voltage drop V_t generated across this thermistor resistance R_{sense} is buffered and applied to the ground referred input resistor R_{in} of the square root circuit, generating the input current I_{in}. The output of the square-root circuit is also a current, I_{out}. This is applied to the transimpedance amplifier to generate a heating voltage V_{heat} applied across the heater thermistor R_{heat}. The sense signal is a current, while the excitation signal is a voltage. The transimpedance gain resistor R_{gain} sets the power dissipation level.

$$V_t = I_{ref} \times R_{sense} \tag{4.2}$$

$$I_{in} = \frac{V_t}{R_{in}} = \frac{I_{ref} \times R_{sense}}{R_{in}} \tag{4.3}$$

$$I_{out} = k \times \sqrt{I_{in}} = m \times \sqrt{R_{sense}} \tag{4.4}$$

$$V_{heat} = I_{out} \times R_{gain} = n \times \sqrt{R_{sense}} \tag{4.5}$$

$$P_{heat} = \frac{{V_{heat}}^2}{R_{heat}} = q \times \frac{\left(\sqrt{R_{sense}}\right)^2}{R_{heat}} = q \times \frac{R_{sense}}{R_{heat}} \tag{4.6}$$

where I_{ref}, R_{in}, R_{gain}, k, m, n and q are constants.

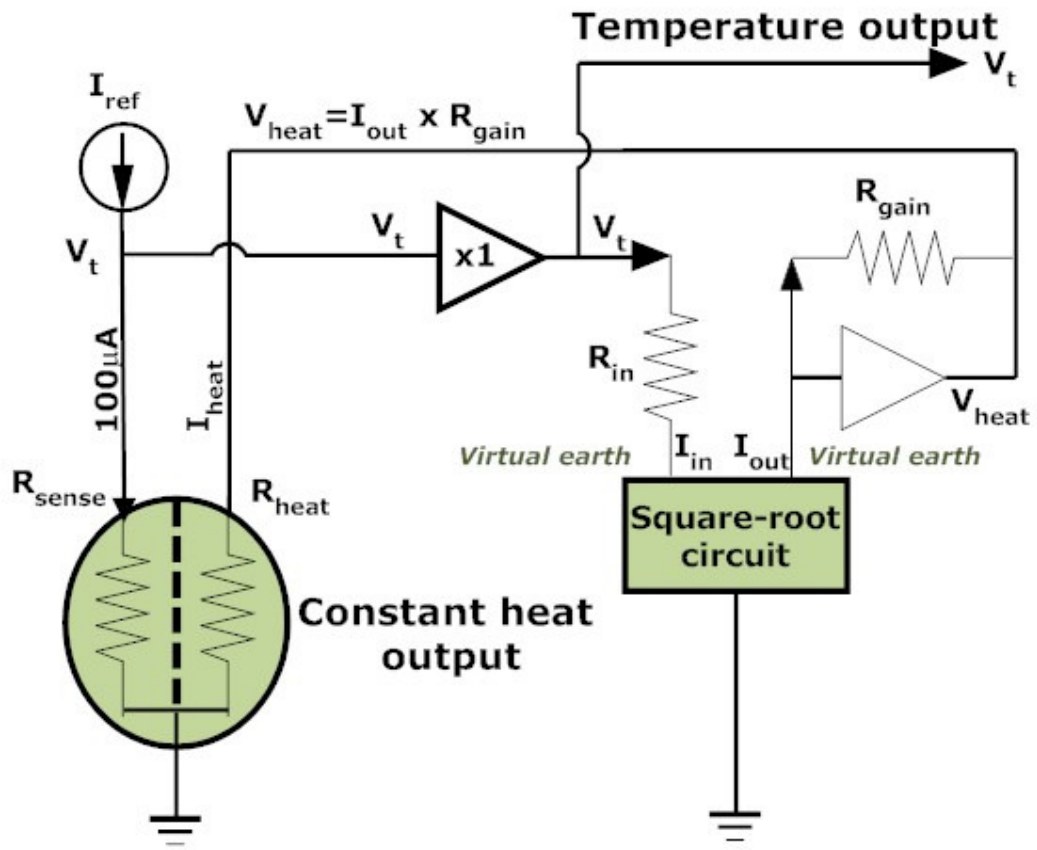

Figure 30 Constant power flow meter using a thermilinear element as a combined sense and heater

The power P_{heat} dissipated is a ratio equal to R_{sense}/R_{heat} which is roughly constant, inherent in the manufacture of the thermilinear device and largely independent of temperature. Constant q is the ratio of fixed resistors in the circuit and is therefore also a constant.

While conceptually simple, there are a number of problems with this circuit architecture. Firstly, the lowest value thermistor in the thermilinear pair must be able to dissipate useful amounts of heat at the low voltages available to sensors running on battery power. In the better of the two pairs mentioned, it is the 1k thermistor that is capable of dissipating the most power (compared to the 6kΩ device). The resistance of the 1kΩ thermistor at the lowest operating temperature determines the maximum amount of power that can be dissipated. For example, at 5°C the heater resistance is 2192Ω. Allowing for low battery conditions of 11.5V in a 12V battery-powered instrument and the likelihood that the transimpedance amplifier can only drive to within 1.5V of the positive supply, then heater voltage is set at this temperature via R_{gain} to be a maximum of

10 volts. This is equivalent to a power dissipation of 45.6mW and an over-temperature operation of typically 5.7°C at a heat dissipation factor for the thermistor of 8mW/°C. This is a useful heat output for a warm thermistor flow meter, but one can see immediately why these devices are so sensitive to ambient temperature variations and why high resolution temperature measurements need to be made to a reference fluid temperature. Hot wire anemometers, by contrast, run at over ten times these over-heat levels (typically 70°C in water).

The more significant problem is the assumption that these thermistors maintain a constant resistance ratio over the ambient operating temperature range of water from 5°C to 45°C. Some inherent mismatch exists in their curves because 1kΩ and 10kΩ thermistors are manufactured from different mixes of nickel manganese and iron oxides. The real ratio of $\boldsymbol{R_{sense}/R_{heat}}$ for YSI thermistors, calculated by using the manufacturer's published $\boldsymbol{a}$, $\boldsymbol{b}$ and $\boldsymbol{c}$ constants in the Steinhart-Hart equation for a 1kΩ-10kΩ thermilinear composite thermistor, ranges from 0.085 at 5°C to 0.115 at 45°C. Power varies from 39mW to 52 mW over the same temperature range, giving a systematic linear gain error between temperature and power output of about 319μW/°C.

One of the advantages of this configuration is that the sense temperature is readily available as a large single-ended voltage at the output of the buffer amplifier in Figure 30. This temperature could be used to determine the true power output based on the linear relationship between power output and temperature. While this is mathematically possible, the fact remains that the heat field is not constant if the heat output is not constant, and this introduces empirical corrections into the calibration equation.

The final problem is that these thermilinear pairs are most often sealed with an epoxy coating rather than a glass coating and are therefore not sufficiently hermetically sealed for use as a fluid flow sensor, although they may be adequately protected for thermal diffusion measurements.

In summary, this might be a workable solution for building a continuous-sensing constant point heat source, but the drawbacks mentioned pushed the investigation onwards towards some single thermistor solution whose attributes could be known exactly and corrected for.

5.1.3 The switched heat source

The problem of mismatch between the heated and sensing thermistors in the thermilinear pair can be overcome by using a single thermistor as both heater and sensor. This requires some method of sensing and capturing the thermistor's resistance using a sense current, and then calculating and impressing the appropriate drive voltage across it to heat it. The obvious choice is to multiplex the sensing and power currents onto the thermistor, with a sample-and-hold circuit to capture the (warm) resistance of the thermistor and to apply it to the square root drive circuit. This is illustrated in the block diagram in Figure 31. The heating voltage V_{heat} is switched off momentarily and a 100µA sense current is switched though the thermistor. Provided this is done rapidly enough, the temperature droop in the heated thermistor will be small and the sense voltage will represent the heated temperature of the thermistor in operation. This sense voltage is buffered and stored on a sample-and-hold network driven in synchronism with the chopper frequency, as shown diagrammatically in Figure 31.

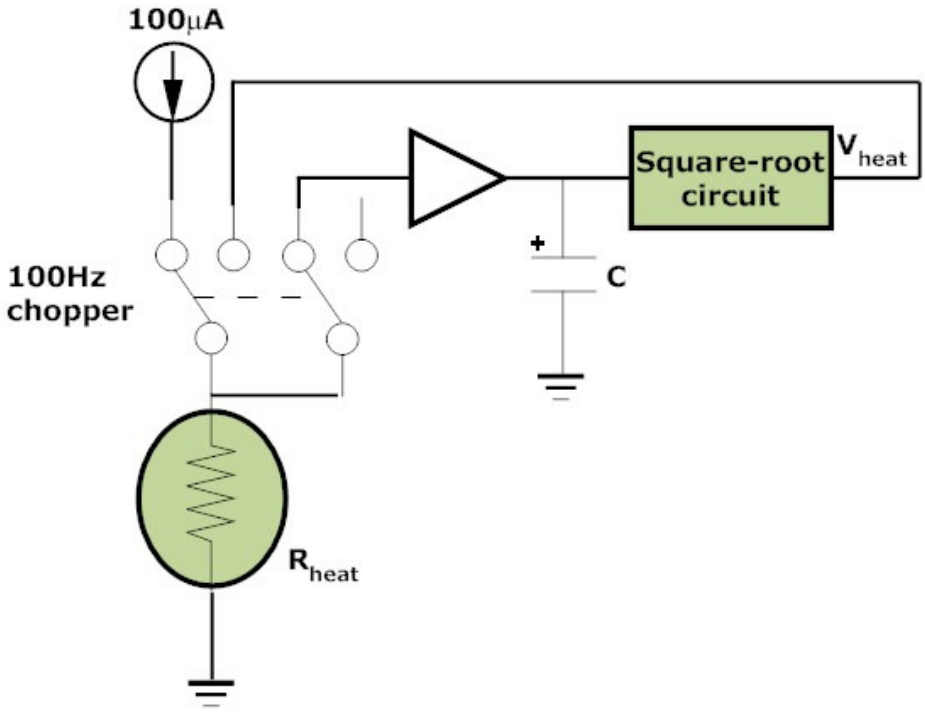

Figure 31 Block diagram of chopper-based single thermistor constant power heat source (power drive not shown)

The sense voltage on the hold capacitor is presented with minimal droop to the square-root circuit. The power stage at the output of the square-root circuit applies the heating voltage across the thermistor via the single-pole dual-position multiplexer switch.

Over time, this circuit tracks changes in temperature and flow. The heater's temperature is available after the hold-capacitor's buffer stage (not shown in Figure 31 for simplicity).

The advantage of the switched heat source has already been made in comparison with the dual-element thermistor; there is no mismatch between thermistors because a single thermistor – no matter what its transfer function – is self-referencing. This allows use of a hermetically sealed bead-in-glass thermistor capable of continuous submersion – this is an essential criterion to be met in a flow meter application.

There are, however, two real and intractable disadvantages with this method of obtaining constant power from a single thermistor. Firstly heating power is only applied for half the time if the chopper frequency has an even mark-space ratio as no self-heating occurs during the 'sense' half of the cycle. This can be ameliorated somewhat by increasing the heating cycle at the expense of the temperature sensing cycle. The limitation to this technique is that current sources are inherently high-impedance devices and this slows their response in the presence of stray capacitance associated with the thermistor's cabling and circuitry. Shorter sensing cycles also impose the need for more drive capability and higher slew-rates on the sample-and-hold driver, which has practical limitations as offset voltages tend to worsen once the designer moves away from precision amplifiers with their slow slew rates of 1μV/s and limited output current capabilities.

Three forms of 'droop' come into operation with this circuit, limiting accuracy. The first of these is 'thermal droop' in the thermistor; it cools during sense mode, and it is at its coolest value when captured by the sample-and-hold network to be fed into the square-root driver. 'Electronic droop' also occurs in the sample-and-hold circuit. The third form is even subtler, and could be termed 'resistance droop'. This circuit is essentially applying a constant voltage to the thermistor for half the chopper cycle. Current flow causes self-heating to occur, thermistor resistance falls as temperature increases, current increases further, power dissipation increases again, temperature increases further and so forth. This 'resistance droop' with constant-voltage drive adds some unquantifiable amount of error to the signal.

Finally, ripple on the heat source must ultimately impact on the measurement or the quality of the heat field. These concerns led to a search for a circuit where the heat source from a single bead-in-glass thermistor could be sensed at the same time as it was heated – without ripple.

5.1.4 The dual current heat source

The third technique - the dual current heat source - solves both the problem of ripple on the heat source and the half-power problem by making a measurement of the internal resistance of the thermistor whilst continuing to heat it. In the configuration of Figure 32, an AC non-heating sense current is impressed upon the heating current directly to determine the thermistor resistance. This AC signal is recovered using synchronous rectification techniques and its magnitude will be equal to the voltage drop across the thermistor excited by the 100μA sense current alone.

This type of circuit is often called a 'lock-in' amplifier, and is distinguished by its very high rejection of both the common-mode voltage caused by the heater current through the thermistor (blocked by the capacitor ***C***) and any non-coherent noise components at frequencies other than the chopper frequency. Thus one is able to measure a single thermistor's internal resistance continuously while heating it, at the same time eliminating heat ripple. The thermistor can be calibrated in the normal way by simply disconnecting the heating current drive to the circuit.

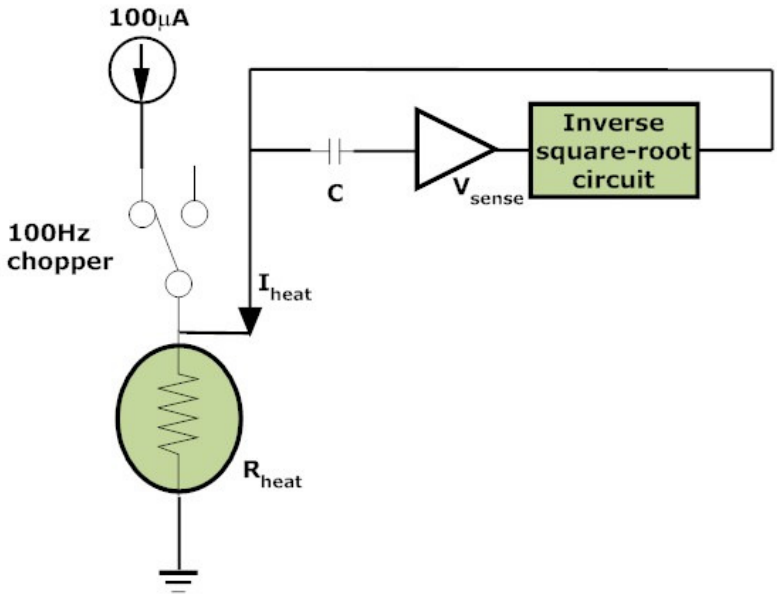

Figure 32 Dual-current source constant-power thermistor heater. Details of the unity-gain buffer and synchronous demodulator are not shown.

The change from voltage drive to current drive in the heater circuit changes the transfer function of this flow meter to an inverse square root function from a direct square root function. The equations below show that power is constant and independent of temperature, because the constant ***q*** is the ratio of fixed resistors: -

$$V_{sense} = I_{ref} \times R_{heat} \tag{4.7}$$

$$I_{in} = \frac{V_{sense}}{R_{in}} = \frac{I_{ref} \times R_{heat}}{R_{in}} \tag{4.8}$$

$$I_{out} = \frac{k}{\sqrt{I_{in}}} = \frac{m}{\sqrt{R_{heat}}} \tag{4.9}$$

$$P_{heat} = I_{out}{}^{2} \times R_{heat} = q \times \frac{R_{heat}}{\sqrt{R_{heat}}^{2}} = q \tag{4.10}$$

While this circuit has achieved the technical specifications it is nevertheless expensive to build in the modulator/demodulator circuit because of the relatively high price of the LTC1043 switched capacitor building block and the 100µA constant current source, $\boldsymbol{I_{ref}}$. It was built and partially tested, but suffered from poor signal-to-noise ratios due to the low level of the demodulated signal that needs to be measured with such precision. It is a circuit worthy of more effort, but only on the basis that the improved designs are unsuccessful in practice. It does have the advantage of allowing alternate measurement of both ambient and self-heating temperatures.

5.1.5 A switched bridge constant-power thermistor flow meter

This fourth circuit is a switched bridge with a digital output, shown in Figure 33, and is a natural derivation of the integrated thermistor/ADC developed in Chapter 3. One difference is that the original fixed ADC reference voltages have to be variable and dependent upon the bridge excitation voltage. Because the bridge voltage and reset output from the ADC microcontroller are now at different levels (previously both were at 5V) reset current to the charge balance circuitry is now switched via a MOSFET through the reset resistor from the bridge voltage supply.

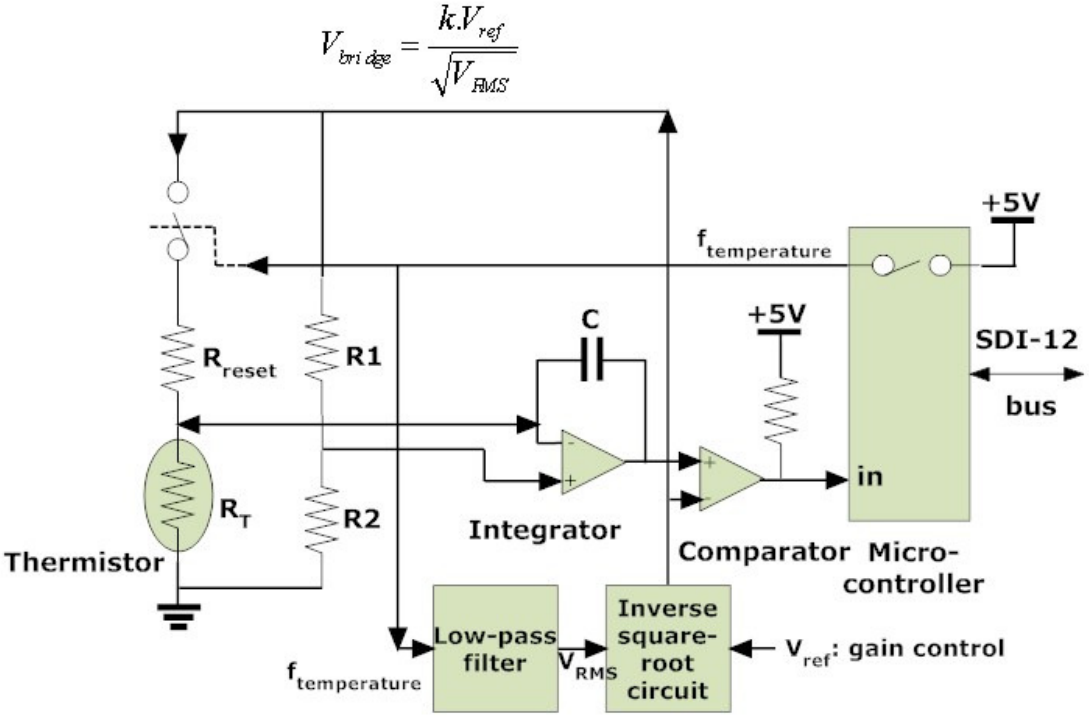

Figure 33 Block diagram of the constant power thermistor bridge with inherent temperature measurement. The detail of the inverse square-root circuit is shown in Figure 34

This circuit configuration eliminates the need for a separate 100µA temperature sensor reference current. As it is an extension of the temperature measurement technology developed earlier in the thesis, it is able to make a direct digital measurement of the heated thermistor's temperature. Heating of the single thermistor is continuous.

The bridge voltage of the 'switched arm' bridge circuit of Figure 33 is derived directly from the ADC's own output frequency via a low-pass filter that generates a voltage V_{RMS} that is fed into the external 'inverting square-root' circuit in the feedback loop. It is this feedback mechanism that maintains constant power dissipation in the thermistor under changing flow and ambient temperature conditions. The gain of the system, and hence the bridge voltage and power dissipation in the thermistor, is set by a voltage input, V_{ref}. Power must be switched over a range of 1:1000 between ambient and self-heating modes of the thermistor.

There are number of disadvantages to this circuit, despite its apparent simplicity.

Firstly, the integrator's output must deliver both the sense current in low-power mode and (with more difficulty) the self-heating current in high-power mode. This current has to flow through the integrator capacitor at the ADC frequency. In reset mode, the inverse square-root circuit that drives the bridge voltage must also supply sufficient current quickly enough to discharge the integration capacitor through the reset resistor

R_{reset} while also maintaining heating current through the thermistor. By definition then, the integration capacitor must itself be large enough to handle these current flows, where $I_C = C \cdot dV/dt$. As such large value capacitors are impractical, current mirrors (not shown) need to be inserted into a practical bridge circuit to enable satisfactory operation with smaller standard-value capacitors.

Secondly, the bridge has an inherently slow response because of the first-order roll-off of the low pass filter and the long integration time needed by this form of SVFC to achieve a satisfactory measurement resolution.

One final disadvantage of the circuit is that the loop gain, and therefore the power output, is linearly proportional to V_{ref}, which limits the dynamic range of the thermistor power levels. A non-linear square-law relationship would be preferable between the voltage-controlled gain input V_{ref} and the power dissipation rate P.

The operation of this constant power bridge is not intuitively obvious, but can be shown (below) to be mathematically correct. The integrator's set-point has to be a variable related to the bridge voltage as it effectively sets the voltage drop across the thermistor and so determines its power dissipation rate at any given temperature or flow rate. That is, the thermistor drive voltage is ratiometrically related to the bridge voltage via the voltage divider formed by the resistors in the right-hand arm of the bridge.

By keeping the comparator threshold related to the integrator set-point by a fixed ratio rather than a fixed value, the comparator trigger point tracks the changing bias conditions in the bridge. The comparator threshold must be greater than the integrator's set-point to allow positive ramping of the integrator output; a convenient voltage for the comparator's threshold is therefore the bridge voltage itself.

The integration cycle

During the integration cycle, the integrator output of Figure 33 ramps positive in a linear fashion to supply current i_C through the capacitor to the thermistor at a rate which forces V_T, the summing junction (equal to the voltage across the thermistor to ground) to be: -

$$V_T = V_{bridge} \cdot \frac{R_2}{R_1 + R_2} \tag{4.11}$$

Thus the thermistor is driven by a voltage that is ratiometrically dependent upon the bridge voltage V_{bridge}, and i_C is proportional to the thermistor resistance R_T

$$-i_C = \frac{R_2 \times V_{bridge}}{(R_1 + R_2) \times R_T} \tag{4.12}$$

The current flow direction is arbitrarily chosen to be positive (towards the integrator output) during the reset period and is therefore negative during the integration period when it is flowing from the integrator output back through the thermistor to ground.

The total integration charge $\boldsymbol{Q_I}$ is the charge delivered to the integrator capacitor during all the integration cycles during the gating period $\boldsymbol{T_G}$, equal to 65536 clock cycles. The number ***counts*** is the number of reset pulses generated during the gating period $\boldsymbol{T_G}$, so that the period of integration is

$$t_I = \frac{65536 - counts}{65536} \cdot T_G \tag{4.13}$$

The 15-bit number ***counts*** is incremented in the microprocessor each time a reset pulse is generated and it is this number which is used to calculate the temperature of the self-heated thermistor after the gating period measurement time $\boldsymbol{T_G}$ is complete. Each reset pulse is on for one full clock cycle, and then must be off for at least another full clock cycle while the comparator tests the state of the integrator output. Therefore only 32768 reset pulses are possible in 65536 clock cycles, which is why the measurement resolution is limited to 15 bits for 2^{16} clock cycles.

The period of integration is

$$t_I = \frac{65536 - counts}{65536} \cdot T_G \tag{4.14}$$

The total (negative) charge $\boldsymbol{Q_I}$ that is added to the integration capacitor during the gating period $\boldsymbol{T_G}$ is therefore

$$-Q_I = t_I \cdot i_C \tag{4.15}$$

$$-Q_I = T_G \times \frac{(65536 - counts)}{65536} \times \frac{R_2 \times V_{bridge}}{(R_1 + R_2) \times R_T} \tag{4.16}$$

The total accumulated charge during integration is negative because of the reverse current flow convention.

The reset cycle

During the reset cycle, the current $\boldsymbol{I_R}$ flowing into the integrator summing junction (assuming that the switch resistance is zero) from the reset pin is

$$i_R = \frac{V_{bridge} \cdot \dfrac{R1}{R1 + R2}}{R_R} \tag{4.17}$$

and must be equal to the sum of the currents leaving the summing junction, namely

- i_T through the thermistor to ground, and
- i_C through the capacitor to the integrator's output (which sinks this current to ground)

The integrator's output is ramping negative from an undefined voltage level $\geq V_{bridge} \cdot \frac{R2}{(R1+R2)}$ towards ground potential. Note that according to the convention above, $\boldsymbol{i_C}$ is positive. Therefore the current flowing through the integration capacitor $\boldsymbol{i_C}$ during the reset cycle is the difference between the reset current $\boldsymbol{i_R}$ flowing into the junction from the bridge excitation voltage through the reset resistor and the current $\boldsymbol{i_T}$ flowing to ground through the thermistor: -

$$i_C = i_R - i_T \tag{4.18}$$

where

$$i_T = \frac{\left(V_{bridge} \cdot \frac{R_2}{R_1 + R_2}\right)}{R_T} \tag{4.19}$$

The period over which reset pulses are issued during the gating period $\boldsymbol{T_G}$ is

$$t_R = \frac{counts}{65536} \cdot T_G \tag{4.20}$$

and therefore the charge $\boldsymbol{Q_R}$ stripped off the integrator capacitor during the gating period $\boldsymbol{T_G}$ is: -

$$Q_R = t_R \cdot i_C \tag{4.21}$$

$$Q_R = T_G \times \frac{counts}{65536} \times \frac{V_{bridge}}{(R_1 + R_2)} \times (\frac{R_1}{R_R} - \frac{R_2}{R_T}) \tag{4.22}$$

The ADC maintains charge balance on the capacitor such that: -

$$Q_R + Q_I = 0 \tag{4.23}$$

Substituting terms in the equation $Q_R = -Q_I$

$$T_G \times \frac{counts}{65536} \times \frac{V_{bridge}}{(R_1 + R_2)} \times (\frac{R_1}{R_R} - \frac{R_2}{R_T}) = T_G \times \frac{(65536 - counts)}{65536} \times \frac{R_2 \times V_{bridge}}{(R_1 + R_2) \times R_T} \tag{4.25}$$

$$counts \times (\frac{R_1}{R_R} - \frac{R_2}{R_T}) = (65536 - counts) \times \frac{R_2}{R_T} \tag{4.26}$$

$$\frac{R_T}{R_2} \times (\frac{R_1}{R_R} - \frac{R_2}{R_T}) = \frac{(65536 - counts)}{counts} \tag{4.27}$$

$$\frac{R_T}{R_2} \times \frac{R_1}{R_R} = \frac{65536}{counts} \tag{4.28}$$

$$R_T = \frac{65536}{counts} \times \frac{R_2}{R_1} \times R_R \tag{4.29}$$

Therefore, the thermistor resistance $\boldsymbol{R_T}$ to be measured is quite simply related to the known fixed reset resistance $\boldsymbol{R_R}$ via the bridge resistors and the output ***count***. The output can be seen to be independent of the bridge voltage $\boldsymbol{V_{bridge}}$, the integrator capacitor value $\boldsymbol{C}$, the clock frequency $\boldsymbol{f_C}$ and the gating period $\boldsymbol{T_G}$. The value of $\boldsymbol{R_R}$ is set to the resistance value $\boldsymbol{R_{Tmax}}$ of the thermistor at the warmest temperature; cooler temperatures increase the thermistor resistance and ***counts*** falls from a maximum of 32768.

Thermistor power dissipation

The aim of the bridge drive circuitry is to maintain a constant heat flow out of the thermistor despite changes in fluid temperature, flow-rate and dissipation rate. That is, thermistor power dissipation $\boldsymbol{P_T}$ must be constant.

The bridge voltage $\boldsymbol{V_{bridge}}$ is derived from the RMS (root-mean-square) value of the bridge output frequency (via an active two-pole Butterworth filter) and the inverting square-root circuit of Figure 34.

The peak voltage V_S of the bridge output frequency is +5V, then

$$V_{RMS} = \frac{counts}{65536} \times V_S \times G_F \tag{4.30}$$

The output voltage $\boldsymbol{V_{RMS}}$ from the active filter drives the inverting square-root circuit whose voltage-controlled gain $\boldsymbol{V_{ref}}$ is a multiplier in the transfer equation such that the bridge voltage $\boldsymbol{V_{bridge}}$ is

$$V_{bridge} = \frac{\sqrt{10}}{10} \times V_{ref} \times \frac{1}{\sqrt{V_{RMS}}} \tag{4.31}$$

Substituting for V_{RMS} gives

$$V_{bridge} = \frac{\sqrt{10}}{10} \times V_{ref} \times \frac{1}{\sqrt{\frac{counts}{65536} \times V_S \times G_F}} \tag{4.32}$$

Returning now to the solution of the thermistor power dissipation $P_T = \frac{{V_T}^2}{R_T}$ where

$$V_T = \frac{R_2}{(R_1 + R_2)} \times V_{bridge} \tag{4.33}$$

$$P_T = \frac{(\frac{R_2}{(R_1 + R_2)} \times V_{bridge})^2}{R_T} \tag{4.34}$$

where the formula for R_T based on bridge resistances and counts is

$$R_T = \frac{65536}{counts} \times \frac{R_2}{R_1} \times R_R$$

$$P_T = \frac{(\frac{R_2}{(R_1 + R_2)} \times \frac{\sqrt{10}}{10} \times V_{ref} \times \frac{1}{\sqrt{\frac{counts}{65536} \times V_S \times G_F}})^2}{\frac{65536}{counts} \times \frac{R_2}{R_1} \times R_R} \tag{4.35}$$

$$P_T = \frac{\frac{R_2^{\,2}}{(R_1 + R_2)^2} \times \frac{1}{10} \times \frac{1}{V_S \times G_F}}{\frac{R_2}{R_1} \times R_R} \times V_{ref}^{\,2} \tag{4.36}$$

All the terms on the right-hand side of Eq. 4.36 except $\boldsymbol{V_{ref}}$ are constant, although sensitive to resistance drift, temperature coefficients of resistance, and changes in the regulated microcontroller supply voltage V_S. Therefore thermistor power dissipation is kept constant by the circuit, despite changes in ambient fluid temperature and fluid flow, for any fixed value of the non-linear gain control voltage $\boldsymbol{V_{ref}^2}$.

5.1.6 An inverse square root circuit using analog hardware multipliers

The inverse square-root circuit of Figure 33 can be implemented using analog multipliers as shown in Figure 34.

The inverse square-root circuit consists of two op-amps ***A1*** and ***A2*** and two four-quadrant analog multipliers ***M1*** and ***M2***. Each multiplier has two inputs ***X*** and ***Y*** and an output voltage equal to ***(X.Y)/10***. Multiplier ***M1*** is connected as a 'squarer' inside the negative feedback loop of the amplifier ***A1*** whose feedback resistance ***R*** is equal to the input resistance ***R***, forcing the voltage at the output of multiplier ***M1*** to be equal to the input voltage $\boldsymbol{V_{RMS}}$. The lower amplifier ***A2*** has multiplier ***M2*** in its negative feedback loop, and is connected as a 'divider' such that the amplifier output servos multiplier ***M2*** to be equal to the gain control input $\boldsymbol{V_{ref}}$. The output of the lower amplifier is the bridge voltage $\boldsymbol{V_{bridge}}$ such that

$$V_{bridge} = \frac{\sqrt{10}}{10} \cdot \frac{V_{ref}}{\sqrt{V_{RMS}}} \tag{4.37}$$

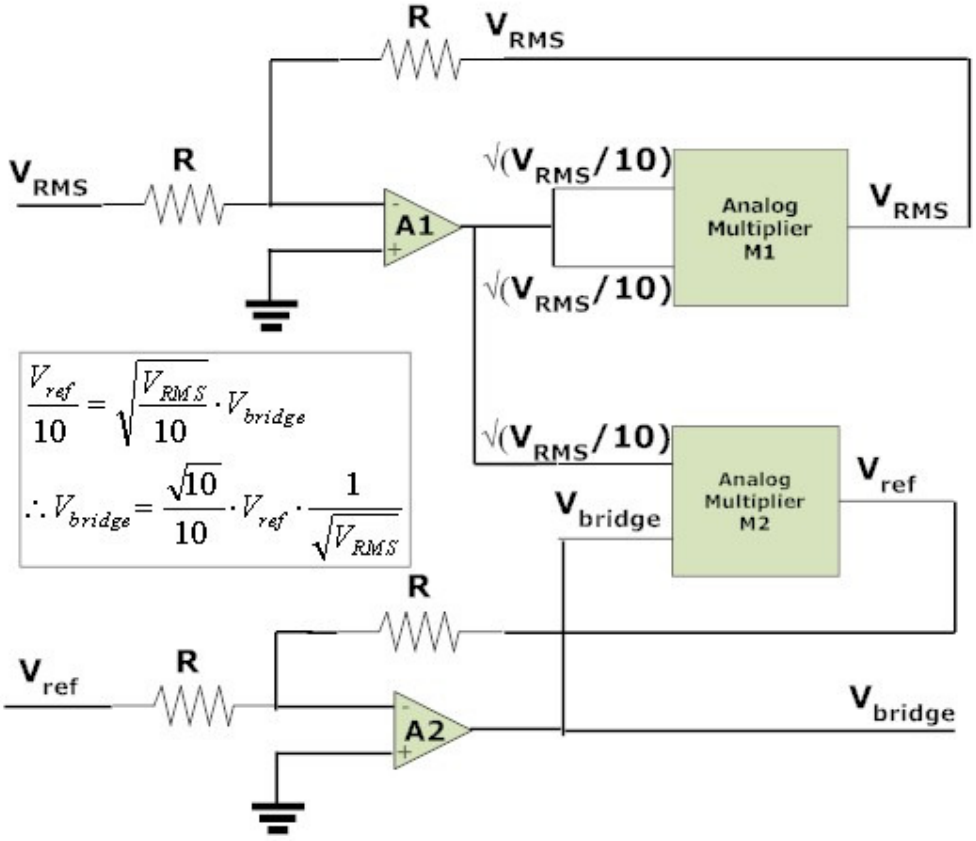

$$\frac{V_{ref}}{10} = \sqrt{\frac{V_{RMS}}{10}} \cdot V_{bridge}$$

$$\therefore V_{bridge} = \frac{\sqrt{10}}{10} \cdot V_{ref} \cdot \frac{1}{\sqrt{V_{RMS}}}$$

Figure 34 Inverse square-root circuit using analog four-quadrant multipliers

Therefore the bridge voltage of Figure 34 increases with the reference voltage V_{ref} and is inversely proportional to the square root of the filter DC output voltage V_{RMS}.

5.1.7 Solving the inverse square-root function using digital multipliers

The preceding methods were developed for use with very simple microcontrollers having limited functionality. A faster method was developed for more powerful microcontrollers having 16-bit hardware multipliers built in. This technique is an adaptation of the Newton-Raphson Method for finding square roots - a method particularly useful in that it has a fast convergence rate. In this method, the square root of the number N is obtained as an approximate solution of

$$f(Y) = Y^2 - N = 0 \tag{4.38}$$

An initial value of half the 16-bit full-scale range is used for Y (i.e. 1000 0000 0000 0000) and the hardware multiplier rapidly solves $Y.Y$ to give Y^2. If $Y^2 < N$ then the value Y is increased by turning on the next most significant bit to create Y (1100 0000 0000 0000) and the process of squaring Y is repeated. If the result of $Y^2 > N$ then the

value ***Y*** is decreased by turning off the next most significant bit. After a maximum of 16 successive approximations, a true value for the square root of ***N*** is the final value of ***Y***.

The ***inverse*** square-root of the number ***N*** is obtained as an approximate solution of

$$f(Y) = Y \times N^2 = 1 \text{ as } \frac{1}{N^2} \times N^2 = 1 \tag{4.39}$$

In programming terms, it is a simple matter to use the hardware multiplier to square ***N*** and multiply it by an approximate value ***Y*** until the result is equal to 1. Using a 16-bit x 16-bit hardware multiplier in modern microcontrollers allows rapid calculation of the inverse square root of an incoming count.

5.1.8 A log-antilog inverse square-root circuit

The resistance $\boldsymbol{R_T}$ of a heated thermistor dissipating a constant amount of heat ***P*** into a flow stream or thermally conductive medium will respond simultaneously to changes in ambient temperature $\boldsymbol{T_A}$ and to changes in the surrounding fluid properties or velocity**.** So while the product of the thermistor's voltage and current (the power dissipated) is fixed in a constant power heater circuit, the ratio of voltage to current (the resistance) is always varying, and must be continuously extracted to drive the feedback control loop. If the traditional ambient temperature reference thermistors are not used to correct for ambient temperature changes, one is forced to switch the control circuit between zero power and full power to obtain first the ambient and then the heated temperatures.

Work on the inverse square root circuit for the switched bridge circuit of sections 5.1.5 and 5.1.6 suggested that the response time was too slow. A simpler solution for solving the inverse square-root transfer function was sought based on known squarer and square-root circuits using log-antilog principles known for their wide dynamic range and the inherently infinite resolution of analog circuits. This circuit is the subject of the paper at the end of this chapter; it is used in three of the five sensors discussed in this thesis: the seepage meter, thermal diffusion (plant water status sensor) and permeameter.

Paper
Skinner, A.J. and Lambert, M.F. (2009). 'A log-antilog analog control circuit for constant-power warm-thermistor sensors – Application to plant water status measurement.' IEEE Sensors, Vol. 9, Issue 9, September 2009

Chapter 6. Evaluation of a warm-thermistor flow sensor for use in automatic seepage meters

Skinner, A.J. & Lambert, M.F. (2009). Evaluation of a warm-thermistor flow sensor for use in automatic seepage meters.
IEEE Sensors, v. 9 (9), pp. 1058-1067

NOTE:
The published paper is available online to authorised users at:

http://dx.doi.org/10.1109/JSEN.2009.2024056

6.1 Background

The original intent of this thesis was to develop a warm-thermistor flow meter capable of making very slow flow measurements in a variety of flow applications in environmental engineering; just 'how slow?' was unknown. Nevertheless, it was assumed that one of the most workable models would include the 'thermal-field distortion' model using the principles first espoused by Thomas (1911) and described in Section 2.3. This design uses a central heater, with matched thermistor temperature sensors on either side of it, to determine the flow-proportional thermal field distortion caused by convected heat being carried downstream while carried in both directions by thermal diffusion. This emphasis on matched thermistors led to involvement with the thermal stratification measurement group at the University and to the development of the smart thermistor strings described in Chapter 3.

While it would have been simple enough to create such a one-dimensional thermal flow-field distortion sensor in a pipe (as, indeed, have various other authors) this design is less suited to two- and three-dimensional flows in open water bodies. Besides, if one is

going to create a constant power heater, the challenge is to do it with a sensitive thermistor rather than a zero temperature-coefficient heater resistance as one can then also know something about the temperature of the heater and how it is affected by its immediate environment. This led naturally to research into the properties and flow performance of the thermistor heater alone and its potential to measure ambient temperature, flow and thermal diffusivity – the latter measurement being the subject of Chapter 5 of this thesis.

The development of a 'constant power' sensor, based on the circuitry developed in Chapter 5, offered various potential advantages as outlined in the Literature Review summary in Section 2.5.5. These included more sensitivity than constant temperature probes to very slow flows, promise of greater immunity to bio-film build-up, the generation of temperature differences at its output and inherent self-referencing such that no sensor matching is required. Development thus proceeded away from the original thermal field distortion concept towards that of a single thermistor and its interaction with its environment.

More importantly, the Literature Review concluded that: -

> *"A further limitation to the measurement of very slow flows has to be the essential nature of thermal flow sensors. In generating heat, they inevitably create a thermal plume whose buoyant convective upthrust will carry heat away from the sensor, especially when cross-flows to be measured are likely to be slower than these self-same vertical buoyant plume flows. Rather than attempt to cancel these flows, methods need to be found to work with them if flows below 3 mm/s are to be measured."*

In this chapter, these tests on the sensor's response in a vertical flow application – seepage meters – are put to the test through models and laboratory-based experimental work.

Much detail is given in the paper that arose from this chapter, and this has not been repeated in this background briefing. Rather, some of the salient points are described in more detail. The motivation for the development of an automated seepage meter is given in Section 6.1.1. An expanded proof is given in Section 6.1.2 of the Hagen-Poiseuille Equation as it applies to the flow meter calibrator in the laboratory. Additional circuit schematics and photographs of the actual equipment used are given in Sections 6.1.3 to 6.1.6. Problems arose when early test results showed flow instabilities in the test rig despite the correctness of the mathematical theory; these were traced to turbulent flows

in the control pipe, as explained in Section 6.1.7. Changing the control-pipe dimensions without compromising the relevant length-to-area ratios resolved this.

In short, the paper should be read before this chapter, as only ancillary information is given here.

6.1.1 Motivation for the development of a groundwater seepage meter

The interconnection between surface and groundwater sources is of increasing interest to scientists, especially where groundwater is injecting massive amounts of salt into river systems. One such example can be found in the downstream reaches of the 2750-km long Murray-Darling river system in southeastern Australia. Hundreds of tonnes of salt per day have historically entered the Murray River in South Australia alone (Jolly *et al.*, 1997). Tree clearing for agriculture has resulted in widespread dry-land salinity, but irrigation areas alongside the river have exacerbated this problem. Plants increase soil salinity by extracting fresh water from brackish water during transpiration, leaving salts behind to accumulate in the soil. The use of already-saline irrigation water on perennial crops necessitates the addition of a 'leaching fraction' to the amount of irrigation water applied; this extra water is designed to flush toxic salts out below the crop root-zone. Such root zone leaching has the unintended consequence of putting pressure on local aquifers, leading to mobilization of groundwater towards the river bottom at the lowest point at the landscape. This adds further salt to the river water, which is in turn recycled further downstream onto other crops and other aquifers. Engineered salt interception schemes located at Waikerie, Woolpunda, Bookpurnong, Rufus River and Loxton in South Australia have ameliorated this problem somewhat. These salt interception schemes parallel to the course of the river are essentially pumped bore fields that have been designed to intercept saline ground water and reduce river salinity levels. The output from the bore fields is pumped away from the river valley for disposal in sealed evaporation pans at Stockyard Plains outside Waikerie. However, careful management of pumping rates is necessary to prevent extraction of valuable river water via the river bottom through the connecting aquifer. Development of a seepage salinometer capable of measuring bi-directional salt fluxes at this boundary between surface and groundwater fits well with the theme of this thesis – the measurement of very slow flows in environmental engineering. A suitable salinity sensor for incorporation into such a seepage meter has been described in Chapter 4, although it was developed for measuring the salt accumulation in the agricultural soils within the same irrigated area at Oxford Landing near Waikerie.

In any event, the creation of a bi-directional seepage meter proved to be beyond the scope of this current paper, and a uni-directional seepage meter was presented; this proved capable of detecting flow velocities an order of magnitude below heat pulse, ultrasonic and electromagnetic seepage meters described in the literature. The measurement of bi-directional flows and salt-fluxes were set aside for other papers.

6.1.2 Expanded Proof of the Varying Head Flow Controller

One of the reviewers of the paper at the end of this Chapter questioned the validity of the losses in the system shown in Figure 35. This expanded proof was not published, but sought to prove the validity of the method from first principles; it is a direct analogy of the apparatus described in the paper ***'Evaluation of a warm-thermistor flow sensor for use in automatic seepage meters'***

Our aim is to show that head losses due to friction depend only upon the height difference between the two free-air surfaces in two reservoirs open to atmosphere and connected by a small bore pipe.

This proof is independent of the slope of the input pipe with respect to the two tanks of Figure 35, although our experiment shows the flow control pipe in the horizontal position because this maximizes the fastest flow rate.

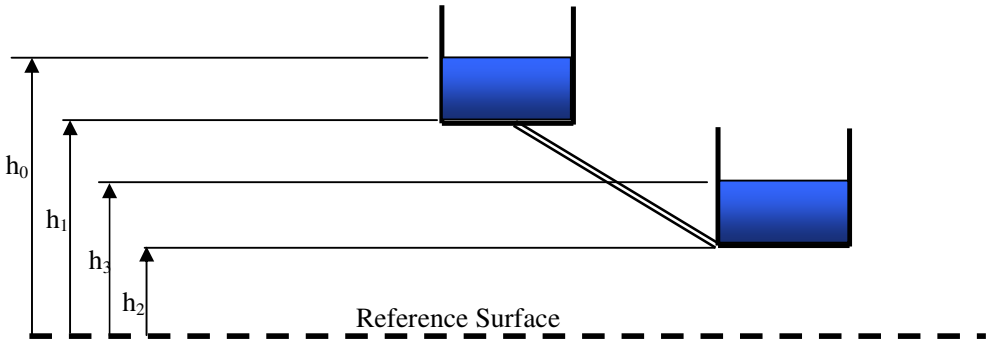

Figure 35 Two reservoirs open to atmosphere have surface water heights of h_0 and h_3 above a nominal reference plane. The reservoirs are connected between heights h_1 and h_2 (in meters) by a pipe inside of which friction (viscous) forces result in an effective 'head loss' h_L.

Bernoulli's Equation states that the energy ***H*** (in meters of head) along a flow streamline is constant. Therefore

$$\frac{P_0}{\rho g} + \frac{u_0^2}{2g} + h_0 = H_0 \qquad (6.1)$$

$$\frac{P_1}{\rho g} + \frac{u_1^2}{2g} + h_1 = H_1 \qquad (6.2)$$

$$\frac{P_2}{\rho g} + \frac{u_2^{\,2}}{2g} + h_2 = H_2 \tag{6.3}$$

$$\frac{P_3}{\rho g} + \frac{u_3^{\,2}}{2g} + h_3 = H_3 \tag{6.4}$$

where $\boldsymbol{P_x}$ is the static pressure of the fluid at height $\boldsymbol{h_x}$, $\boldsymbol{\rho}$ is the density of the fluid (assumed to be uniform throughout), $\boldsymbol{g}$ is the acceleration due to gravity, $\boldsymbol{u_x}$ is the velocity of the fluid at a point.

Flows within the tanks are assumed to occur without energy losses, so that

$$H_0 = H_1 \tag{6.5}$$

and

$$H_2 = H_3 \tag{6.6}$$

but friction losses $\boldsymbol{H_L}$ occur within the narrow-bore pipe such that

$$H_2 = H_1 - H_L \tag{6.7}$$

and

$$\therefore H_3 = H_0 - H_L \tag{6.8}$$

where

$$H_L = f\left(Q_{pipe}, r_0, \mu, L\right) \tag{6.9}$$

from the Hagen-Poiseuille equation where

$$\frac{\Delta P}{\rho g} = H_L \tag{6.10}$$

Combining these equations gives

$$\frac{P_3}{\rho g} + \frac{u_3^{\,2}}{2g} + h_3 + H_L = \frac{P_0}{\rho g} + \frac{u_0^{\,2}}{2g} + h_0 \tag{6.11}$$

But velocities $\boldsymbol{u_3}$ and $\boldsymbol{u_0}$ at the surface of the two tanks are approximately zero, and the pressures $\boldsymbol{P_3}$ and $\boldsymbol{P_0}$ of these two surfaces with respect to atmospheric pressure are also zero.

$$\therefore H_L = h_0 - h_3 \tag{6.12}$$

That is, head loss H_L due to friction in the small-bore control pipe between the main tank and the sensor vertical standpipe - described by the Hagen-Poiseuille equation - are dependent entirely upon the height difference between the two water surfaces in the main tank and standpipe.

6.1.3 'Plunging flow calibrator' control circuit

The paper at the end of this Chapter describes a plunging probe apparatus that moves a vertical thermistor probe up and down at different velocities to measure the flow-independent thermistor temperature $\boldsymbol{T_F}$, or stops it at the limits of travel to obtain the still water temperature $\boldsymbol{T_S}$. A description of the control circuit that automates this process is

given in this section. But first, the description of the precision flow sensor drive apparatus and its purpose.

The generation of precise flow velocities down to 0.1 mm/s was achieved using a single DC-Micromotor (Faulhaber 2224R012S) coupled to a range of precision all-metal spur gear heads (Faulhaber 22/2) as shown in Figure 36 and Figure 38.

This motor-gearbox was directly coupled to a precision shaft-encoder (Unidata 6509) driving a beaded cable to provide a non-slip linkage to the probe on one-side and a counterweight on the other. This assembly allowed the sensor to be moved vertically through a very still water column in a 20 litre Dewar vessel. The linear velocity v of the sensor, in mm/s, was calculated as $v = l/t$ from the known distance l in millimeters travelled by the probe (and read off the shaft encoder's LCD display) in a time period t measured with a stopwatch.

A control circuit was built to drive the probe up and down through the water column at various speeds (achieved by using different motor drive voltages for each gearbox ratio). The thermistor resistance was measured while the probe was operating in various ambient, self-heated, stopped, forward and reverse modes. These operating sequences are shown in Table 2.

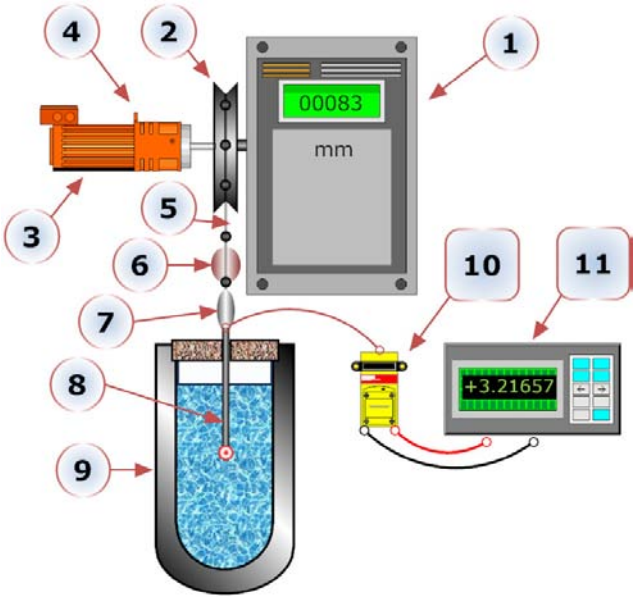

Figure 36 'Plunging-probe' sensor calibration rig for generating very slow linear velocities for a warm-thermistor probe in an isothermal still water tank. A shaft-encoder [1] having a pulley wheel [2] of 500mm circumference, precision bearings and 1 mm resolution is driven by a DC-Micromotor [3] coupled to a precision all-metal spur gear head [4]. A beaded line [5] is balanced across this pulley wheel by lead counterweight [6] and the lead weight [7] on the stainless-steel shaft [8] carrying the thermistor. The motor raises and lowers the probe through the very still temperature-stable water body in the 20-litre Dewar vessel [9]. The output of the constant-power bridge circuit [10] is recorded by the 6½-digit Keithley K2000 recording multimeter [11]. Power supply and control circuits are not shown. The actual apparatus is shown in Figure 39.

TABLE 2 MEASUREMENTS OF PROBE TEMPERATURE WERE MADE UNDER EIGHT DIFFERENT CONDITIONS FOR EACH OF THE 23 SIMULATED FLOW SPEEDS. THIS CALIBRATION REGIME ENSURED THAT ALL POSSIBLE COMBINATIONS OF FLOW CONDITIONS OCCURRED FOR EACH FLOW VELOCITY.

Stage #	Ambient/Heated	Stopped/ Moving	Dir'n
1	Ambient	Stopped	-
2	Ambient	Moving	Down
3	Heating	Moving	Down
4	Heating	Stopped	-
5	Ambient	Stopped	-
6	Ambient	Moving	Up
7	Heating	Moving	Up
8	Heating	Stopped	-

The temperature difference T_S-T_F between stages 3 and 4 ('rising flow') and 7 and 8 ('reverse flow') was used to determine the sensor's response at each flow speed. Voltage measurements were synchronized with each operating condition, and recorded within the K2000 voltmeter's internal memory under computer control. The control circuit was created using standard CMOS logic gates and analog switches (Figure 37) to select reference voltages (bottom-left) that are used via buffer amplifiers to drive the precision geared motor drives to stop, move up or move down. The timing of these operations is keyed to the Keithley K2000 voltmeter by using the 'measurement ready' output to step the circuit on in synchronism with the temperature voltages from the thermistor. The coloured LEDs (top-right) indicate the state of the apparatus.

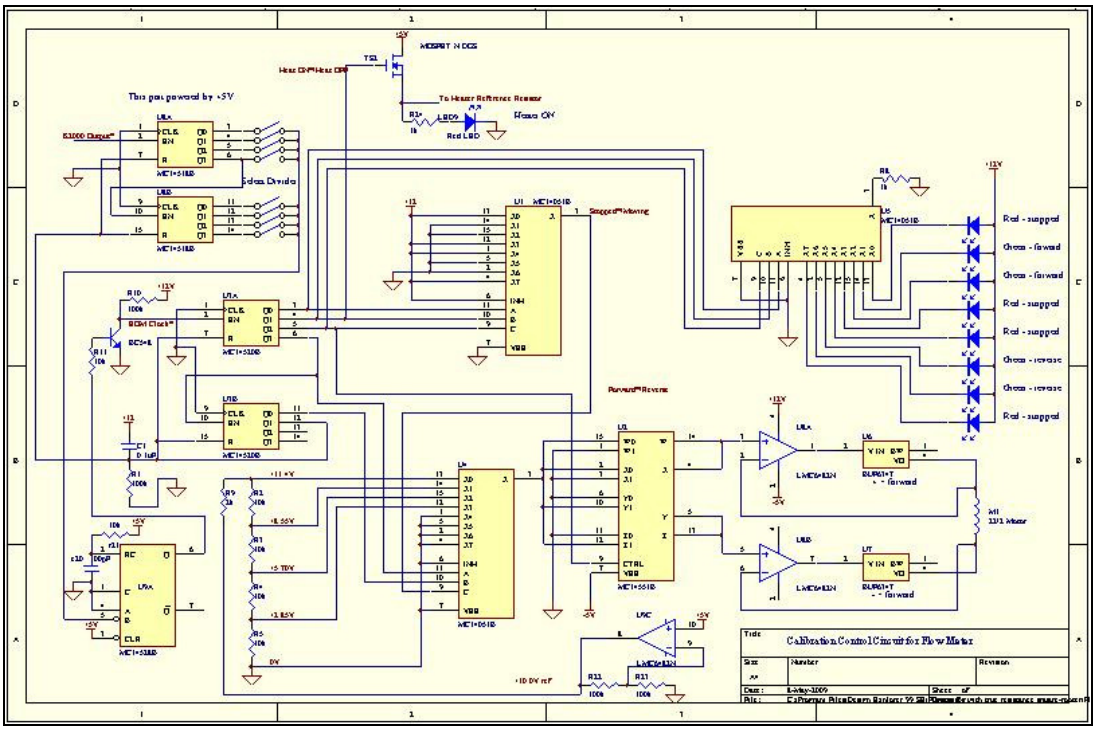

Figure 37 Logic-based control circuit for the plunging probe calibration rig

6.1.4 The workbench…

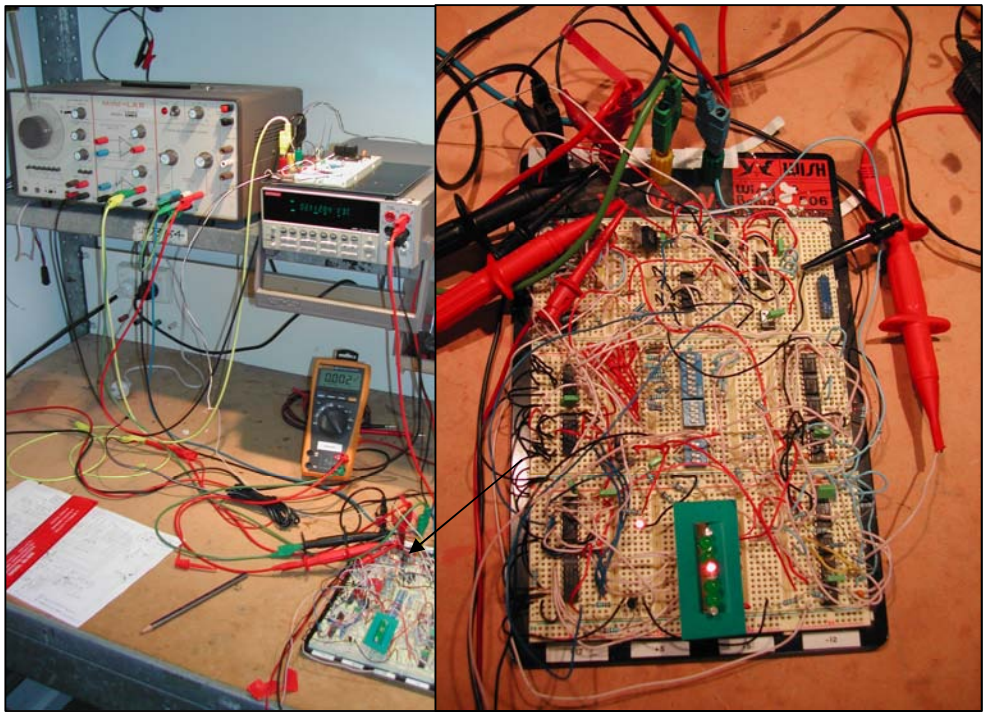

Figure 38 The Keithley K2000 6½-digit recording multimeter (top-centre) is programmed from a customized computer program to carry out 1024 measurements at a rate of (typically) every second, measuring the output voltage of the double-bridge constant-power circuit. The close-up of the control and measurement circuit on the right-hand side shows the bread-boarded circuit of the schematic shown in Figure 37. It's not lovely, but it worked.

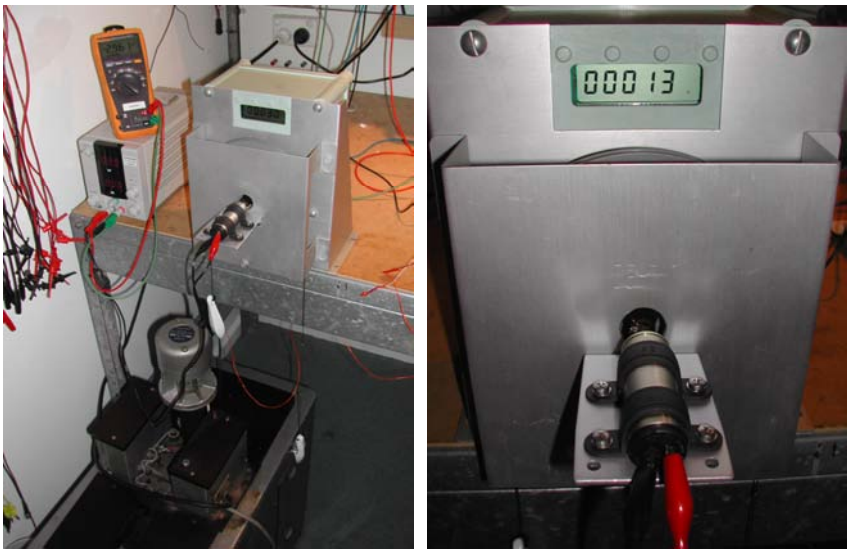

Figure 39 The Unidata shaft-encoder (left-top) monitors the vertical height of the probe balanced across its pulley wheel, which is driven directly by the motor-gearbox unit (right-centre). The Dewer flask sits below the shaft-encoder, and the beaded cable supporting the sensor probe passes through a small hole in the cork lid.

6.1.6 Transient flow calibration apparatus

The paper at the end of this Chapter describes a transient flow calibration apparatus that allows water to fall downwards over a vertical thermistor probe, from a maximum velocity at ***t=0*** to a final velocity of zero. This section contains photos (Figure 41, Figure 42 and Figure 43) of the basic experimental apparatus, including the water height sensors used to determine the system time-constant. But first, the description of the apparatus and its purpose: -

"However, a calibration environment was sought that more closely resembled that found in a vertical seepage meter standpipe, and one which would allow a single-sweep calibration encompassing all flow velocities consecutively. The flow generation process developed is reliant upon first principles and upon measurands - time and depth - that can be measured accurately and with commonly available equipment. The sensor is placed in a vertical pipe environment as shown in Figure 40, just as it would be in the throat of a seepage meter.

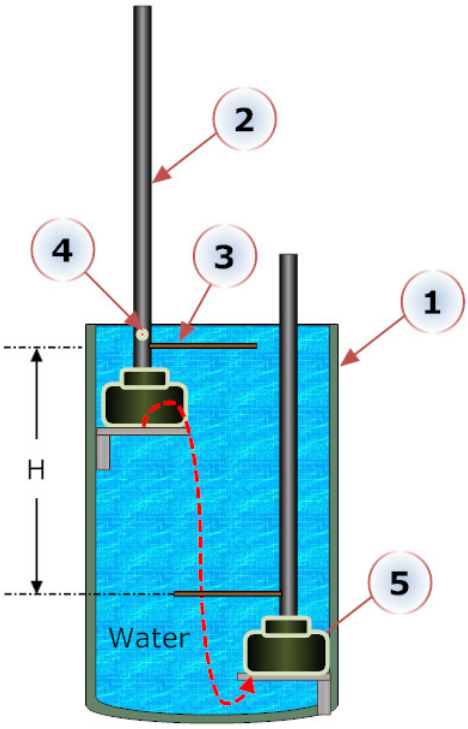

Figure 40 A 'single-sweep' seepage meter calibration system. This step-change variable head seepage meter calibrator uses a Hagen-Poiseuille flow controller. A 240-litre container [1] holds a 900-mm depth of well-mixed water at room temperature. The thermistor sensor located at level [4] is submerged by 50 mm when the 1000-mm high x 27.5 mm diameter bore vertical calibration sensor standpipe [2] and electronic control circuit [5] are in the top left-hand position. In this initial position, water in the vertical sensor standpipe is at the same level as the surface of the water in the main tank. When the instrument is plunged to the lower right-hand position, an instantaneous differential head pressure '*H*' is applied to opposite ends of the (coiled) Hagen-Poiseuille flow control pipe [3], which has a 5-mm bore and a length of 33m. *H* is the 'final height' of the step-change in water pressure. The electronics has been incorporated into the standpipe base in order to stabilize its temperature.

This calibration rig generates a rising flow, and the sensor's thermal heat field and any buoyant circulating currents are subject to the same real boundary conditions present in a field deployment of this type of sensor in a seepage meter. The flow regulator to the sensor stand-pipe is a simple horizontal small-bore pipe which controls the flow rate based only upon the differential pressure head, the dimensions of the pipes and physical properties of the water; these are described by the Hagen-Poiseuille equation."

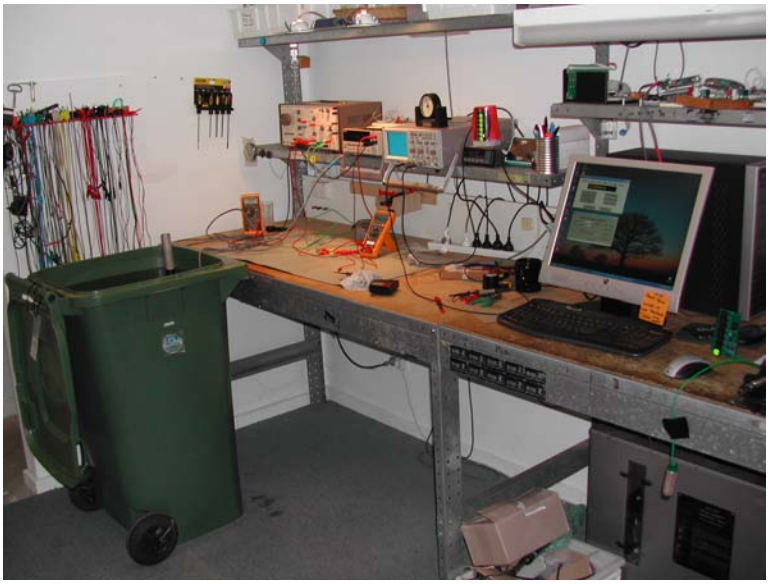

Figure 41 The seepage meter standpipe can just be seen above the water level in the tank at left.

Figure 42 The standpipe is shown in the water column, with the electronics below and the Hagen-Poiseuille flow control pipe to the left (the latter was later replaced by 33 m of wound plastic pipe to lower the Reynolds Number below turbulent flow speeds). Rather than step-change height, the method shown here purged the vertical standpipe using compressed air. Uncapping the top of the standpipe allowed water to flow back in with a first-order time-constant.

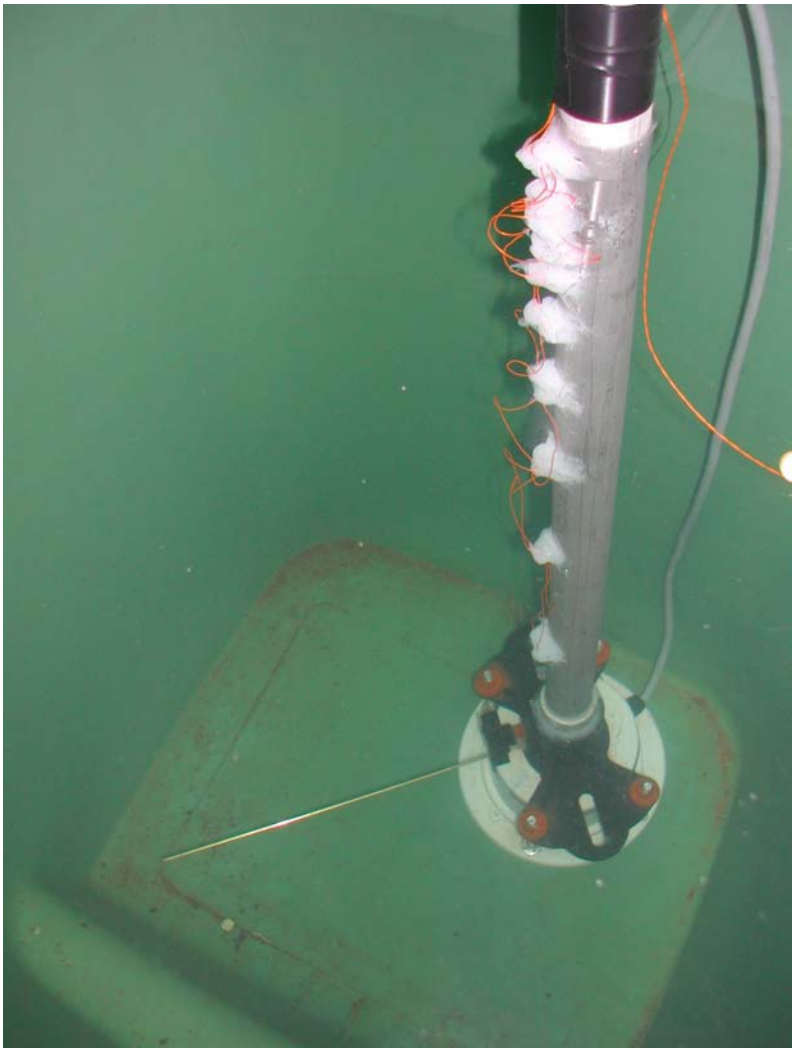

Figure 43 The seepage meter standpipe is shown with the 'level sensing' thermistors arranged in a logarithmic spacing up though its height. The level sensor spacings were chosen to allow roughly equal time intervals for the arrival of the water-air front at each heated sensor as the water level rose up through the column with decaying velocity, flowing in from the main tank through the flow control pipe on the left.

6.1.7 Flow transition from laminar to turbulent in the control pipe

The dimensions of the flow control pipe shown in Figure 42 and Figure 43 were computed to bring the range of upwards flow velocities in the seepage meter standpipe into the velocity range between 0 and 5 mm/s. A full description of the apparatus and dimensions is given in the paper at the end of this Chapter, but what is important here is the explanation of how the 'control pipe' dimensions were first calculated to be arithmetically correct, but hydro-dynamically wrong.

The maximum flow rate v_{max} (m/s) in the sensor stand pipe occurs at $t=0$ when $h(t)=0$, and is: -

$$v_{\max} = \frac{a}{A} \cdot \frac{r_0^{\,2} \cdot \rho \cdot g}{8\mu \cdot L} H \tag{6.13}$$

The response of the system describes the rate at which the height ***h*** of the water in the vertical standpipe falls with time ***t*** and is an exponential equation based upon the system dimensions of control pipe length ***L***, initial water height ***H***, small-bore cross-sectional area ***a*** and large-bore cross-sectional area ***A,*** density ***ρ***, viscosity ***μ*** and gravitational constant ***g***: -

$$h(t) = H - e^{\left(\frac{-t}{\tau} + \ln H\right)} \tag{6.14}$$

where

$$\tau = \frac{A}{a} \cdot \frac{L}{H} \cdot \frac{8}{r_0^{\,2}} \cdot \frac{\mu}{\rho \cdot g} \tag{6.15}$$

The 'time-constant' ***τ*** describes the first-order frequency response of the system and is the time taken in seconds for the height of the water ***h(t)*** in the sensor standpipe to rise to 63.21% of the final height ***H***. It is this system time-constant that is used to derive the flow velocities ***dh/dt*** at each moment during an experimental run.

What was not initially clear from these equations is that the Hagen-Poiseuille equation that governs the time constant of this flow rig requires laminar (non-turbulent) flows in the control pipe. So while the ratio ***L/a*** of the control pipe would seem to allow the dimensions of the precision metal control pipe shown in Figure 43, these dimensions must be adjusted to keep the control pipe flow velocity low enough to prevent turbulence. Such turbulence gives rise to 'hydraulic friction' that limits the maximum rate of water entering the vertical seepage meter standpipe. The full effect of this can be seen in data from an early run, shown in Figure 44. Although the dimensions of the control pipe satisfy the criteria for computing the necessary system time-constant, experimental results were poor because the high Reynolds Number (high velocity in the control pipe) resulted in non-laminar turbulent flow.

Accordingly, the bore size was increased to 5 mm (an increase in the cross-sectional area ***a***), necessitating an increase in the control pipe length ***L*** to over 30 m, resulting in correct operation.

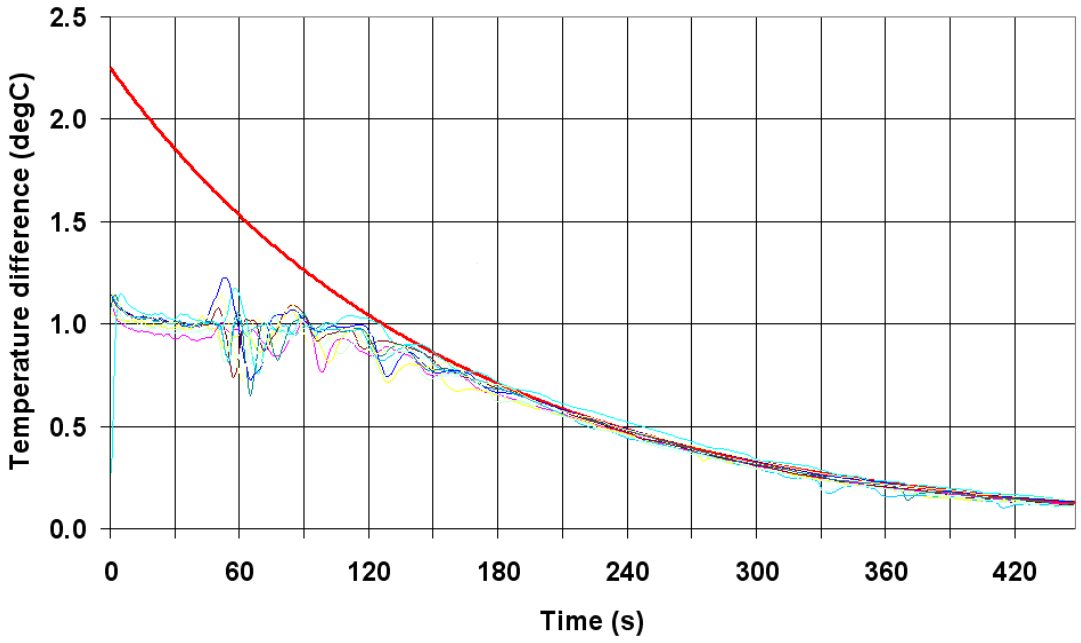

Figure 44 At high flow rates in the 'control pipe' (between 0 and 180 s into the run), flow becomes turbulent (high Reynolds Number) and limits flows in the vertical seepage meter standpipe, as shown by the deviation and oscillations of the flow sensor traces with respect to the expected (red) curve.

Paper

Skinner, A.J. and Lambert, M.F. (2009). 'Evaluation of a warm-thermistor flow sensor for use in automatic seepage meters.' IEEE Sensors, Vol. 9, Issue 9, September 2009

Chapter 7. A null-buoyancy thermal flow meter: Application to the measurement of the hydraulic conductivity of soils

Skinner, A.J. & Lambert, M.F. (2009). A null-buoyancy thermal flow meter with potential application to the measurement of the hydraulic conductivity of soils.
IEEE Sensors, v. 11 (1), pp. 71-77

7.1 Background

7.1.1 Seepage meters and mechanical valves

One of the most helpful aspects of journal publication during the course of this thesis was the feedback from reviewers that once or twice sparked a new line of thinking. This was true of the paper on seepage meters where the final reviewer – a man who clearly knew something about seepage meters – suggested that blocking the flow to obtain the still water temperature T_S of the warm-thermistor would cause pressure to build up within the buried seepage meter funnel. He suggested that a bypass valve be installed, and the need for such a mechanism was duly added to the 'Discussions and Conclusions' as follows: -

> "A simple linear gain relationship has been found between the temperature difference T_S-T_F and the flow velocity v …….Very slow [upward] flow measurements have been demonstrated for large-bore vertical pipes ….. In a working seepage meter standpipe the flow would need to be controlled by a valve arrangement to determine the still-water temperature T_S (valve shut: no flow) and T_F (valve open: flow established)."

That such an inelegant and expensive solution as an underwater mechanical valve nullified all the previous efforts to create a very simple vertical flow design set in motion the events that led to this new paper on ***downward*** flows. Besides, this seepage meter was

still only able to measure uni-directional (***upward***) flows from the sediments into the river bottom. A bi-directional seepage meter capable of measuring reverse flows would be of practical interest in capturing extraction of river water back into pumped aquifers such as those adjacent to the Murray River as part of the salt interception scheme described in Section 6.1.1.

Ironically, this next paper solved the initial conundrum presented by the reviewer with his suggestion for mechanical valves; how does one determine still water temperature without shutting off the flow? The linear nature of temperature rise in a self-heating thermistor with increasing power dissipation in still water allows this to be determined in a single point calibration process in still water in order to determine the '***dissipation constant***' of a particular thermistor. The ability of the instrument to sense ambient temperature T_A as well a self-heated temperature allows T_S to be derived from T_A, as explained in the following extract from the paper:

> Changing the sensor power-dissipation level with the sensor in still water will change the sensor temperature. The CFD model used by Skinner and Lambert (2009:B) was re-run for a stagnant velocity of 0.001 mm/s at an ambient temperature of 20°C. The temperature rise of the modelled sensor as power dissipation increases is shown in Figure 3 [of the paper]. The slope of this linear response is 13 mW/°C in still water, and corresponds to the common industrial concept of thermistor '***dissipation constant***' $DC = \frac{P(mW)}{T_S - T_A}$
>
> where P is the power (in mW) dissipated as heat by the thermistor, T_S is the temperature of the warm thermistor under still water conditions (although a thermal plume rises above the thermistor) and T_A is the background ambient temperature of the fluid at some distance from the sensor, or as measured via the sensor resistance when the thermistor is dissipating less than 100μW of power.
>
> This temperature rise as power levels change must be subtracted from the sensor response in order to extract the sharper temperature rise due to flow stagnation. This is accomplished by returning to the concept of the still water temperature T_S that can be subtracted from the flow temperature T_F to remove ambient background temperature data from the returned signal. T_S is measured during laboratory tests described in this paper, but can be estimated under field conditions knowing ambient water temperature T_A and applied power level using the linear fit equation $T_S = (P/DC) + T_A$

Of the various possible solutions for avoiding mechanical valves, the most obvious was an 'inverted U-shape' sensor with warm thermistor sensors in both arms; in this fashion, at least one of the arms would be subjected to a rising flow. Figure 45 shows how such an inverted U-tube could be used for measuring bi-directional seepage fluxes.

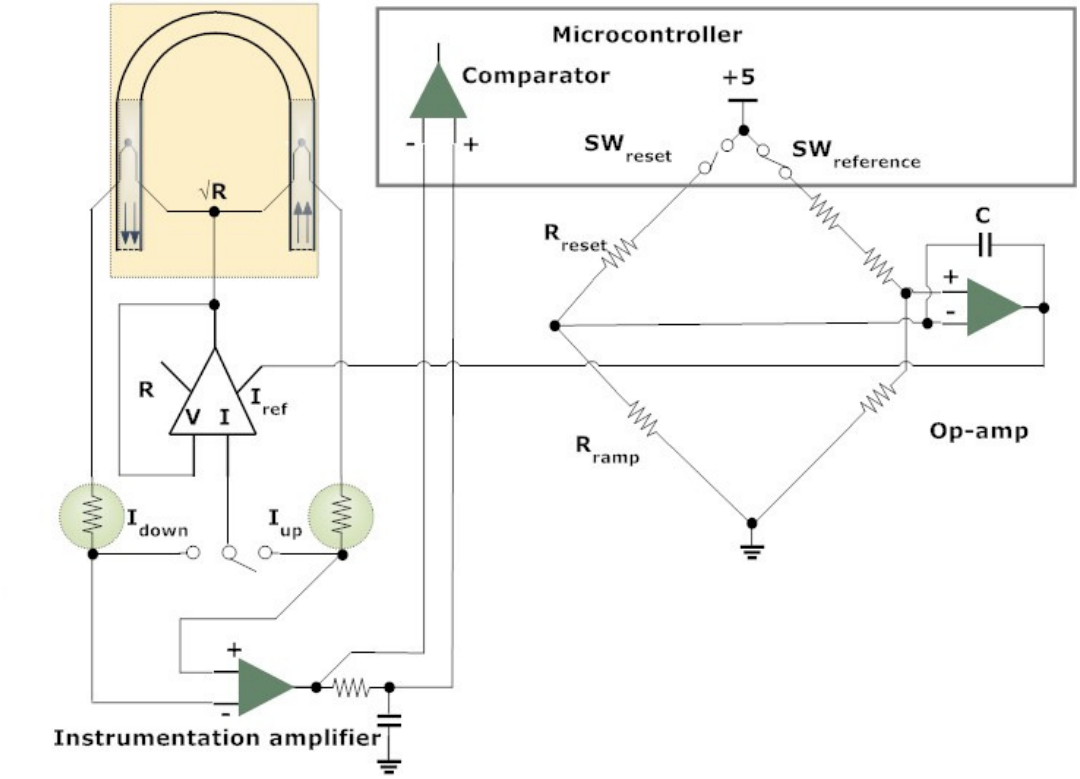

Figure 45 A bi-directional flow cell and electronics, configured as a differential flow detector, with the upward flow sensor being the master in the control loop, as set by the switch. The voltage across the upward flow sensor would be imposed across the slave thermistor in the downward flow section of the inverted tube. The difference in the thermistor currents – as detected by the instrumentation amplifier – would be the signal.

7.1.2 Buoyant plumes under downward flow conditions

While this inverted U-tube looked to be valid, the response of a warm thermistor sensor in a downwash flow, especially one thermally-polluted by the upstream sensor on the other side of the inverted-U tube, was unknown. It was known that a rising thermal plume was enhanced by upward flows, but would a downward flow actually cause the inevitable thermal plume to flip downwards? Was there a point at which the upthrust of the plume balanced the downward flow? If so, what would happen? Surely this stagnation point would be power dependent as, logically, this plume size must increase as the applied thermistor power increased, as the buoyant plume does not exist under zero power conditions? Surely this would create a non-linear response compared to the

upward-flow sensor's linear response, making a differential measurement between upward and downward flow non-linear?

To answer these flow response questions, a return to the CFD (computational fluid dynamics) modeling was necessary; Dr Allan Wallace, whose consulting business specializes in CFD and the thermodynamics of fluids, carried out this modeling. (Allan is acknowledged as a joint author of this last paper – he carried out the modeling and the engineering analysis, while I supplied the concepts, experimental work, writing and analysis). The results of this modeling are shown in Figure 46, and as expected, the downward flow response was non-linear and therefore the differential response reflected that non-linearity.

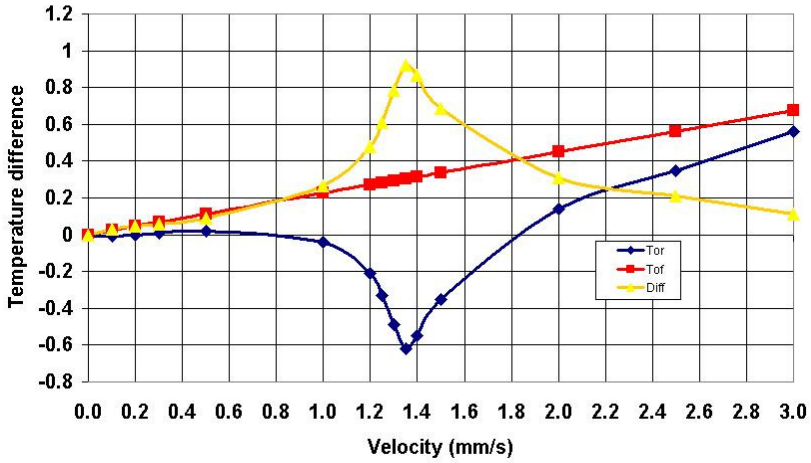

Figure 46 Maximum thermistor temperature occurs at a 1.35 mm/s downward flow that exactly balances the natural convective upward flow for a 40 mW heat output. This leads to a stagnation zone around the thermistor tip that results in maximum heating of the sensor under any flow conditions. The red trace (squares) is the sensor response for upward flows. The blue trace (diamonds) is the sensor response for downward flows. The yellow trace (triangles) is the temperature difference between upward and downward flow values.

7.1.3 Flows in the landscape – 'hydraulic conductivity' and drainage meters

A sensor for the measurement of very slow downward flows has all the earmarks of being a solution to a very different problem – how to automate the measurement of one of the most common yet least measured environmental slow flows – the rate at which rainfall percolates into the surface of the landscape. Knowing that such a problem even existed owes much to early research work in the course of this thesis into ***drainage*** rates below crops – another poorly understood and almost intractable slow-flow measurement problem. A great number of environmental/hydrological models make use of the water balance equation that seeks to describe how water enters, leaves and is stored in the landscape. In simple form, this general equation can be written as

$$P = Q + E + \Delta S \qquad (7.1)$$

where P is the precipitation or rainfall on the input side of the equation, and Q, E and ΔS are the runoff, evaporation and change in soil storage terms, respectively, on the output and storage side of the equation. Of these terms, rainfall, runoff and evapotranspiration have had a great deal of attention and are well understood and widely measured by various water and weather authorities.

Changes in soil storage are, however, more difficult to quantify, particularly because these measurements are underground and so more difficult and expensive to make than measurements of surface flows such as rainfall and runoff. Changes in surface soil moisture storage can be estimated using soil moisture content sensors (neutron probes, capacitance probes, time-domain reflectometers and so forth). The rate of percolation into the landscape versus runoff, and the 'deep drainage' below crop root zones towards the water table, occur at very slow rates, mobilizing salt in semi-arid Australian landscapes. Soil moisture content sensors do not see these flows as they occur under saturated soil conditions where moisture content gradients disappear.

Work done by Bond and Hutchinson (2006) extended the development of the tube tensiometer (Hutchinson and Bond 2001) to incorporate two tube tensiometers to measure the local vertical hydraulic gradient under dry-land cropping systems. The tube tensiometers operate in the saturated 0...10 kPa soil matric potential range where most drainage flows occur. They function by measuring the height of a 'hanging' water column using pressure transducers at the bottom of a 1m tube packed with diatomaceous earth and buried in the soil below the root zone of a crop [1m head = 10kPa water pressure]. Two of these tube tensiometers were combined in the '***tube tensiometer drainage meter***' shown in Figure 48 and Figure 49 to measure the hydraulic gradient $d\psi/dz$ in the soil between tensiometer tips having a vertical spacing of 200 mm, requiring matching of the two pressure sensors to ±5 mm. The high-resolution sensor electronics of Figure 50 were built using an adaptation of the technology in Figure 17 and Figure 18 in what was once again an application needing well-matched and temperature-corrected sensors. The electronics worked well, but the pressure transducers exhibited such a grossly non-linear temperature coefficient that satisfactory pressure sensor matching proved to be impossible.

The calculation of drainage flux [***mm/day***] from the '***counts'*** output of the sensor interface circuitry is shown in Figure 47.

The equation to calculate soil water suction ψ [mm] from the pressure output P_c [counts] and the temperature output T_c [counts] is:

$$\psi[mm] = -\left(A + B*P_c + C*T_c + D*P_c*T_c\right)$$

The hydraulic gradient $\Delta H/\Delta Z$ is given by:

$$\Delta H/\Delta Z = 1 + \left(\psi_{upper} - \psi_{lower}\right)/200$$

The drainage D [mm/day] is given by:

$$D = \Delta H/\Delta Z * K\left(\overline{\psi}\right)$$

Where K is the hydraulic conductivity [mm/day] at the average soil water potential $\overline{\psi}$,

$$\overline{\psi} = \left(\psi_{upper} + \psi_{lower}\right)/2$$

Figure 47 Calculation of drainage flux from ADC '*counts*' and 'temperature counts' of Figure 50. (Bond and Hutchinson 2006). *A*, *B*, *C* and *D* are calibration-derived coefficients.

While the drainage meter thus developed responded to the vertical hydraulic gradient in the soil, it relied upon the application of Darcy's Law (the drainage equation ***D*** in Figure 47) to quantify the 'water flux' percolating down through the soil profile to the water table. This in turn required knowledge of the soil's hydraulic conductivity, $K\left(\overline{\psi}\right)$. The authors state (rather wistfully): -

"The other practical difficulty in applying such a device is the measurement of hydraulic conductivity of the soil surrounding the tensiometers. The intention of the drainage meter design was to incorporate a method for measuring the hydraulic properties of the soil surrounding the depth of installation. Unfortunately, while the facility has been incorporated, a suitable technique for making the measurements has not been established. When the drainage meter was originally conceived, it was intended to adapt the method of Inoue *et al.* (1998). This method was tested but found not to be practical because of the difficulty in achieving a unique inverse solution to the water flow equations. The unsteady internal drainage method for characterising soil hydraulic properties in-situ was used in a demonstration trial. This method does not use the drainage meter itself, is time and equipment intensive, and is known to be difficult to implement in some soils. An alternative method that would use the current drainage meter setup has been identified (Kodesova *et al.*, 1999) but has not yet been fully tested."
from ***Bond and Hutchinson (2006)***

These early attempts at measuring water fluxes via a drainage meter – if only from the standpoint of the engineer responsible for the sensor interface electronics – served to sensitize the author to the problems of measuring hydraulic conductivity in soils. Other authors (e.g. Gee *et al* 2002) have since tackled these slow flows in the landscape using

drainage flux meters based on buried funnels, hanging water columns in fiberglass wicks and tipping bucket flow measurement mechanisms.

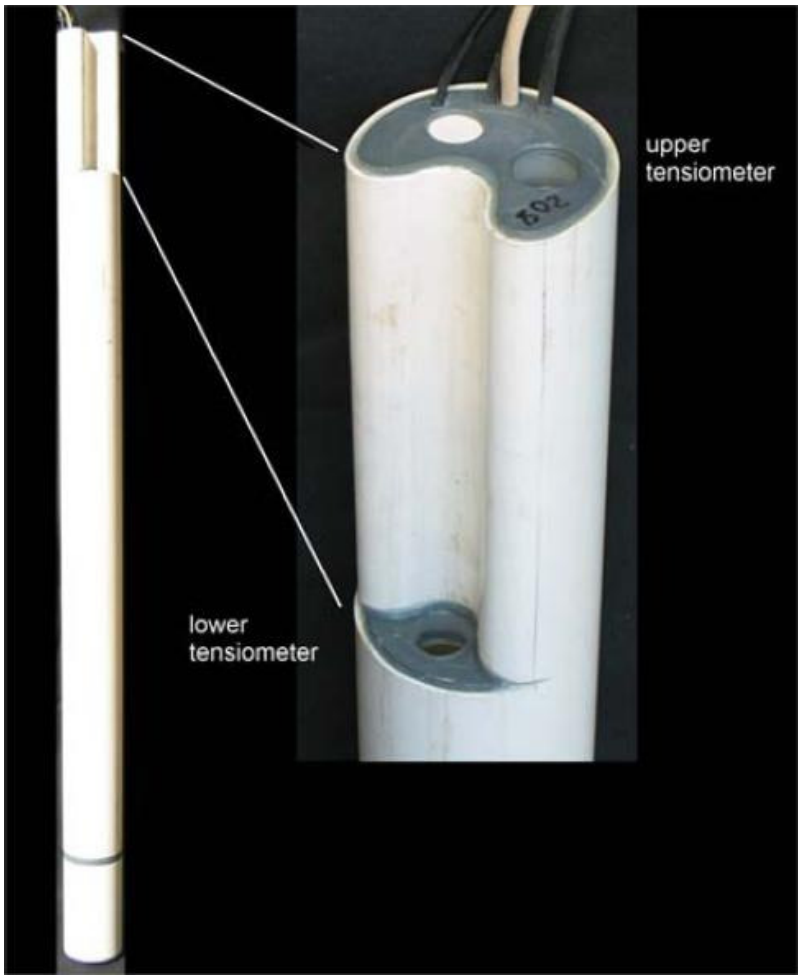

Figure 48 The 'tube tensiometer' drainage meter is shown on the left of the figure; the electronics of Figure 50 is incorporated into the base of this device. The detail of the sensing tip can be seen on the right, with the single (white) SDI-12 cable for data and command interchange leaving the instrument for the soil surface. The black vent tubes are needed to allow gauge pressure measurements for depth recording and to allow air trapped in internal pore spaces to vent to atmosphere as air enters the drainage meter. (Bond and Hutchinson 2006)

These instruments stand as field alternatives to the intensive and expensive research farm lysimeters where pieces of the landscape are mechanically isolated from their surroundings and weighed by underground load cells to monitor the water fluxes in the process while surrounded by large areas of the same crop (e.g. Meyer *et al* 1980, 1981, 1988 and 1990). Until the soil hydraulic conductivity can be known, efforts to quantify water fluxes below crops remains a qualitative rather than a quantitative measurement.

NOTE:
This figure is included on page 102 of the print copy of the thesis held in the University of Adelaide Library.

Figure 49 The tube tensiometer drainage meter is inserted down an augured hole several meters deep. The two sensor 'tips' of highly conductive diatomaceous earth are formed in-situ to connect the drainage meter to the soil profile. (Bond and Hutchinson 2006)

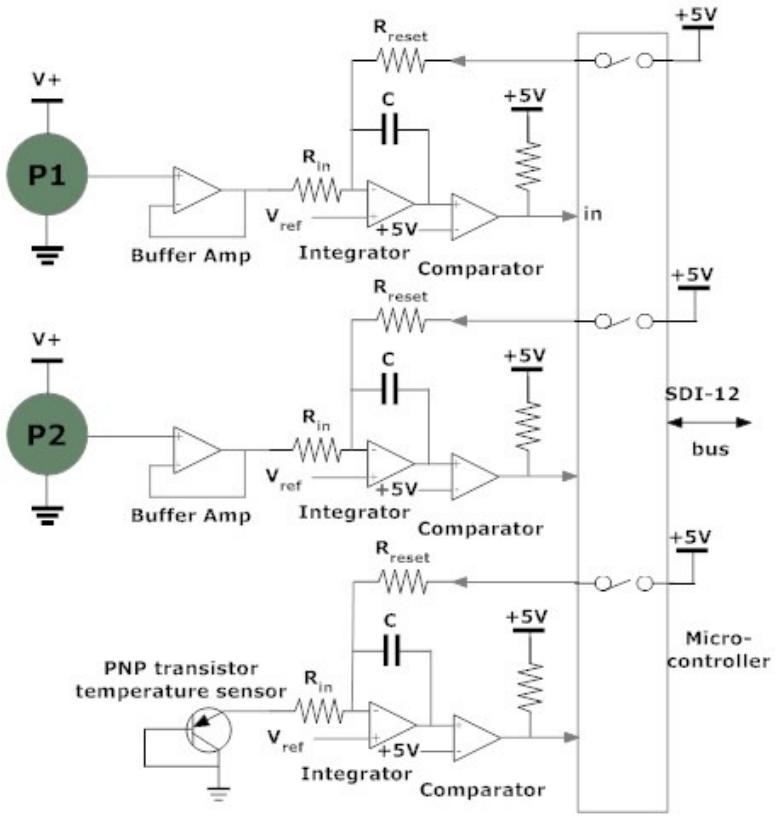

Figure 50 Multi-channel SVFC ADC with temperature correction, used for 15-bit pressure/depth measurements in the CSIRO 'drainage meter', which consists of twin tube tensiometers incorporating electronic gauge-pressure transducers P1 and P2 to monitor a 0-1m water head in each tube.

7.1.4 Permeameters and the measurement of hydraulic conductivity

In the meantime, work carried out by Clark (2004) on the Nuriootpa Agricultural Research Station in the Barossa Valley in South Australia identified drip irrigation on common red-brown soil types over long periods as a potential source of both physical and chemical degradation. Was there a method for continuous automated measurement of the hydraulic conductivity of soils – on the soil surface at least – that might give a better understanding of changes to soil structure and chemistry over long-periods of frequent irrigation cycles? ***Measurement of the very slow flow rate at which water enters the landscape seemed to be a potential application for a sensor designed specifically for the measurement of the very slow downward flows in nature occurring at the interface between air and soil during rainfall or irrigation***.

Whether or not water permeates into the soil or ponds on the surface and runs off depends upon the rate of rainfall and a number of physical properties of the soil including, importantly, its hydraulic conductivity. On a landscape scale, these soil properties affect groundwater and stream recharge, vegetation cover, plant water take-up and erosion. On a much smaller scale, the rate of infiltration of water into a soil surface may be dominated either by macropores (cracks, root channels and wormholes greater than one millimetre in diameter) or micropores (which dominate the soil properties of porosity and sorbtivity). These flows are termed 'preferential flow' and 'matrix flow', respectively. A soil's saturated hydraulic conductivity ($\boldsymbol{K_s}$) is measured using single- or double-ringed infiltrometers that create free water ponds on the soil surface at atmospheric pressure. A soil's unsaturated hydraulic conductivity ($\boldsymbol{K_\psi}$) is measured while water movement is occurring in unsaturated soils where air and water coexist in the soil pore spaces under the negative pressure conditions known as soil moisture tension, $\boldsymbol{\psi}$(kPa).

The measurement of soil hydraulic conductivity has been the subject of much scientific study under both field and laboratory conditions. Instruments for measuring this flow rate in the field are called either permeameters (Clothier and White 1981, Perroux and White 1988, Amoozegar 1989, Angulo-Jaramillo et al, 2000) or infiltrometers (Ankeny 1989, 1991), depending upon country of origin. These permeameters consist of a cylindrical graduated constant water head device to control and measure flow and a soil interface mechanism such as a single or double ring or a flat porous disc to connect the water reservoir to the soil surface as in Figure 51.

Figure 51 The CSIRO disc permeameter (Perroux and White 1989) for the measurement of tension-infiltration rate into soil. A small negative pressure of a few centimetres of water head is applied to the supply membrane; this prevents water running down wormholes or cracks in the surface (preferential flow), allowing the determination of the soil's unsaturated hydraulic conductivity (matrix flow).

Permeameters use the rate of fall of a water column in a tall small-bore cylinder as a measure of the very slow infiltration flow rates of water entering the soil surface (10 nm/s to 0.5 mm/s). Attempts to automate these flow rate measurements have relied largely upon pressure difference measurements (Ankeny 1989) that have been affected by the hydraulic noise generated by the bubble columns and elastic surface tension effects associated with them. The bubble columns have in turn been necessary to achieve the constant pressure heads that must be applied to the soil surface at negative tensions.

The journal paper arising from this chapter set out to examine an alternative design for this instrument based upon direct flow measurements using a new thermal null-buoyancy technique. Negative soil interface pressures ψ_S have been achieved using a column plug (saturated diatomaceous earth, as in Figure 52) having a negative hydraulic gradient ψ_P greater than the positive head pressure gradient ψ_H, eliminating the noisy bubbling mechanisms but requiring an overflow system to maintain the positive pressure under all soil flow conditions. That is

$$\psi_S = \psi_H - \psi_P \tag{7.2}$$

where

$$\psi_P > \psi_H$$

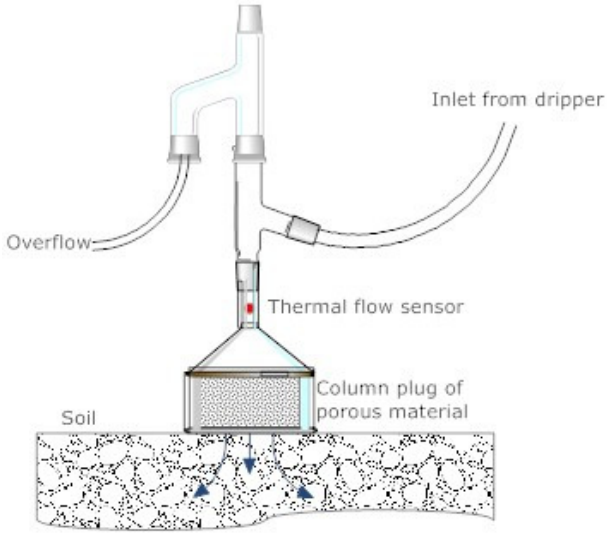

Figure 52. An unsaturated flow permeameter for irrigated agricultural soils. Arranging for the device to always overflow creates a constant head pressure ψ_H above the porous plug. The pressure drop across the porous plug ψ_P (by Darcy's Law) is designed to exceed the positive head pressure ψ_H of free water above the plug. This ensures that water is drawn out of the instrument at a soil moisture tension ψ_S ($=\psi_H - \psi_P$) such that flows only occur in soil micropores rather than in cracks and macropores.

Adequate water supplies are available in this application, allowing the design of an instrument to measure the long-term changes to the unsaturated soil hydraulic conductivity of soils under drip irrigation systems.

The complexities of understanding the effective operation of the null-buoyancy flow meter's general principles, and proving them in the laboratory, meant that work on such a permeameter as a complete instrument had to be postponed to some point beyond the completion of this thesis. The theme, however, remains central to this body of work in that it explores one of the central slow-flow applications that occurs in environmental engineering; the rate at which rainfall enters the landscape.

7.1.5 Early results: problems with thermal stratification in the test rig

The falling-flow test jig used to gain experimental confirmation of the modeled data is described in the paper at the end of this chapter. Early attempts to discover the null-buoyancy power versus velocity relationship ran into a variety of problems. The first of these resulted from self-induced thermal stratification in the vertical standpipe above the sensor. The 33m long flow control tube from this standpipe was plugged at the outlet end over the main water body to stop flow, the standpipe topped up and the sensor power level fixed. The whole apparatus was then allowed to settle for at least five minutes in order to allow momentum gradients to die away before flow measurements began. The average still-water temperature T_S was captured during this period and later used to

extract the background temperature from the data set. Sampling of the concentric thermistor commenced at a 1Hz rate to a precision of better than 0.001°C as the standpipe water level began to fall naturally, driven by the head pressure difference across the flow control pipe. Water flowing downward over the sensor and out through the flow control tubing was expelled onto the surface water of the main tank at roughly the same level as the standpipe outlet. (The idea was to prevent rhythmic dripping effects from being echoed back into the control pipe by surface tension forces). Temperature data was collected until the sensor tip was exposed to air, at which point power was shut off to prevent over-heating of the thermistor under conditions of poorer thermal dissipation.

Temperature difference T_S-T_F is plotted versus standpipe velocity in Figure 53. The null-points are clearly shown for the higher velocities and higher power levels but become increasing indistinct at lower velocities as expected from the CFD model. Considerable variability can be observed between measurement runs, sufficient to invalidate the method; the reasons for this are discussed in the next two sections. In Figure 53, 'double maxima' occur in eight out of ten traces. It would seem that the five-minute heating period prior to the commencement of flow was enough to create thermal stratification in the vertical water column above the sensor by almost 1°C above the tank temperature. This warm slug of water falling over the sensor overwhelmed the local heat field and generated a temperature maxima of its own that could easily be confused with the signal of interest. The 'double peaks' in each trace correspond to the arrival of the thermocline at the sensor, creating a 'step' in the background fluid temperature. This forces a step in the sensor temperature as the controller attempts to maintain a constant heat output.

7.1.6 Reducing thermal background temperatures

To overcome the impact of standpipe stratification on the measurements above the sensor the system was reconfigured to keep the sensor powered off until falling flow began; this ensured that no residual heat field was created. To break up natural stratification, water was circulated from the main tank to the top of the water column before measurements began. As the still-water temperature T_S was no longer available directly, an artificial temperature roughly equal to the heated temperature sensor at the slowest recorded flow rate was used as a substitute for T_S. The latter is used simply to extract the large common-mode background temperature from the readings so this value was deemed to be acceptable.

These measures rid the system of the 'thermocline hump' but variability in the

flow velocity corresponding to the temperature minima still remained.

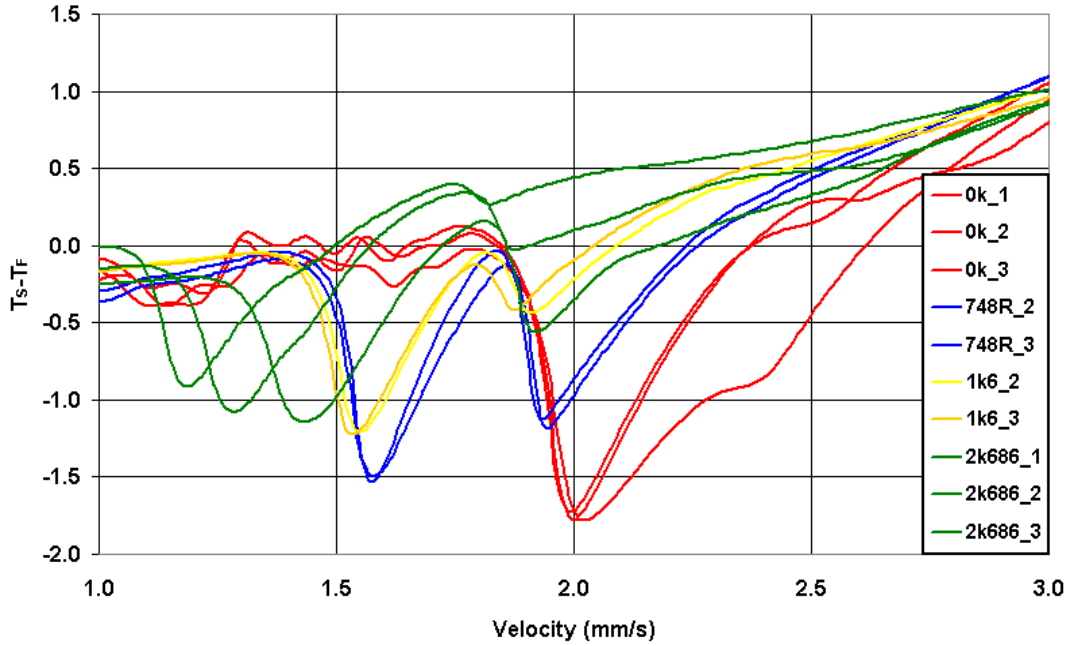

Figure 53 Temperature difference signals T_S-T_F versus velocity for four different power levels. Note that data recording actually begins at *t=0* on the right-hand side of the plot (off-scale) when flow is at a maximum. The null-points are clearly shown for the higher velocities and higher power levels, but become increasingly indistinct at lower flows. The extra peaks at higher velocities around 1.8 mm/s result from initial thermal stratification of the water column above the sensor and correspond to a shift in the background temperature as the thermocline passes over the sensor. Legend colours are: Red: 97 mW, Blue: 77 mW, Yellow: 62 mW and Green: 48 mW

7.1.7 Flow instability

At the 48mW power level (green trace in Figure 53) minima for each of the three runs occur at 1.13, 1.23 and 1.37 mm/s, creating an unacceptable measurement uncertainty in determining flow velocity. To find the cause of this measurement uncertainty, 11 runs were made with the sensor dissipating the maximum power of 97 mW to produce the strongest 'peak' at the stagnation temperature. The common-mode temperature T_S has been treated merely as a numerical offset in Figure 54, forcing the minimum temperature difference to be equal to –1.5°C on the temperature differential axis. This shows more clearly just how badly the peak scatter is along the velocity axis, ranging from 1.6 mm/s to 2.7 mm/s.

Ultimately, the simplest explanation of why experimental results were so poor was the obvious explanation; the flow rate ***was*** changing between each run. 'Pulling the plug' to start each test run, as described in Section 7.1.5, resulted in minute changes of the position of the outlet pipe with respect to the water surface. Repeated runs using the nine level sensors as an independent measure of flow rate vindicated the result generated by the

flow sensor itself; flow rates varied significantly from one run to the next. The cause was traced to the 'shape' of the water outflow stream from the Hagen-Poisuelle flow pipe onto the surface of the water body in the main tank. This varied minutely each run as the plug-pulling operations described in section 7.1.5 perturbed the height of the outlet above the water surface. It was not until this outflow was forced to exhaust ***under*** water and left untouched that flow in the test rig could be assumed to be the same run after run. Surface tension effects had still been operating, albeit without the rhythmic oscillations induced by dripping outflows. Once this obstacle had been cleared, experimental data aligned with the CFD and engineering models, and the paper at the end of this Chapter could be completed.

7.1.8 Plume stability

The constant power data of Figure 54 was used to further examine the stability of the thermal plume as flow slows from a maximum to a minimum as water runs out of the standpipe into the main tank. The T_S-T_F minima shown in the constant power plots of Figure 54 have been numerically forced to a nominal velocity of 2.13 mm/s by simply cutting and moving columns of data in the spreadsheet to align the minima; the result is shown in Figure 55. It can be seen that the temperature slope of the inverted thermal plume is less stable than the buoyant thermal plume. At the stagnation velocity, the temperature of the heated thermistor T_F reaches its warmest with respect to the still water temperature T_S, resulting in a T_S-T_F minimum. The water around the thermistor tip is not moving and heats up to almost 1.5° above the still water temperature condition T_S. Under still-water conditions, the buoyant thermal plume essentially cools the thermistor tip below the stagnation temperature by thrusting the local heat field up into a region several centimetres above the sensor.

The situation on either side of the stagnation point is this. At flow velocities higher than the stagnation velocity, the thermal plume is washed below the sensor tip and is inherently unstable, like a balloon held underwater with a stick. At flow velocities slower than the stagnation velocity, the thermal plume rises in a much more stable fashion above the sensor tip, like a helium balloon in still air on the end of a string. Figure 55 shows this clearly; the sensor temperature changes rapidly from unstable at higher velocities to the right of the stagnation point to stable at lower velocities to the left of the stagnation point.

These findings suggest that the sensor control mechanism should 'seek the peak' from a higher power level by first suppressing the more stable buoyant plume until the stagnation point is reached.

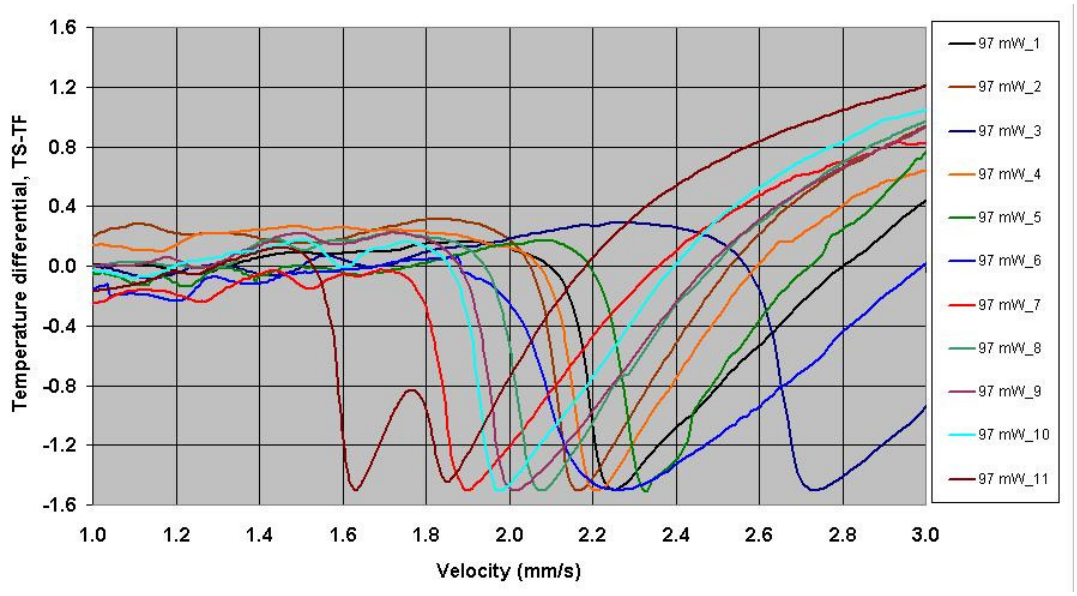

Figure 54. Flow response at constant power (97 mW) with normalised T_S; this small offset change is justified as T_S is arbitrarily chosen anyway with this method. If the theory was correct and the calibration rig working as expected all of these 'minima' should occur at the same velocity at this fixed power level. This is clearly not the case here, although many more weeks were to pass before the cause of this flow instability was discovered.

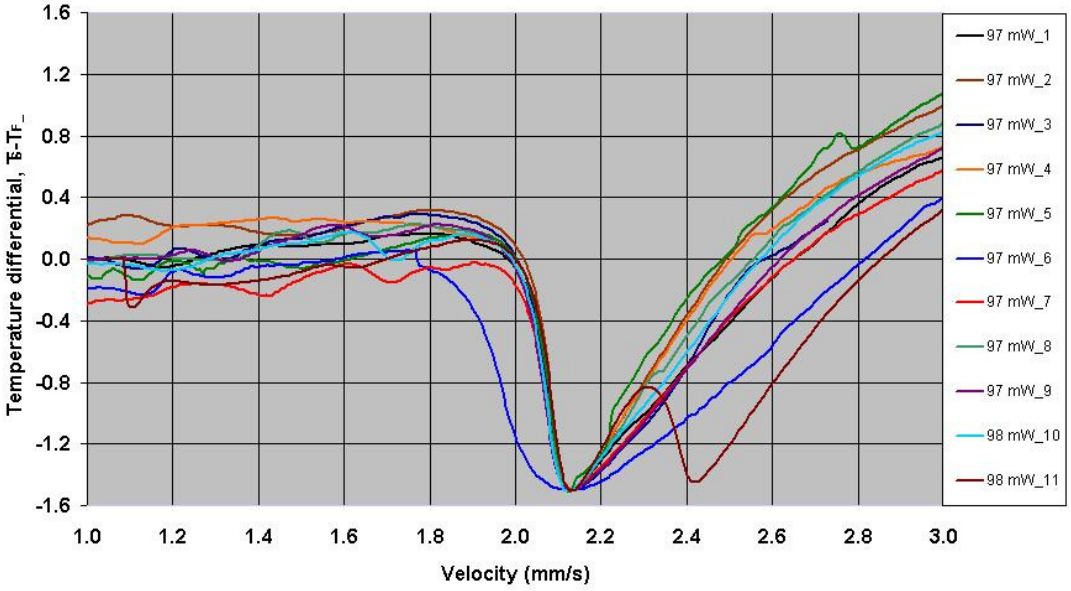

Figure 55. Flow response at constant power (97 mW) with 'normalised' TS and velocity. This allows the 'shape' of the response to be seen over 11 consecutive runs. These plots suggest that the inverted thermal plume is less stable when forced below the thermistor tip by overwhelming flows (to the right of the null-point) in comparison to more stable buoyant plume above the sensor tip (to the left of the null-point). The reasons for the double minima in run 11 (brown trace) and blurred minima in run 3 (dark blue trace) are unknown.

Paper
Skinner, A.J. and Lambert, M.F. (2009). 'A null-buoyancy thermal flow meter: Application to the measurement of the hydraulic conductivity of soils.' IEEE Sensors, in submission, August 2009.

Chapter 8. Conclusions and Future Work

This thesis has sought to demonstrate that simple sensors can make complex measurements, provided only that ingenuity and time are available in abundance. This abundance of time is rarely available in the commercial sensor development process and is likely disappearing from the academic world as well.

Applications involving the measurement of very slow flows in environmental engineering are also abundant, as this thesis has sought to demonstrate through five journal papers ranging across measurements in lakes, rivers, crops and landscape processes.

Very slow flows within large water bodies were observed indirectly by using highly matched temperature sensors arrayed in smart-sensor strings hanging vertically on a single cable through a temperature-stratified water column. Deployment of these 'thermistor strings' in a dozen different reservoirs brought to light hydrodynamic events whose magnitude and spatial effects provided evidence of other very slow flows. For example, a cold-water in-rush caused by a storm over the catchment led to a 'short-circuiting' of the Happy Valley Reservoir in South Australia; this 'gravity current' under-flowed the warmer less-dense main water body (Figure 60, Appendix A). Other events at other reservoirs captured seiching and standing waves following wind and flood events.

A different type of density stratification can be found in river estuaries where denser salt water, driven by tidal or river rise, flows under fresh water river outflows, provided river and seawater temperatures are roughly equal. The extension of the charge-balance ADC from the thermistor temperature sensors to four-electrode conductivity and platinum resistance thermometers makes possible the future development of smart sensor strings for detecting both temperature and salinity stratification. These sensors need to solve manufacturing issues with the existing smart sensor strings shown in Figure 21; although the sensor elements are inexpensive, hand assembly of the cable and waterproof jackets is expensive and field interchangeability difficult. Furthermore, sensors cannot be kept in stock as they have to be fully assembled into customized waterproof strings before immersion in the calibration bath. New work on density strings must solve three problems, shown schematically in **Error! Reference source not found.**. If sensors are not hard-wired into sensor cables then a magnetic modem needs to be developed to transfer power, measurement commands and data. Bio-film build up on the EC sensor will cause long-term drift and may be combated by the use of ultraviolet light-emitting diodes at the germicidal wavelength of 254.7-nm wavelength. Finally, water samples must be

exchanged between the main water body and the measurement cell; this thesis has shown that simple self-heating thermistors can act as slow thermal pumps.

These salinity sensors can be further developed for use in seepage meters to quantify salt loads entering fresh water rivers from saline groundwater sources. The challenge here will be to build a bi-directional seepage meter capable of measuring flows in both directions between surface and ground waters and having sufficient dynamic range to cover the five orders of magnitude changes found in nature. Investigation of downward flows using a null-buoyancy flow meter resulted in particularly poor dynamic range despite demonstrating a sensor of great simplicity.

These integrated platinum-on-ceramic EC sensors have been inexpensively interfaced to data logging systems in order to record toxic salt fluxes in soils. Field experiments have been set up at Oxford Landing to capture such events but have been confounded by the Australian drought that has lingered on since 2006. Rainfall events over the experimental site have been so light and infrequent since installation that no wetting fronts have occurred despite installation during the Australian (wet) winter period. Irrigation systems are currently off, as the vines in the experimental site are dormant. One must wait…

The second half of the thesis pursued the design and use of warm thermistor sensors. Plant water status monitoring based on thermal diffusion techniques has yet to be demonstrated as an irrigation-scheduling tool on a growing crop although a simple laboratory experiment showed the concept to be promising. Warm thermistor technology was also applied to the design of very slow flow meters operating below the known 3 mm/s limit in the buoyant flow region of operation where early researchers had faltered. Flow meters based upon upward flow (seepage meters) and downward flows (permeameters) have been described, with basic principles investigated in the laboratory and through computer modeling. Creating working instruments in these fields is beyond the scope of this PhD process, as demonstrated by the extent of the work needed to commercialize simple temperature sensors for stratification measurements in reservoirs.

At the heart of these thermal diffusion and slow flow measurements is an analog control circuit able to drive a thermistor at power levels over a range of 1:1000 while simultaneously monitoring thermistor temperature to high precision. A single self-referencing thermistor sensor has been shown to be useful in measuring ambient temperature and flow speed simply by switching power levels. These flow sensors represent a departure from the standard constant over-temperature operation commonly employed by other researchers in creating flow meters for higher flow rates. Constant heat

output simplifies calibration to measurements made against a single temperature standard. The method needs to be tested in biologically active water bodies to determine if it copes better with bio-film build-up on the sensor than constant-temperature devices whose external heat fields fall away as insulating films build up.

One of the significant challenges in this thesis was to develop calibration methods to generate the very slow flows of interest needed to test these slow flow sensors. That such measurement effort was warranted was indicated by CFD modeling that pointed the way; there was no need to choose between models or measurements – both worked hand-in-hand to achieve a workable instrument. CFD models showed that a self-heated thermistor creates a real upward flow of its own of about 1.35 mm/s at a 40-mW power output. This led directly to the concept of a non-mechanical null-buoyancy method of determining flow using a single thermistor with variable power control useful in automating permeameters for measuring very slow flows into the soil surface. The familiar fluid mechanics problem of flow stagnation proved to be a bonus. If a buoyant thermal up-thrust could balance a downward fluid flux then such a stagnation point might logically occur. This proved to be the case in the CFD model, and power dissipation could be adjusted using the existing sensor control mechanisms to achieve this stagnation point, indicated by an increase in temperature within a sensor having controllable power and measurable thermistor temperature. Proving this in the laboratory was simplified because the mechanisms for generating the necessary slow flow rates had already been worked out, albeit for flows in a downward direction. This new work on upward flows did, however, highlight the variability in the calibration apparatus between one test run and the next. Ultimately, this was traced to the air-water interface at the outlet of the Hagen-Poiseuille flow control pipe. Decent results could only be obtained once this outlet was submersed and left undisturbed just below the surface of the main tank, negating surface tension effects. No such problems had occurred in the seepage meter calibration apparatus, where (fortuitously) water-to-water connection along the flow control pipe was inherent in the design.

Experimental proof-of-method showed that the null-buoyancy flow technique method was ultimately still subject to background ambient fluctuations acting at a distance. This came as a surprise but shouldn't have; this very problem plagued all early efforts to build warm thermistor flow meters. Further design and experimental work beyond this thesis will need to focus on finding ways to minimize the effects of background temperature perturbations without having to create the sort of isothermal

conditions almost impossible to achieve under field conditions; the new instrument must learn to cope.

A set of carefully controlled measurements at a single power level showed that the null-buoyancy flow meter generated heat fields on either side of the stagnation flow rate that were markedly different. Specifically, heat fields forced below the sensor tip by fluid fluxes were significantly less stable than thermal plumes above the sensor where buoyancy flows dominated fluid flow. This suggests a need for future work to develop drive circuitry to first create an upwardly-buoyant plume before backing off the power level through the stable flow range until the null-point is detected just before the plume is driven below the sensor tip into the unstable region.

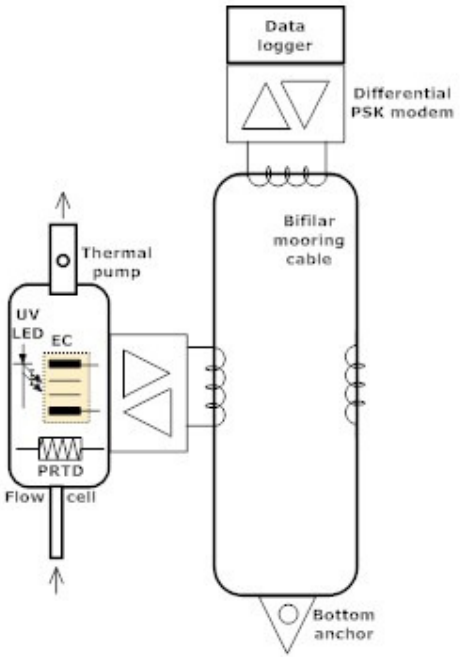

Figure 56 Future work: In concept, multiple doughnut-shaped salinity and temperature sensors for monitoring density stratification in estuarine river environments slide down the (looped and electrically insulated) mooring cable to the required depth. Such sensors can be pre-calibrated without first having to be assembled into waterproof strings. The mooring cable forms a single winding for the differential phase shift keyed (PSK) magnetic modem that transfers power to multiple sensors and allows bi-directional flow of measurement commands and data. Bio-film build up is ameliorated by exposure of the electrodes to UV LED radiation inside the measurement cell. Water is pumped through the cell using a thermal pump between measurement cycles.

The relationship between power and flow rate that was determined experimentally using the null-buoyancy flow meter confirmed the square-law relationship between power and flow indicated by CFD and engineering models. This same square-law limited the operating flow range of the sensor under experimental conditions to even less than the 10:1 flow range suggested by the modeling; increasing the sensitivity at low power levels

is expected to improve this only slightly. Perhaps the true use of this flow meter principle will be in constant-flow control systems that operate at higher power levels where the null-buoyancy peak is most pronounced. The null-buoyancy sensor is, after all, quite sensitive within its narrow operating flow range, much as a ‘lock-in’ amplifier in electronic control circuits is used to reject all perturbations outside a very specific frequency range.

Overall, complex environmental slow-flow measurements have been demonstrated using simple circuits based around low-cost sensor elements. If new instruments do indeed drive new science, then this body of work can provide the seeds for the development of environmental measurement tools useful in gaining an understanding of the natural environment upon which all life on this planet depends for support.

Chapter 9. References

1) Amoozegar, A. (1989). 'A compact constant-head permeameter for measuring saturated hydraulic conductivity of the vadose zone.' Soil Science Society of America Journal. Sept.-Oct. 1989, 53:1536-1361
2) Analog Devices, (1992). 'AD652 Monolithic Synchronous Voltage-to-Frequency Converter'. Data converter reference manual Volume II, pp. 3-27.
3) Angulo-Jaramillo, R., Moreno, F., Clothier, B.E., Thony, J.L., Vachaud, G., Fernandez-Boy, E. and Cayuela, J.A. (1997). 'Seasonal variation of hydraulic properties of soils measured using a tension disk infiltrometer'. Soil Sci. Soc. Am. J. 61, pp. 27–32
4) Angulo-Jaramillo, R.,Vandervaere, J-P, Roulier, S. Thony, J-L., Gaudet, J-P. and Vauclin, M. (2000). 'Field measurement of soil surface hydraulic properties by disc and ring infiltrometers: A review and recent developments'. Soil and Tillage Research 55 (2000) 1-29
5) Ankeny, M.D., Kaspar, T.C. and Horton, R. (1989). 'Automated tension infiltrometer' US Patent Number 4,884,436
6) Ankeny, M.D., Kaspar, T.C. and Horton, R. (1991). 'Simple field method for determining unsaturated hydraulic conductivity'. Soil Sci. Soc. Am. J. 52, pp. 467–470.
7) Antennucci, J.P. and Imberger, J. (2001). 'On internal waves near the high-frequency limit in an enclosed basin'. Journal of Geophysical Research, Vol. 106, No. C10, pp 22, 465-22,474, October 2001
8) Auerbach, F.J., Meiendres, G., Mueller, R. and Scheller, G.J.E. (1994). 'Simulation of the thermal behaviour of thermal flow sensors by equivalent electrical circuits.' Sensors and Actuators, A41-A42, 275-278.
9) Australian Bureau of Statistics (1992). Yearbook, January 1992, Chapter 15, 'Agriculture'.
10) Baier, P. W., Bonnet, K. F. (1978). 'PTC-resistor probe for the measurement of the instantaneous fuel consumption in motor vehicles.' Flow Measurement of Fluid, 455-459.
11) Baker, J.M. and van Bavel, C.H.M. (1987). 'Measurement of mass flow of water in the stems of herbaceous plants'. Plant, Cell and Environment. Vol. 10, p. 777-782.

12) Baker, R.C. (2000). 'Flow measurement handbook: Industrial designs, operating principles, performance and applications' Cambridge University Press. ISBN 0-521-48010-8

13) Barrett, D.J., Hatton, T.J., Ash, J.E. and Ball, M.C. (1995). 'Evaluation of the heat pulse velocity technique for measurement of sap flow in rainforest and eucalypt forest species of south-eastern Australia'. Plant, cell and environment, vol. 18, No.4, pp. 463-469

14) Batchelor, G.K. (1959). 'Small scale variations of convected quantities like temperature in turbulent fluids.' Journal of Fluid Mechanics, 5, 113-139.

15) Bond, W.J. and Hutchinson, P.A. (2006). 'Principles, Implementation and Operation of the tube tensiometer drainage meter'. A report for the Grain Research and Development Corporation. CSIRO Land and Water Science Report 18/06, June 2006

16) Brand, A.,Müller, B., Wuest, A., Dinkel, C., Revsbech, N. P., Nielsen, L.P., Pederesen, O., Damgaard, L. R., Larsen, L. H. and Wehrli, B. (2007). 'Microsensor for in situ flow measurements in benthic boundary layers at submillimeter resolution with extremely slow flow.' Limnology and Oceanography: Methods 5, 185-191

17) Bremhorst, K., Graham, L.J.W. (1990). 'A fully compensated hot/cold wire anemometer system for unsteady flow velocity and temperature measurements.' Measurement Science and Technology, 1, 425-430.

18) Briggs-Smith, M., Piscitelli S. and Livrea A. (1981). 'Pulse thermistor technique for measuring very low liquid flow rates.' Review of Scientific Instruments, 52(10), 1565-1568.

19) Brumley, B., Murphy, P.J. (1977). 'Turbulence measurements in a lake.' Scientific Press, , 337-344.

20) Brundritt, J. K. (1971). 'A device for determining velocity of flow near the substrate.' Limnology and Oceanography, 16, 120 - 123.

21) Caldwell, D.R., Wilcox, S.D. and Matsler, M. (1975). 'A freely falling probe for small-scale temperature gradients.' Limnology and Oceanography, 20, 1034-1042.

22) Canali, C., Catellani, A., Morten, B., Prudenziati, M., Stacchietti, R. and Taroni, A. (1981). 'Self-heated element, solid-state, flow sensors.' Proceedings of ISATA, Stockholm, 68, .

23) Catellani, C., Stacchietti, R., Taroni, A. and Canali, C. (1982). 'Dynamic behaviour and stability of thermistor air flowmeter.' Sensors and Actuators, 3, 195-202.

24) Catellani, C., Stacchietti, R., Taroni, A. and Canali, C. (1982). 'Performance and temperature stability of an air mass flowmeter based on a self-heated thermistor.' Sensors and Actuators, 3, 23-30.

25) Cimbala, M. G., 'Binary Logarithms and their uses'. Professional Firmware Inc. mcimbala@isrv.com. Private web site.

26) Clark, L.J. (2004). 'Changes in properties of vineyard red-brown earths under long-term drip irrigation, combined with varying water qualities and gypsum application rates'. PhD Thesis: University of Adelaide, South Australia

27) Clift, R., Grace, J. and Weber, M. E. (1978). 'Bubbles, Drops and Particles'. Dover Publications. ISBN: 9780486445809

28) Clothier, B.E., Kirkham, M.B. and McLean, J.E. (1992). 'In situ measurement of the effective transport volume for solute moving through soil'. Soil Sci. Soc. Am. J. 56, pp. 733–736.

29) Clothier, B. E. and White, I. (1981) 'Measurement of Sorptivity and Soil Water Diffusivity in the Field' Soil Sci. Soc. Am. J., Mar 1981; 45:241-245.

30) Collis, D. C., Williams, M. J. (1959). 'Two-dimensional convection for heated wires at low Reynolds numbers.' Journal of Fluid Mechanics, 6, 357-384.

31) Compte-Bellot, G. (1976). 'Hot-wire anemometry.' Annual Review of Fluid Mechanics, 8, 209-231.

32) Cook, F.J. and Broeren, A. (1994). 'Six methods for determining sorptivity and hydraulic conductivity with disc permeameters'. Soil Sci. 157, pp. 2–11.

33) Cook, F.J., Jayawardane, N.S., Rassam, D.W., Christen, E.W., Hornbuckle, J.W., Stirzaker, R.J., Bristow, K.L. and Biswas, T.K. (2006) 'The state of measuring, diagnosing, ameliorating and managing solute effects in irrigated systems'. Technical Report No. 04/06, CRC for Irrigation Futures (Australia), October 2006

34) Cook, R.R. (1994). 'Measurement uncertainty.' Electrical Engineering Congress.

35) Coulson, J. M. and Richardson, J. F. (1978). 'Chemical Engineering' Third Ed. p203. 1978. ISBN 0-08-021015-5. Permagon

36) Dennis, J.E., Gay, D.M., and Welsch, R.E. (1981). 'An adaptive non-linear least-squares algorithm'. ACM Transactions on Mathematical Software Sept 1981. 7, 3

37) Dillon, T. M., Powell, T. M. (1976). 'Low-frequency turbulence spectra in the mixed layer of Lake Tahoe, California-Nevada.' Journal of Geophysics Research, 81, 6421-6427.

38) Dostert, K. (1982). 'Applications of self-heated PTC thermistors to flow and quantity of heat measurement.' Sensors and Actuators, 3, 159-167.

39) Douglas, J.F. (1986). 'Fluid Mechanics' 2nd ed. p311, ISBN 0-582-98861-6, Longman

40) Edwards,W.R.N.,Jarvis,P.G.,Landsberg, J. J. and Talbot, H. (1986) 'A dynamic model for studying flow of water in single trees' Tree Physiology 1, 309-324 (1986). Heron Publishing-Victoria, Canada.

41) Edwards, W.R.N., Becker, P. and Èermák, J. (1997). 'A unified nomenclature for sap flow measurements'. Tree Physiology 1997 17(1):65-67

42) Falivene, S. (2008). 'Soil Solution Monitoring in Australia'. CRC for Irrigation Futures (Australia). Irrigation Matters Series No. 04/08, November 2008

43) Forstner, H. and Rutzler, K. (1969). 'Two temperature compensated current meters for use in marine ecology.' Journal Marine Resources, 27, 263 - 271.

44) Forte, J., Victoria, L. and Ibanez, J. A. (1990). Review of Scientific Instruments, 61, 1123.

45) Fowlis, W.W. (1970). 'Techniques and apparatus for the fast and accurate measurement of fluid temperature and flow speed fields.' Review of Scientific Instruments, 41, 570-576.

46) Fujita, H., Ohhashi, T., Asakura, M. and Watanabe, K. (1995). 'A thermistor anemometer for low-flow measurements.' IEEE Transactions of Instrumentation and Measurement, 44(3), 779-781.

47) Furness, R.A., (1991). 'The Principles of Flowmeter Selection.' Water, October, 26-30.

48) Gee, G.W., Ward, A.L., Caldwell, T.G. and Ritter, J.C. (2002). 'A vadose zone water fluxmeter with divergence control', Water Resour. Res., 38(8), 1141

49) Goldstine, H.H. (1977). 'A History of Numerical Analysis'. Springer-Verlag, New York.

50) Grahn, A.R., Paul, M.H. and Wessel, H.U. (1968). 'Design and evaluation of a new linear thermistor velocity probe.' Journal of Applied Physiology, 24, 236-246.

51) Granier, A. (1985). 'Une nouvelle méthode pour la mesure du flux de sève brute dans le tronc des arbres'. Annales des Sciences Forestières. Vol. 32, p 193-200

52) Gullo, M.A., Lo and Salleo, S. (1991). 'Three different methods of measuring xylem cavitation and embolism: a comparison'. Annals of Botany, Vol. 67, p 417-424

53) Hamblin, P.F. and Kuenel, R. (1980). 'An evaluation of an unattended current and temperature profiler for deep lakes.' Limnology and Oceanography, 25, 1128-1141.

54) Hart, D.D., Clark, B.D. and Jasentuliyana, A. (1996). 'Fine-scale measurement of benthic flow environments inhabited by stream invertebrates.' Limnology and Oceanography, 41(2), 297-308.

55) Hinze, J.O. (1975). 'Turbulence'. McGraw-Hill series in mechanical engineering, ISBN 0 070 29037 7

56) Helfter, C., Windt, C.W., van As, H., Mencuccini, M. and Hand, D.P. (2007). 'Lasers for non-invasive monitoring of sap flow in trees'. SPIE – The International Society for Optical Engineering. 10.1117/2.1200703.0653

57) Huber, B. (1923). 'Transpiration in verschiedener Stammhöhe *I. Sequoia gigantea*'. Zeitschr. f. Bot. 15:465-501

58) Hutchinson, P.A. and Bond, W.J. (2001). 'Routine measurement of the soil water potential gradient near saturation using a pair of tube tensiometers', Australian Journal of Soil Science Vol. 39, pp. 1147-1156.

59) Imberger, J. (1991). 'Instrumentation development for lake mixing investigations.' Water, October 17-18.

60) Imberger, J. (1998). 'Flux Paths in a Stratified Lake'. Coastal and Estuarine Studies. American Geophysical Union, Issue 54, pages 1-18. ISSN 0938-0949

61) Imberger J. and Ivey G.N. (1991). 'On the Nature of Turbulence in a Stratified Fluid. Part II: Application to Lakes' Journal of Physical Oceanography. Volume 21, Issue 5 pp. 659–680

62) Inoue, M. Higashi, N., Yamazaki, S., Inosako, K. and Mori, Y. (2004). 'Effect of salt concentration on measurement of soil water content using various soil moisture probes based on dielectric constant' 2004 ASA-CSSA-SSSA International Annual Meetings, Seattle, Oct.31-Nov.4.

63) Inoue, M., Ould Ahmed. B.A., Saito, T. and Irshad, M. (2008). 'Comparison of twelve dielectric moisture probes for soil water measurement under saline conditions'. (Technical report). American Journal of Environmental Sciences 4.4 (August 2008): p367(6)

64) Inoue, M., Simunek, J., Hopmans, J.W. and Clausnitzer, V. (1998). 'In-situ estimation of soil hydraulic functions using a multistep soil-water extraction technique'. Water Resources Research, Vol. 34, pp. 1035-1050.

65) Jolly, I.D., Dowling, T.I., Zhang, L. Williamson, D.R. and Walker, G.R. (1997). 'Water and salt balances of the catchments of the Murray-Darling Basin'. CSIRO Technical Report 37/97, November 1997

66) Kanwisher, J., Lawson, K. (1975). 'Electromagnetic flow sensors.' Limnology and Oceanography, 20, 174 - 182.

67) King, L.V. (1914). 'On the Convection of Heat from Small Cylinders in a Stream of Fluid: Determination of the Convection Constants of Small Platinum Wires with Applications to Hot-Wire Anemometry' The Royal Society.

68) Klepper, B., Browning, V.D. and Taylor, H.M. (1971). 'Stem diameter in relation to plant water status'. Plant physiology. Vol. 48, 683-685

69) Kodesova, R., Ordway, S.e. Gribb, M.M. and Simunek, J. (1999). 'Estimation of soil hydraulic properties with the cone permeameter: Field studies'. Soil Science, Vol. 164, pp. 527-541.

70) Kung, R., Buzyna, G and Pfeffer, R. (1987). 'Velocity and temperature measurement with thermistor anemometers in a thermally stratified rotating fluid.' Journal of Physics E: Scientific Instruments, 20, 461-467.

71) LaBarbera, M. and Vogel, S. (1976). 'An inexpensive thermistor flowmeter for aquatic biology.' Limnology and Oceanography, 21, 750-756.

72) Lee, D.R. (1977). 'A Device for Measuring Seepage Flux in Lakes and Estuaries' Limnology and Oceanography, Vol. 22, No. 1, Jan. 1977, pp. 140-147

73) Lammerink, T.S.J, Tas, N.R., Elwenspoek, M. and Fluitman, J.H.J. (1993). 'Micro-liquid flow sensor.' Sensors and Actuators, A37-A38, 45-50.

74) Lang, A.R.G., Leuning, R. (1981). 'New omnidirectional anemometer with no moving parts.' Boundary-Layer Meteorology, 20, 445-457.

75) Laub, J.H. (1947) 'An electric flowmeter' Electrical Eng. 66 1216-9

76) Laub, J.H. (1956) 'Thermal flowmeter' US Patent 2 729 976

77) Laub, J.H. (1957) 'Measuring mass flow with the boundary-layer flowmeter' Control Eng. 4 March 112-7

78) LaZerte, B. D. (1978). 'The planktonic diatom ecology, internal seiches and hypolimnetic turbulence of Frains Lake, Michigan.' PhD Thesis.

79) Lemckert C., Antenucci, J. Saggio, A. and Imberger J. (2004). 'Physical properties of turbulent benthic boundary layers generated by internal waves'. ASCE, Journal of Hydraulic Engineering Volume 130, Issue 1, pp. 58-69, Jan 2004

80) Lemckert C. and Imberger J. (1993). 'Energetic Bubble Plumes in Arbitrary Stratification.' Journal of Hydrological Engineering. Volume 119, Issue 6, pp. 680-703, June 1993

81) Lemckert C. and Imberger J. (1998). 'Turbulent benthic boundary layer mixing events in fresh water lakes.' Coastal And Estuarine Studies, 1998 Issue 54, pp 503-516 - AGU American Geophysical Union

82) Lemmin, U., Schurter, M., Imboden, D. M. and Joller, T. (1985). 'An instrument for measuring small bottom currents in lakes.' Limnology and Oceanography, 30, 1116-1122.

83) Leonard, L.A., Luther, M.E. (1995). 'Flow hydrodynamics in tidal marsh canopies.' Limnology and Oceanography, 40(8), 1474-1484.

84) Lewis D.M., Elliott J.A., Brookes J.D., Irish A.E., Lambert M.F. and Reynolds C.S. (2003). 'Modelling the effects of artificial mixing and copper sulphate dosing on phytoplankton in an Australian reservoir'. Lakes & Reservoirs: Research & Management Volume 8 Issue 1, Pages 31 – 40, 30th April 2003

85) Litaor, M.I. (1988). 'Review of soil solution samplers'. Water Resources Research, Volume 24, Issue 5, p. 727-733

86) Lockyer, R. (1996). 'A sonic anemometer for general meteorology.' Sensors, May, 43435.

87) Lomas, C.G. (1986). 'Fundamentals of Hot Wire Anemometry.' Cambridge University Press.

88) Lorke A., Umlauf L., Jonas T. and Wüest A. (2002). 'Dynamics of Turbulence in Low-Speed Oscillating Bottom-Boundary Layers of Stratified Basins.' Journal of Environmental Fluid Mechanics Volume 2, Number 4 Pages 291-313 December, 2002 ISSN 1567-7419

89) Loveys, B., McCarthy, M., Jones, H.G., Theobold, J. and Skinner, A.J. (2005). 'When to water? Assessment of plant-based measurements to indicate irrigation requirements'. CSIRO Final Report to Australian Grape and Wine Research and Development Corporation, Project Number CSP02/02, CSIRO Plant Industry, September 2005

90) Luketina, D.A., Imberger, J. (1998). 'Determining turbulent kinetic energy dissipation from Batchelor curve fitting.' Journal of Atmospheric and Oceanic Technology.

91) MacIntyre, S. (1981). 'Stratification and mixing in shallow tropical African lakes.' PhD Thesis.

92) MacIntyre, S. (1986). 'A flow-measuring system for use in small lakes.' Limnology and Oceanography, 31(4), 900-906.

93) MacIntyre, S., Flynn, K., Jellison, R. and Romero, J. (1999). 'Boundary mixing and nutrient fluxes in Mono Lake, California.' Limnology and Oceanography, 44(3), 512-529.

94) Meyer, W.S. and Green, G.C. (1980). 'Water Use by Wheat and Plant Indicators of Available Soil Water.' Agron J.1980; 72: 253-257

95) Meyer, W.S. and Green, G.C. (1981) 'Plant indicators of wheat and soybean crop water stress.' Journal Irrigation Science. Volume 2, Number 3 / September, 1981

96) Meyer, W.S., Dugas, W.A., Barrs, H.D., Smith, R.C.G. and Fleetwood, R.J. (1988). 'Effects of soil type on soybean crop water use in weighing lysimeters'

97) Meyer, W.S. and Green, G.C. (1990). 'Effects of soil type on soybean crop water use in weighing lysimeters'. Volume 11, Number 2 / April, 1990 pp.69-75

98) Meyer, W.S. and Green, G.C. (1999) 'Growth and ground water uptake responses of lucerne to changes in groundwater levels and salinity: lysimeter, isotope and modelling studies.' Agricultural Water Management. Volume 39, Issues 2-3, 25 February 1999, Pages 265-282

99) Miaschi, B and Rasmussen K. E. (1974). 'Neoprene vulcanization for waterproofing of underwater cable systems' 10/1974
http://adsabs.harvard.edu/abs/1974STIN...7526276M

100) Microchip Corporation (1997). 'Application Note AN660: Floating Point Routines'. Testa, F.J.

101) Molina, C., Victoria, L. and Ibanez, J.A. (1994). 'Measurement of volume flow through a microporous membrane by a NTC thermistor miniature bead.' Review of Scientific Instruments, 65(8), 2726-2730.

102) Morten, B., Prudenziati, M., Taroni, A. and Zanarini, G. (1976). 'Experimental results on dynamic behaviour of thermistor flowmeters.' IEEE Transactions of Instrumentation and Measurement, IM-25(3), 232 - 234.

103) Nadler, A. (2005). 'Methodologies and the practical aspects of the bulk soil EC-soil solution EC relations'. Advances in Agronomy, Volume 88, Elsevier 0065-2113/05

104) National Semiconductor Corporation (1997). 'Super Matched Bipolar Transistor Pair Sets New Standards for Drift and Noise.' Application Note 222, July 1997

105) Okamoto, K., Ohhashi, T., Asakura, M. and Watanabe, K. (1994). 'A digital anemometer.' IEEE Transactions of Instrumentation and Measurement, 43(2), 116-120.

106) Olin, J.G. (1993). 'An Engineering Tutorial: Thermal Mass Flowmeters.' Intech Engineer's Notebook, Aug, 37-41.

107) Paige, R, and Koenig, S. (1982). 'Finite differencing of computable expressions'. ACM Transactions on Programming Languages and Systems, Vol. 4, No. 3, July 1982, Pages 402-454.

108) Patterson, M.R., Sebens, K.P. and Olson, R. (1991). 'In situ measurements of flow effects on promary production and dark respiration in reef corals.' Limnology and Oceanography, 36(5), 936-948.

109) Paulsen, R.J., Smith, C.F., O'Rourke, D., Wong, T.F. (2001). 'Development and evaluation of an ultrasonic ground water seepage meter' - Ground Water, Vol.39, No. 6, p 904-911, Nov/Dec 2001

110) Peňuelas, J, Filella, I., Biel, C., Serrano L. and Savé, R. (1993). 'The reflectance at the 950-970 nm region as an indicator of plant water status'. International Journal of Remote Sensing, Vol. 14, No. 10, 1887-1905

111) Perroux, K.M. and White, I. (1988). 'Designs for disc permeameters'. Soil Sci. Soc. Am. J. 52, 1205-1215.

112) Rasmussen, R. A. (1962). 'Application of thermistors to measurement in moving fluids.' Review of Scientific Instruments, 33, 38-42.

113) Riedl, R. J. and Machan, R. (1972). 'Hydrodynamic patterns in lotic intertidal sands and their bioclimatological implications.' Marine Biology, 13, 179-209.

114) Rosenberry, D.O. and Morin, R.H. (2004). 'Use of an electromagnetic seepage meter to investigate temporal variability in lake seepage.' Ground Water, Vol 41(1). p 68-77. Jan/Feb 2004

115) Roy, H., Hüttel, M. and Jørgensen, B B. (2002). 'The role of small-scale sediment topography for oxygen flux across the diffusive boundary layer'. Limnol. Oceanogr. 47: 837-847.

116) Rutherford, J. C., MacCaskill, J.B. and Williams B.L. (1993). 'Natural water temperature variations in the lower Waikato River New Zealand', New Zealand Journal of Marine and Freshwater Research, 1993: Vol 27: 71-85

117) Saggio A. and Imberger J. (2001). 'Mixing and turbulent fluxes in the metalimnion of a stratified lake.' Limnology and Oceanography, 46(2), 2001, Vol. 46; Part 2, pp 392-409 ISSN 0024-3590

118) Schrank, G., Lane, J. (1991). 'Measurement of Turbidity in Wastewater Treatment.' Water, October, 33-43.

119) SDI-12 sensor interface bus: www.sdi-12.org

120) Selker, J., Leclerq, P., Parlange, J.Y. and Steenhuis, T. (1992). 'Fingered Flow in Two Dimensions, 1. Measurement of Matric Potential.' Water Resources Research, 28(9), 2513-2521.

121) Sheldrake, T.H. 'Heat transfer and fluid flow around an axisymmetric 1C engine inlet valve.' Heat Transfer, 1995 - Wiley

122) Shuichi E., Tsujii I., Kawashima M. and Okumura, Y. (2008). 'A new method of temperature-compensation of electrical conductivity using temperature-fold dependency of fresh water'. Limnology (2008) 9:159-161. DOI 10.1007/s10201-008-0248-2

123) Skinner, A.J. and Lambert, M.F. (2006). 'Using smart sensor strings for continuous monitoring of temperature stratification in large water bodies.' IEEE Sensors, Vol. 6, No. 6, December 2006

124) Skinner, A.J. and Lambert, M.F. (2009a). 'A log-antilog analog control circuit for constant-power warm-thermistor sensors – Application to plant water status measurement.' IEEE Sensors, accepted for publication, December 2008

125) Skinner, A.J. and Lambert, M.F. (2009b). 'Evaluation of a warm-thermistor flow sensor for use in automatic seepage meters'. IEEE Sensors, accepted for publication, November 2008

126) Smettem, K.R.J. and Clothier, B.E. (1989). 'Measuring unsaturated sorptivity and hydraulic conductivity using multiple disc permeameters.' J. Soil Sci. 40, pp. 563–568.

127) Smith, D.M. and Allen, S.J. (1996). 'Measurement of sap flow in plant stems'. Journal of Experimental Botany., Vol. 47, No. 12, 1833-1844

128) Sonnenschmidt, D. and Vanselow, K.H. (1996). 'Measurement of water flow velocity by analysis of short temperature steps.' Measurement Science and Technology, 7, 1536-1539.

129) Spitzer, D. W. (2005). 'Industrial Flow Measurement', 3rd Edition 2005, ISA. ISBN 978-1-55617-871-9

130) Steinhart, J.S. and Hart, S.R. (1968). 'Calibration Curves for Thermistors'. Deep Sea Research vol. 15 p. 497 (1968)

131) Stenberg, M., Stemme, G. Kittisland, G. and Pedersen, K. (1988). 'A silicon sensor for measurement of liquid flow and thickness of fouling biofilms.' Sensors and Actuators, 13, 203-221.

132) Stirzaker, R.J., Sunassee, S. and Wilkie, J. 2004. 'Monitoring water, nitrate and salt on-farm: a comparison of methods.' Irrigation Australia 2004 conference, 11-13 May, Adelaide. CSIRO Land and Water Technical Report No. 34/04

133) Swade, D. (2000). 'The Cogwheel Brain: Charles Babbage and the quest to build the first computer'. Publisher: Little, Brown & Company, 2000 ISBN 0316648477 (EAN 9780316648479)

134) Swanson, R.H. and Whitfield, D.W.A. (1981). 'A numerical-analysis of heat pulse theory and practise'. Journal of Experimental Botany Vol. 32, p 221-239

135) Swart, N.R. and Nathan, A. (1992). 'Flow-rate microsensor modelling and optimization using SPICE.' Sensors and Actuators, 34, 109-122.

136) Taniguchi, M. and Fukuo, Y. (1993). 'Continuous Measurements of Ground-Water Seepage Using an Automatic Seepage Meter'. Ground Water GRWAAP, Vol. 31, No. 4, p 675-679, July/August 1993.

137) Thomas, C.C. (1911) 'The measurement of gases' J. Franklin Inst. Vol.61, 411-60

138) Thorpe, S.A. (1999). 'Observations of the thermal structure of a lake using a submarine'. Limnol. Oceanogr, 44(6),1999, 1575-1582

139) Turner, N.C. (1988). 'Measurement of plant water status by the pressure chamber technique'. Irrigation Science. Vol.9, p 289-308

140) Taha, S.M.R. (1994). 'Digital measurement of the mass-flow rate.' Sensors and Actuators, 45, 139-143.

141) Taroni, A. and Zanarini, G. (1975). 'Dynamic behaviour of thermistor flowmeters.' IEEE Transducers Indicators Electronic Controls Instrumentation, IECI-22(8), 391-396.

142) Taroni, A. and Zanarini, G. (1975). 'Sensitivity and response time of thermistor flowmeters.' IEEE Transactions: Industrial and Electronic Control and Instrumentation, IECI-22, 566-568.

143) Tong, Qin-Yi and Huang, Jin-Biao (1987). 'A novel CMOS flow sensor with constant chip sensor (CCT) operation.' Sensors and Actuators, 12, 44440.

144) Turner, J.S. and Kraus, E.B. (1967). 'A one-dimensional model of the seasonal thermocline.' Tellus XIX, 1.

145) Van der Wiel, A.J., Linder, C., de Rooij, N.F. and Bezinge, A. (1993). 'A liquid velocity sensor based on the hot-wire principle.' Sensors and Actuators, A37-A38, 693-697.

146) Van Oudheusden, B.W. (1990). 'Silicon thermal flow sensor with a two-dimensional direction sensitivity.' Measurement Science and Technology, 1, 565-575.

147) Van Oudheusden, B.W. (1991). 'The thermal modelling of a flow sensor based on differential convective heat transfer.' Sensors and Actuators, 29, 93-106.

148) Van Oudheusden, B.W. and Huijsing, J.H. (1990). 'An electronic wind meter based on a silicon flow sensor.' Sensors and Actuators, A21-A23, 420-424.

149) Verhoeven, H.J. and Huijsing, J.H. (1994). 'An integrated gas flow sensor with high sensitivity, low response time and a pulse-rate output.' Sensors and Actuators, A41-A42, 217-220.

150) Vogel, S. (1969). 'Low speed wind tunnels for biological investigations.' Chapter 11. In. Experiments in physiology and biochemistry, Vol. 2. G. A. Kerkut, ed. Academic Press, London.

151) White, I. and Sully, M.J. (1987). 'Macroscopic and microscopic capillary length and time scales from field infiltration'. Water Resour. Res. 23, pp. 1514–1522.

152) White, I., Sully, M.J. and Perroux, K.M. (1992). 'Measurement of surface–soil hydraulic properties: disk permeameters, tension infiltrometers, and other techniques'. In: Advances in Measurement of Soil Physical Properties: Bringing Theory into Practice Special Publication no. 30 SSSA, Madison, WI, pp. 69–103.

153) Wooding, R.A. (1968). 'Steady infiltration from a shallow circular pond'. Water Resour. Res. 4, pp. 1259–1273

154) Wüest A. and Lorke A. (2003). 'Small-Scale Hydrodynamics In Lakes'. Annual Review of Fluid Mechanics Vol. 35: 373-412

155) Wüest A. and Lorke, A. (2009). 'Small-Scale Turbulence and Mixing: Energy Fluxes in Stratified Lakes.' In: Gene E. Likens, (Editor) Encyclopedia of Inland Waters, Vol. 1, 628-635 Oxford: Elsevier

156) Yang, C., Kummel, M. and Soeberg, H. (1988). 'A self-heated thermistor flowmeter for small liquid flow in microchannels.' Sensors and Actuators, 15, 51-62.

157) Yang, C. and Soeberg, H. (1992). 'Monolithic flow sensor for measuring milliliter per minute liquid flow.' Sensors and Actuators, 33, 143-153.

158) YSI Precision Thermistor Thermometry (1993). 'Application Note TD002'. Zurbuchan, J.M. Measurement Science Conference Tutorial 1993/2000

159) Yu, D., Hsieh, H.Y. and Zemel (1993). 'Microchannel pyroelectric anemometer'. Sensors and Actuators A, 39 (1993) 29-35

Appendix A: Selected field data from temperature sensor strings

This section of the thesis presents some data, in graphical form, collected by the smart-sensor temperature strings described in Chapter 3.

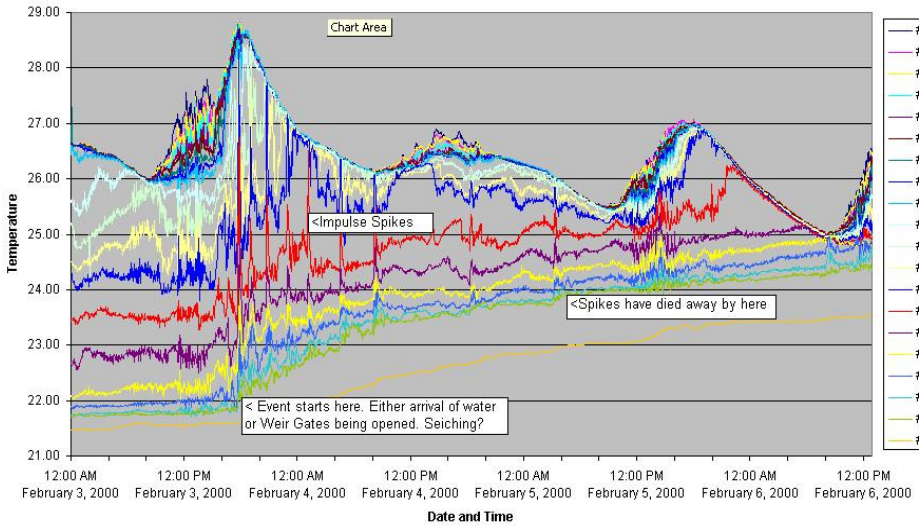

Figure 57. Evidence of 'seiching' in the Torrens Lake during a lake-flushing exercise. The inflow hit the dam wall, creating reflections

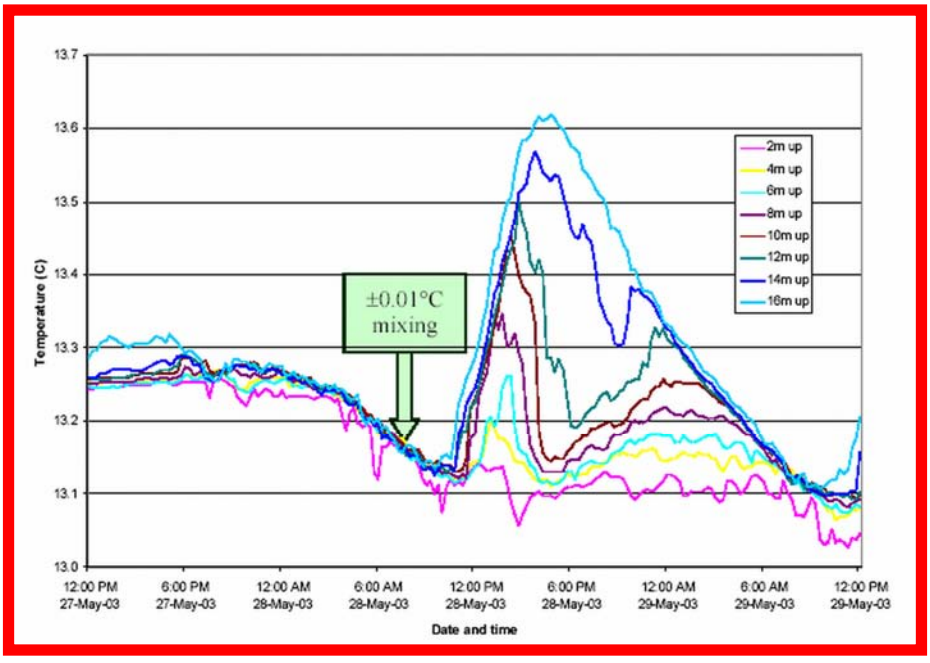

Figure 58. Evidence of 'sensor calibration consistency' in a 16m-water column. Data prior to sunrise on the 28th May 2003 indicated that the top 14m of the water column mixed to within 0.02°C, vindicating the level of matching (±0.01°C) attained during design and calibration. Systems deployed in the Murray River in June 2009 demonstrated matching over similar depths to within ±0.004°C

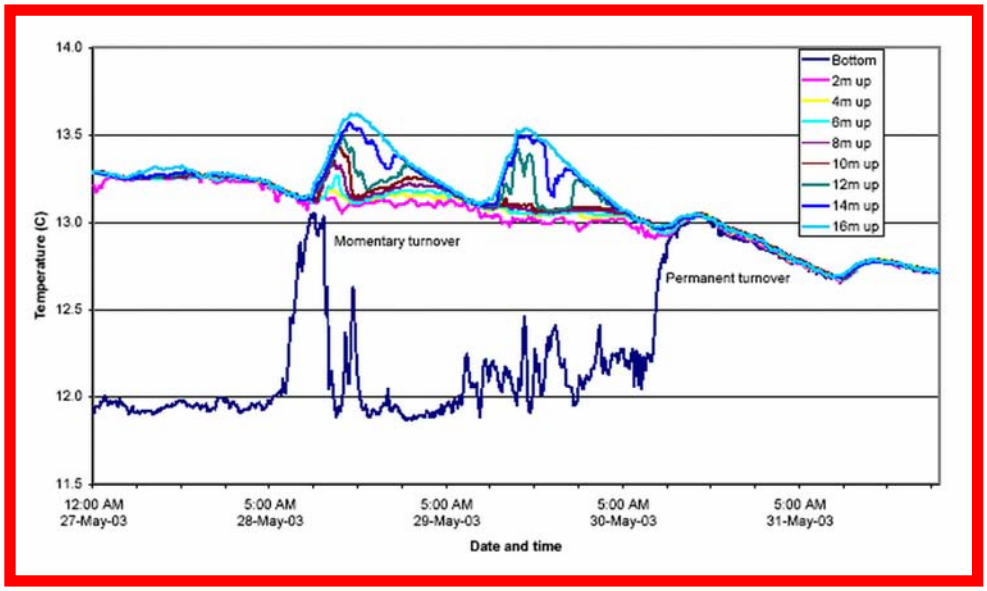

Figure 59. A 'turn-over' event in early autumn at the White Swan Reservoir in Ballarat Victoria. The bottom 2m of the water column is over 1°C cooler than the 14m water column above it. As the surface layers cool, their density increases and the water column becomes unstable, leading to complete mixing around dawn on the 30th May 2003.

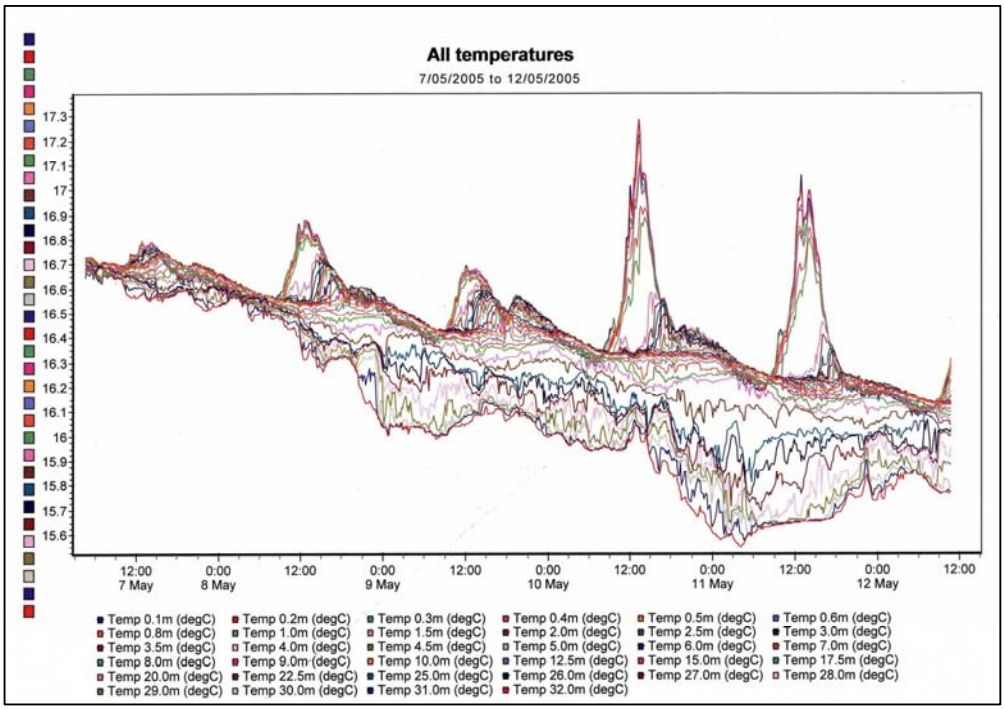

Figure 60. Evidence of a cold-water in-rush event from the catchment 'short-circuiting' the Happy Valley Reservoir by under-flowing the main water body. The 'curtain effect' of cooler waters at depth can be seen in the data on the sensors between 25m and 32m from midday on the 8th May 2005, reaching a peak around midnight on the 11th May 2005.

Figure 61 A radio-linked ship-to-shore buoy supporting a SDI-12 thermistor string. No data logging occurs on the buoy; instead, all data is transmitted immediately after each 15-minute measurement.

Figure 62 This Sealite buoy supports a full logging system, an integrated weather station capsule (Vaisala WXT-510) for air temperature, relative humidity, (drum-head) rainfall sensor, barometric pressure, ultrasonic wind speed and direction and separate global solar and net radiation sensors. All of these sensors are SDI-12 compatible, as is the electronic compass (seen through the instrument door) developed to give a local reference direction for the wind direction sensor. The data logger reads only SDI-12 sensors, and includes Next-G cellular-phone telemetry for remote data collection.

Figure 63 A spar-buoy supporting three separate thermistor strings having different anchoring arrangements to allow stratification monitoring in the epilimnion (surface layer), metalimnion (thermocline layer) and hypolimnion (bottom layer) of a reservoir, no matter how the water level changes. The perforated plate at the bottom of the buoy acts as a hydraulic damper to prevent the buoy 'bobbing' in rough water. The length of the chain wrapped around this damper plate is adjusted to change the flotation depth of the spar buoy, which sits low in the water (bottom, right) to allow correct operation of the net radiometer. The latter is part of the weather station cluster mounted on the buoy to monitor wind and solar energy. The station uses cellular phone long-haul telemetry and VHF ship-to-shore SCADA radio systems.

Appendix B: Binary logarithms for solving the Steinhart-Hart Equation

This appendix describes an attempt to simplify the calculation of temperature from thermistor resistance, for use in the very simple temperature sensors described in Chapter 3. It does this by replacing calculation-intensive *natural logarithms* in the Steinhart-Hart equation (Steinhart 1969) by an *approximation to a binary logarithm* involving simple arithmetic operators. This technique was obsoleted by the 'Method of Differences' described in Chapter 3, which in turn sprang out of this earlier work as a means of generating simple correction tables for reducing errors between approximated binary logarithms and true binary logarithms. The salinity sensor described in Chapter 4 used conventional floating-point arithmetic, as it's microcontroller suffered none of the restrictions in program memory space to be found in the simple temperature strings.

B1. Natural and binary logarithms

The natural logarithms used in the Steinhart-Hart equation are based on the constant e (2.71828182845904), just as base-10 logarithms are based on the constant 10. How are natural logarithms normally derived in a typical microcontroller at the heart of a sensor or instrument? To evaluate the traditional method, the smart temperature sensor was programmed with some existing maths code from a 32-bit floating-point maths library based on the Microchip Application Note AN660 (1997). These sensors worked well and gave the expected precision, accuracy field performance but the floating-point maths routines absorbed a very large part of the 2000-byte program code space of the sensor's microcontroller. An alternative algorithm is the subject of this Appendix. But before explaining the new technique derived, here is a brief overview of the standard method for calculating natural logarithms, based on AN660.

The effective domain of the natural log function is all positive number from 0 to the maximum number that can be represented in IEEE 754 32-bit floating point format, or 2E+128. There are some straightforward Taylor series approximations for this function: -

$$\ln(1+x) = \sum_{n=1}^{\infty} \frac{(-1)^{n+1}}{n} . x^n \text{ for } |x| < 1 \qquad \text{(B.1)}$$

or

$$\log_e x = (x-1) - \frac{1}{2}(x-1)^2 + \frac{1}{3}(x-1)^3 ... \qquad \text{(B.2)}$$

where (2>x>0)

However, these are not optimal for high performance function evaluation (AN660) because convergence is slow and computational demands are high as the order of the term's increases, accompanied by increasing loss of precision.

Instead, a technique known as "minimax approximation" is used, whereby a polynomial approximation of degree *n* to a continuous function can always be found such that the maximum error is a minimum, and that the maximum error must occur at least at *n+2* points with alternating sign within the interval of approximation. The great advantage in using the minimax approximations lies in the fact that minimizing the maximum error leads to the fewest number of terms required to meet a given precision. The number of terms is also dramatically affected by the size of the interval of approximation, leading to the concept of segmented representations, where the interval of approximation is split into sub-intervals, each with a dedicated minimax approximation.

For the 32-bit format, computation of the natural log is based on the alternative expansion: -

$$\ln x = \ln f + \ln 2^n = \ln f + n \cdot \ln 2 \tag{B.3}$$

where *n* is an integer and $0.5 \le f < 1$.

The final argument *z* is obtained through the additional transformation: -

$$z \equiv \begin{Bmatrix} 2f-1, n = n-1, f < 1/\sqrt{2}, \\ f-1, otherwise \end{Bmatrix} \tag{B.4}$$

naturally leading to a segmented representation of $\ln f = \ln(1+z)$ on the sub-intervals $\left[1/\sqrt{2}-1, 0\right]$ and $\left[0, \sqrt{2}-1\right]$, using the effectively constrained minimax form given by: -

$$\log_2(1+z) \approx z - 0.5 \cdot z^2 + z \cdot \left(z^2 \cdot \frac{p(z)}{q(z)} \right) \tag{B.5}$$

where *p(x)* is linear and *q(x)* is quadratic in *x*.

Without providing further detail, the conventional solution to solving the natural log of a number is non-trivial, code space intensive and requires typically 4800 to 5400 clock cycles to execute in the PIC16F628 microcontroller used in the temperature sensors. It is workable, but can it be improved upon?

Binary logarithms are based on the constant 2, and have the great advantage of simplicity of use in the world of binary arithmetic. Conversion from natural logarithms to binary logarithms of a resistance ***R*** can be readily achieved using the relationship: -

$$binaryLog(R) = \frac{naturalLog(R)}{naturalLog(2)} \tag{B.6}$$

i.e. $$\log_2 R = \frac{\ln R}{\ln 2} \quad \textbf{(91)}$$

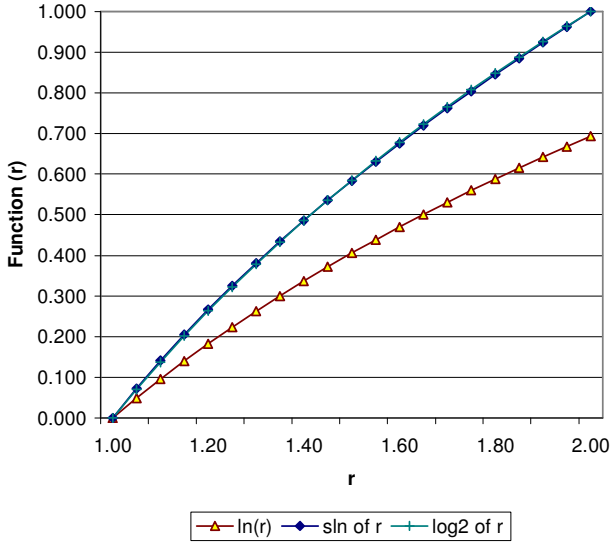

Figure 64 Comparison of natural (ln), binary (bln) and simple (sln) logarithms

Calculation of the binary log of a number in an Excel spreadsheets can use either this form, or more directly, the function "=log(R,2)"

Replacing the natural logarithm **ln(R)** in the simplified ***R-T*** thermistor equation with a binary logarithm **bln(R)** gives the following simplified relationship between thermistor temperature ***T*** and resistance ***R***, as used in Chapter 3:-

$$T(^0\mathrm{C}) = \frac{\mathrm{b}}{\mathrm{bln(R)} + \mathrm{c}} - d \qquad \text{(B.7)}$$

This substitution of binary logs for natural logs changes the values of the coefficients, but not the accuracy of the calculated temperature.

B2. Deriving binary logarithms in a microcontroller

Any integer number – such as the resistance ***R*** of a thermistor - can be expressed in the form: -

$$R(\Omega) = 2^P \times r \qquad \text{(B.8)}$$

where ***r*** is a number between 1 and 2, and ***P*** is an integer power of 2. Two is the base, while ***P*** is the integer part of the base 2 logarithm of ***R***.

If the binary log of a number is represented as ***bln(n)*** to distinguish it from the natural logarithm ***ln(n)***, then the binary log of the resistance ***R*** can be written as: -

$$\mathrm{bln(R)} = \mathrm{P} + \mathrm{bln(r)} \qquad \text{(B.8)}$$

A thermistor having a nominal resistance of 100kΩ at 25°C will have a resistance of 333kΩ at 0°C and 34.78kΩ at 50°C.

Because the sensor uses only 16-bit analog-to-digital conversion, it is convenient to restrict the resistance range to 16-bits (two bytes) as well. This is done by nominally dividing the resistance values for the thermistor and reset resistance by 4, and restricting the cold-end temperature range to a resistance of 4 x 65535Ω, or 4.7°C.

Thermistor resistances between 258300Ω/4=64575Ω and 42498Ω/4=10624Ω can be represented as per Eq. B.8 by: -

$64575(\Omega) = 2^{15} \times 1.970672607$ at 5°C

and $10624(\Omega) = 2^{13} \times 1.296875$ at 45°C.

In these two examples, ***P*** has the value of 15 and 13 respectively. Corresponding values of ***r*** are 1.970672607 and 1.296875. Note again that $1 \le r < 2$.

To extract ***P*** and ***r*** in a microcontroller [Cimbala 1996] the original two-byte value of resistance is right-shifted as many bits as needed, collecting the bits as they are shifted out, until the register that contained the original value is equal to 1. The number of "shifts" is equal to ***P***, and ***r*** is equal to 1 plus the fractional part that was shifted out. No arithmetic computations or lookup-tables have been required.

Take for example the (scaled) thermistor resistance of 30000Ω at 20.97°C - this can be represented in binary form by the two-byte value (30000_{dec} = 7530_{hex} = 0111 0101 0011 0000_{bin}):-

0	1	1	1	0	1	0	1	0	0	1	1	0	0	0	0	•	0	0	0	0	0	0	0	0	0	0	0	0	0	0	0
msb																														lsb	

where msb = most significant bit, lsb = least significant bit, • = decimal point

Just as in the decimal numbering system, the digits to the right of the decimal place represent the fractional part of the number (= 0 at the moment), but with binary weightings = 2^{-1}, 2^{-2}, 2^{-3}, 2^{-4}, = ½, ¼, etc.

To extract ***P*** and ***r***, the two-byte value of resistance is right-shifted 14-times until the register containing the original value is equal to 1, as follows: -

	→→→→→→→→→→→→→→																													
0	0	0	0	0	0	0	0	0	0	0	0	0	0	0	1	•	1	1	0	1	0	1	0	0	1	1	0	0	0	0	0
msb																														lsb	

The power term ***P*** is equal to 14, the number of right-shifts

The term **r** is equal to $1+\frac{1}{2}+\frac{1}{4}+\frac{1}{16}+\frac{1}{64}+\frac{1}{512}+\frac{1}{1024}=1.831054688$ from the fractional two-byte number to the right of the decimal point plus the integer 1 to the left of the decimal place. That is, 30000_{dec} can be represented as $2^{14} \times 1.831054688$

The number ***r*** can be seen to have a range from $1.0000\ 0000\ 0000\ 0000_{bin}$ to $1.1111\ 1111\ 1111\ 1111_{bin}$, or 1.000000000_{dec} to 1.999969482_{dec}, while the number ***P*** is clearly an integer value between 13 and 15 in this example

At this stage of the computation, the number ***r*** always has an integer portion = 1, and the number to the right of the decimal point is a 15-bit number in a two-byte (word) register. This word register has a range from 0 to 32768, because the two byte integer value for resistance can never be shifted more than 15 times, and still leave the ***msb*** in the ***lsb*** location. If the four-byte number is left shifted 15 times, the result is a 16-bit integer number equal to **r** multiplied by 32768 (2^{15}).

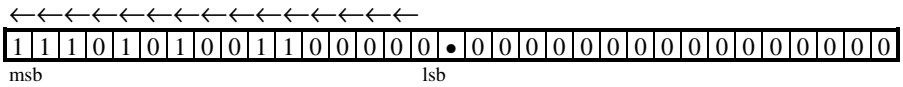

That is, $1.831054688 \times 2^{15} = 60000$. Corresponding values of ***r*** for 1.970672607 and 1.296875 are 64575 and 42496 respectively. The range of ***r*** is now 32768 to 65535 (2^{15} to 2^{16}-1).

The value ***P*** in the following calculations will therefore be 14, and the value of ***r*** will be 60000, which is a scaled integer with a multiplier of 32768 that has to be accounted for in the calculations. But first an explanation of the use of binary logarithms…

B3. Approximating the binary logarithm with a simple arithmetic function

Cimbala 1996 uses the lookup-table approach to derive the binary log of ***r*** using the fractional part of the value ***r*** as the pointer into the table.

However, a simple approximation of binary log functions was discovered while trying to fit various polynomial curves to the values of ***r*** between 1 and 2 in the binary logarithm, where: -

$$\boldsymbol{bln(R) = P + bln(r)} \tag{B.10}$$

The equation takes the form: -

$$binaryLog(R) \approx P + \frac{r}{2} - \frac{1}{r} + \frac{1}{2} = SimpleLog(R) = \mathrm{sln(R)} \tag{B.11}$$

When $r = 1$,

$$\frac{r}{2} - \frac{1}{r} + \frac{1}{2} = 0 \tag{B.12}$$

and when $r = 2$,

$$\frac{r}{2} - \frac{1}{r} + \frac{1}{2} = 1 \tag{B.13}$$

Note again that $1 \le r < 2$, $r = \frac{R(\Omega)}{2^P}$ and that ***r*** when plotted is a smooth function.

The value of this algorithm is its simplicity of calculation when using scaled integer arithmetic in a small 8-bit sensor microcontroller.

Multiplying ***r*** by 2^{15} allows it to fit into a two-byte number rather than work with awkward fractions. The range of ***r*** then moves from 1 to 2 to an integer range of 32768 to 65535 (as above).

Two of the three terms to be summed are easy to extract without needing arithmetic; **r/2** is obtained by a single right-shift of **r**, and ½ = 16384 when scaled up by 2^{15}.

The only real complexity is the inversion ***1/r***, which can be resolved in integer arithmetic by a division of a 4-byte number by the 2-byte value of ***r***.

The integer form of the equation can be expressed as follow: -

$$SimpleLog(R) = P + \frac{r}{2} - \frac{1}{r} + \frac{1}{2} \qquad \text{(B.14)}$$

where $0 \le P \le 15$ and $1 \le r < 2$

The value of ***r*** is scaled up from a fraction to an integer by multiplying it by 2^{15}, so the equation can be written in the form: -

$$SimpleLog(R) * 2^{15} = P * 2^{15} + \frac{r * 2^{15}}{2} - \frac{2^{15} * 2^{15}}{r * 2^{15}} + \frac{2^{15}}{2} \qquad \text{(B.15)}$$

B4. Solving for error terms in the Simple logarithm

A better understanding of the nature of the difference between the binary log and the Simple log is shown in Figure 65 below, which plots the difference between the two over the range *r=1 to 2*.

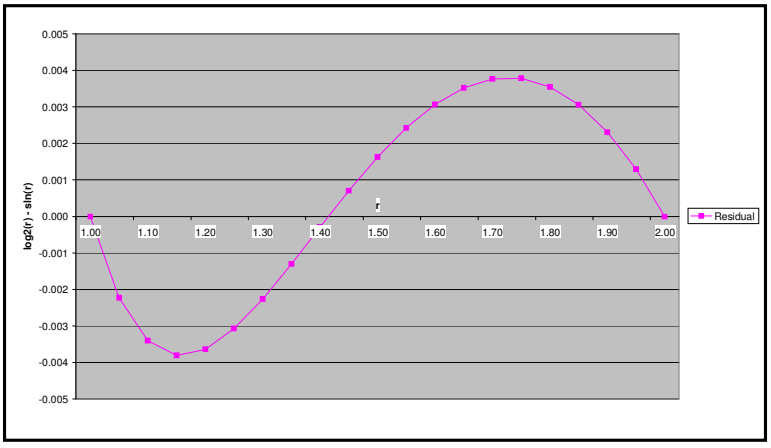

Figure 65 Residual errors between real natural logarithms and the 'Simple log' binary approximation

This s-shaped curvature error shows up later in the temperatures calculated using the Simple log, limiting temperature accuracy to +/-0.06°C.

Substituting the SimpleLog - sln(R) - in the simplified Steinhart-Hart equation:-

$$T(^0\mathrm{C}) = \frac{\mathrm{b}}{\mathrm{sln(R)} + \mathrm{a}} - c \qquad \text{(B.16)}$$

The small discrepancies between the binary logarithm and the Simple logarithm result in the errors in the calculated temperature of ±0.04°C shown in Figure 66 below: -

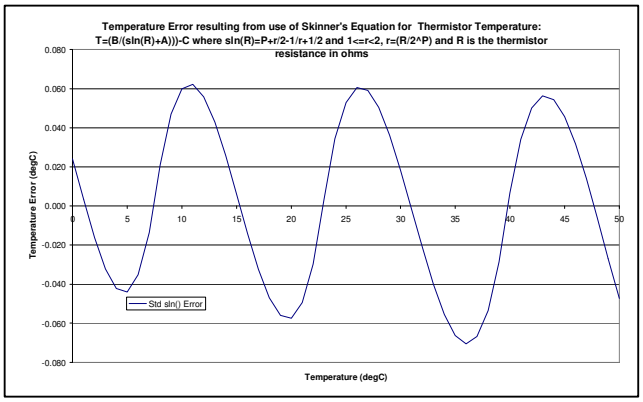

Figure 66 Temperature errors resulting from use of the Simple equation in the first order R-T curve

The cyclical nature of the error function of temperature above is a direct consequence of the error curve between ***sln(R)*** and ***bln(R)*** coupled with the incrementing of the ***P*** term from 13 to 15 as the resistance increases at lower temperatures.

B5. Using a look-up table to reduce errors in the Simple logarithm

The simplest way to reduce the errors between binary logs and Simple logs as shown in the figure above is to use a look-up table of (say) 128 values, covering the range of ***r*** from 1 to 2. A table having 128 values between 1 and 2 will increment ***r***-values in equal steps of 0.00781

These table values are easily calculated using Excel; the first few are shown in Table 1

TABLE 3 NATURAL, SIMPLE AND BINARY LOGARITHM TERMS IN THE RANGE 1 TO 2

r	ln(r)	sln(r)	bln(r)	Difference	Integer
1.00000	0.000	0.00000	0.00000	0.00000	114
1.00781	0.008	0.01166	0.01123	-0.00043	101
1.01563	0.016	0.02320	0.02237	-0.00083	89
1.02344	0.023	0.03462	0.03342	-0.00120	78
1.03125	0.031	0.04593	0.04439	-0.00153	68
1.03906	0.038	0.05713	0.05528	-0.00184	58

The ***Difference*** column is equal to the binary logarithm ***bln(r)*** minus the Simple logarithm ***sln(r)***, which is converted to a one-byte integer by multiplying it by 32768 (the factor used elsewhere in scaling fractions to integers). 128 is added (to convert the bipolar range to unipolar numbers between 0 and 127). This can be expressed as: -

$$BinaryLog(r) = SimpleLog(r) + Difference\_from\_LookupTable \qquad (B.17)$$

The range of ***r*** is 32768 to 65535 after it has been converted to an integer by multiplying it by 2^{15}, or 32768, so the pointer to the look-up table is found by subtracting 32768 from ***r*** and then dividing by 256. The latter step is a simple matter of using the most significant byte of $(r-32768)$ as the pointer – in binary arithmetic, this is equivalent to division by 256, just as knocking off three zeroes from the end of a large number is equivalent to dividing by 1000 in decimal notation.

For example, the thermistor resistance of 30000Ω represented as $2^{14} \times 1.831054688$ becomes $P = 14$, $r = 1.831054688 \times 2^{15} = 60000$. Then $(60000 - 32768)/256 = 234.375$, so the pointer into the correction table is 106, pointing to a value of 234. The table-centering offset of 128 must be subtracted from 234, so the final correction value is +106

Returning to the Simple log to convert it back to a binary logarithm: -

$$BinaryLog(R) * 2^{15} = P * 2^{15} + \frac{r * 2^{15}}{2} - \frac{2^{15} * 2^{15}}{r * 2^{15}} + \frac{2^{15}}{2} + Difference\_from\_LookupTable \qquad (B.18)$$

Substituting real values in the thermistor resistance example above gives: -

$$BinaryLog(30000) = (14 * 2^{15} + \frac{1.831054688 * 2^{15}}{2} - \frac{2^{15} * 2^{15}}{1.831054688 * 2^{15}} + \frac{2^{15}}{2} + 106)/2^{15} \qquad (B.19)$$

bln(30000) = 14.87267488 using bln(30000)=ln(30000)/ln(2)

bln(30000) = 14.87261962 using the corrected Simple logarithm described above

It can be seen that the result is correct to 4 decimal places.

Paper
Skinner, A.J. and Lambert, M.F. (2009). 'An arithmetic solution to the Steinhart-Hart Equation for thermistors.' IEEE Sensors, in submission, December 2009.

Appendix C: Thermistor Formulae in Excel Spreadsheets

Excel Visual Basic Macro FORMULAE used in thermistor calculations

```
'RT Converts 100R Thermistor Resistance into Temperature in degrees C

Function RT100(Resistance)
   aa = 0.0017709
   bb = 0.0003406
   cc = 0.0000001479
   RT100 = 1 / (aa + bb * Log(Resistance) + cc * Log(Resistance) ^ 3) - 273.15
End Function

'TR Converts 100R Thermistor Temperature in degrees C into Resistance ohms

Function TR100(Temperature)
   aa = 0.0017709
   bb = 0.0003406
   cc = 0.0000001479
   alpha = (aa - (1 / (Temperature + 273.15))) / cc
   beta = ((bb / (3 * cc)) ^ 3 + (alpha) ^ 2 / 4) ^ 0.5

   TR100 = Exp((beta - (alpha / 2)) ^ (1 / 3) - ((beta + (alpha / 2)) ^ (1 / 3)))
End Function
```

The same structure is used for other thermistors; only the coefficients aa, bb and cc change, as follows: -

```
'RT Converts 1000R Thermistor Resistance into Temperature in degrees C
   aa = 0.001313
   bb = 0.0002906
   cc = 0.0000001023

'RT Converts 2252R Thermistor Resistance into Temperature in degrees C
   aa = 0.00147419
   bb = 0.0002371
   cc = 0.0000001077

'RT Converts 3000R Thermistor Resistance into Temperature in degrees C
   aa = 0.0014051
   bb = 0.0002369
   cc = 0.0000001019

'RT6 Converts 6000R Thermistor Resistance into Temperature in degrees C
   aa = 0.0012474
   bb = 0.000235
   cc = 0.00000009466

'RT30000 Converts 30000R Thermistor Resistance into Temperature in degrees C
   aa = 0.0009354
   bb = 0.0002211
   cc = 0.0000001275
'RT100k Converts 100k Thermistor Resistance into Temperature in degrees C
```

```
aa = 8.43643767950071E-04
bb = 2.02100835064118E-04
cc = 1.20314377529985E-07
    RT100k = 1 / (aa + bb * Log(resistance) + cc * Log(resistance) ^ 3) - 273.15
End Function
```

Appendix D: Failure of Monotonicity in the ADC

Further development of the charge-balance analog-to-digital converter after publication of the paper derived from Chapter 3 sought to correct for 'flat-spots' in the temperature response curve at the higher-end of the operating temperature range above that used in the field work. Monotonic output of an analog-to-digital converter guarantees that – in the case of the temperature sensor described in Chapter 3 – a very slowly varying temperature will generate one count after another in perfect numerical order. The count never doubles back on itself, skips a count or two, or develops 'flat spots' where a particular count repeats itself before the progression picks up again as though nothing had happened. In 'temperature-drift' tests, 21 sensors were logged as room temperature fluctuated slowly. Monotonicity was perfect, according to the principles of uniform count progression and uni-directionality until a 'flat spot' appeared in all sensors at a count value of 13107, although at slightly different temperatures for each sensor, and consistently within a range of +/-7 counts of the value 13107.

Firmware checks confirmed that this particular phenomenon was not an artefact of the conversion of counts-to-serial data transmitted to the logger, so the focus shifted back to the hardware. Of particular note was the relationship between this count 13107 and the total count 65536: a ratio of exactly 5 to 1. To test the hardware, a high-stability resistor chain in series with a small value trimmer resistor was fitted to the sensor in place of the thermistor such that counts could be trimmed in this range. A 20MHz oscilloscope was used to view the charge-balance circuitry throughout the count range where the 'flat-spot' occurred, and the sensor firmware modified slightly to keep the ADC in operation so that long-term diagnosis of the problem could be carried out.

What showed up was a small 'glitch' on the integrator output ramp at the moment the ramp crossed the comparator threshold. This took the form of a ringing damped sine wave 2μs long and 100mV peak to peak. Of particular note was that this occurred at the comparator triggering point, which coincided exactly with the negative edge of the SVFC clock. This is the point where the microcontroller 'samples' the comparator input. The conclusion was that sampling of the comparator output by the microcontroller was occurring at exactly the same moment that the comparator output was switching from low to high, and where it's output is indeterminate. The SCFV clock and the comparator switching point where perfectly synchronized. Whatever is happening inside the microcontroller's input pin – looking out at an input that is changing state – the net result

is a decision to report the bit state in such a way that the output count 'locks' onto a particular value, equal to 1/5 of the clock. That is, the integrator's sawtooth output is a sub-harmonic of the sampling clock. This suggests that a similar problem will occur at other sub-harmonics (1/4, 1/3, ½, 1/6, 1/7, etc.)

Table 4 Sub-harmonics of the SVFC clock causing temperature 'flat-spots'

Sub-harmonic	Count	Temperature
2	32768	44.26
3	21845	33.61
4	16384	26.40
5	13107	20.97
6	10923	16.65
7	9362	13.05
8	8192	9.99
9	7282	7.31
10	6554	4.94
11	5958	2.82
12	5461	0.89
13	5041	-0.87

The mechanism proposed for this failure was based on the theory that a perturbation on the power supply lines to the LM392 op-amp/comparator when the comparator switched was feeding back into the op-amp and appearing at its output, which further triggered oscillations in the comparator output. No evidence of this positive feedback was evident in the comparator output, although this may well have been due to the limitations of a 20MHz analog oscilloscope. Attempts to defeat this problem in hardware failed; these included additional filtering on supply lines and references, switching the comparator output to the active (rather then the open-collector) edge, and adding hysteresis to the comparator. The most probable explanation lies in the highly non-linear nature of a high-gain comparator as it passes briefly through the linear region at the switching point. The input impedance of its inputs can change momentarily, which effectively sucks a small amount of charge out of the integrator capacitor of the previous stage, resulting in the 2µs ringing on the (integrator) op-amp output. This charge can be amplified significantly by the Miller-effect and the high-gain of the first stage of the comparator.

This failure of monotonicity – although small – led to the redesign of the temperature sensor in order to separate the op-amp and comparator; this meant elimination of the LM392. Instead, a single op-amp was used in the integrator circuit, and the on-board comparator inside the microcontroller was used. The comparator set point from the ADC bridge circuit is applied through an appropriate microcontroller pin. This

effectively cured the problem; later versions of the sensor (after IEEE Sensors paper was published) had perfectly monotonic outputs.

Appendix E: Sap Flow Bibliography

(Courtesy of Professor Brian Loveys – CSIRO Plant Industry)

1) Antolín MC, Ayari M, Sánchez-Díaz M (2006) 'Effects of partial rootzone drying on yield, ripening and berry ABA in potted Tempranillo grapevines with split roots'. Australian Journal of Grape and Wine Research 12, 13-20.

2) Augé RM, Moore JL (2002) 'Stomatal response to non-hydraulic root-to-shoot communication of partial soil drying in relation to foliar dehydration tolerance'. Environmental and Experimental Botany 47, 217-229.

3) Baker JM, van Bavel CHM (1987) 'Measurement of mass flow of water in stems of herbaceous plants'. Plant, Cell and Environment 10, 777-782.

4) Begg JE, Turner NC (1970) 'Water potentials gradients in field tobacco'. Plant Physiology 46, 343-346. Journal of Experimental Botany 57, 3283-3291.

5) Braun P, Schmid J (1999) 'Sap flow measurements in grapevines (Vitis vinifera L.). Stem morphology and use of the heat balance method.' Plant and Soil 215, 39-45.

6) Bravdo, B. and Naor, A. (1996) 'Effect of water regime on productivity and quality of fruit and wine.' Acta Horticulturae 427, 15-26.

7) Burgess SSO, Bleby TM (2006) 'Redistribution of soil water by lateral roots mediated by stem tissues.' Journal of Experimental Botany 57, 3283 -3291.

8) Brookes JR, Meinzer C, Coulombe R, Gregg J (2002) 'Hydraulic redistribution of soil water during summer drought in two contrasting Pacific Northwest coniferous forests.' Tree Physiology 22, 1107-1117.

9) Caldwell MM, Dawson TE, Richards, JH (1998) 'Hydraulic lift: consequences of water efflux from the roots of plants'. Oecologia 113, 151-161.

10) Calò A, Giorgessi F, Sansone L, Tomasi D, Zerbi G (1999) Recherches sur le rapport entre le flux de sève, la transpiration et la vigueur dans la vigne selon le mode de conduite'. Vitis 38, 7-13.

11) Choné, X, Van Leeuwen C, Dubourdieu D, Gaudillère JP (2001) 'Stem water potential is a sensitive indicator of grapevine water status'. Annals of Botany 87, 477-483.

12) Collins M, Fuentes, S, Barlow S (2005) 'Water-use of grapevines to PRD irrigation at two water levels. A case study in North- Eastern Victoria'. Australian and New Zealand Grapegrower &Winemaker 502, 41-45.

13) Comstock JP (2002) 'Hydraulic and chemical signalling in the control of stomatal conductance and transpiration'. Journal of Experimental Botany 53, 195-200.

14) Correia, MJ, Pereira, JS (1995) 'Absicisic acid in apoplastic sap can account for the restriction in leaf conductance of white lupins during moderate soil drying and after rewatering'. Plant, Cell and Environment 17, 845-852.
15) Correia, MJ, Pereira, JS, Chaves, MM, Rodrigues, ML, Pacheco, CA (1995) 'ABA xylem concentrations determine maximum daily leaf conductance of field-grown Vitis vinifera L. plants'. Plant, Cell and Environment 18, 511-521.
16) Davies WJ, Tardieu F, Trejo CL (1994) 'How do chemical signals work in plants that grow in drying soil'. Plant Physiology 104, 309-314.
17) De Lorenzi, Rana G (2000) 'Sap flow transpiration measurements in a table grape vineyard growing in Southern Italy'. Acta Horticulturae, 537, 69-75.
18) Dodd IC, Stikic R, Davies WJ (1996) 'Chemical regulation of gas exchange and growth of plants in drying soil in the field'. Journal of Experimental Botany 47, 1475-1490.
19) Dodd IC, Theobald JC, Bacon MA, Davies WJ (2006) 'Alternation of wet and dry sides during partial rootzone drying irrigation alters root-to-shoot signalling of abscisic acid'. Functional Plant Biology 33, 1081-1089.
20) Dorji K, Behboudian MH, Zegbe-Domínguez JA (2005) 'Water relations, growth, yield, and fruit quality of hot pepper under deficit irrigation and partial rootzone drying'. Scientia Horticulturae 104, 137-149.
21) Dry PR, Loveys BR, (1999) 'Grapevine shoot growth and stomatal conductance are reduced when part of the root system is dried'. Vitis 38, 151-156.
22) Dry PR, Loveys BR, During H (2000 a) Partial drying of the rootzone of grape. I
23) Transient changes in shoot growth and gas exchange.Vitis 39, 3-7.
24) Dry PR, Loveys BR, During H (2000 b) 'Partial drying of the rootzone of grape. II. Changes in the patterns of root development'. Vitis, 39, 9-12.
25) Du T, Kang S, Zhang J, Li F, Hu X (2006) 'Yield and physiological responses of cotton to partial root-zone irrigation in the oasis field of northwest China'. Agricultural Water Management 84, 41-52.
26) Düring H, Dry PR (1995) 'Osmoregulation in water-stressed roots- responses of leaf conductance and photosynthesis'. Vitis, 34 (1), 15-17.
27) Escalona JM, Gulías J, Medrano H (1999) 'Daily and seasonal sap flow (SHB) in irrigated and non-irrigated Tempranillo grapevines'. Proceedings 11th GESCO Meeting, Sicília, Itália, pp 316-322.

28) Eastham J, Gray SA (1998). 'A preliminary evaluation of the suitability of sap flow sensors for use in scheduling vineyard irrigation'. American Journal Enology and Viticulture 49 (2), 171-176.

29) Fuchs EE, Livingston NJ (1996) 'Hydraulic control of stomatal conductance in Douglas fir [Pseudotsuga menziesi (Mirb.) Franco and alder [Alnus rubra (Bong)] seedlings'. Plant, Cell and Environment 19, 1091-1098.

30) Green SR, Clothier BE, McLeod DJ (1997). 'The response of sap flow in apple roots to localised irrigation'. Agricultural Water Management 33, 63-78.

31) Ginestar C, Eastham J, Gray S, Iland P (1998) 'Use of sap-flow sensors to schedule vineyard irrigation. Effects of post-veraison water deficits on water relations, vine growth, and yield of Shiraz grapevines'. American Journal Enology and Viticulture 49(4), 413-420.

32) Gollan T, Passioura JB, Munns R (1986) 'Soil-water status affects the stomatal conductance of fully turgid wheat and sunflower leaves'. Australian Journal of Plant Physiology 13, 459-464.

33) Gowing DJG, Davies, WJ, Jones HG (1990) 'A positive root-sourced signal as an indicator of soil drying in apple, Malus domestics Borkh.'. Journal of Experimental Botany 41, 1535- 1540.

34) Gu SL, Du GQ, Zoldoske D, Hakim A, Cochran R, Fugelsang K, Jorgensen G (2004) 'Effects of irrigation amount on water relations, vegetative growth, yield and fruit composition of Sauvignon blanc grapevines under partial rootzone drying and conventional irrigation in the San Joaquin Valley of California, USA'. Journal of Horticultural Science & Biotechnology. 79 (1), 26-33.

35) Hansen H and Dorffling K (2003) 'Root-derived trans-zeatin riboside and absisic acid in drought-stressed and rewatered sunflower plants: interaction in the control of leaf diffusive resistance?' Functional Plant Biology 30, 365-375.

36) Hartung W, Wilkinson S, Davies WJ (1998) 'Factors that regulate absicisic acid concentrations at the primary site of action at the guard cell'. Journal of Experimental Botany 51, 361-367.

37) Hartung W, Slovik S (1991) 'Physicochemical properties of plant growth regulators and plant tissues determine their distribution and redistribution: stomatal regulation by abscisic acid in leaves'. The New Phytologist 119, 361-382.

38) Jia W, Davies WJ (2007) 'Modification of leaf apoplastic pH in relation to stomatal sensitivity to root-sourced abscisic acid signals'. Plant Physiology 143, 68-77.

39) Kang S, Liang Z, Pan Y, Shi P, Zhang J (2000) 'Alternate furrow irrigation for maize production in an arid area'. Agricultural Water Management 45, 267-274.
40) Kang S, Shi W, Cao H, Zhang J (2002) 'Alternate watering in soil vertical profile improved water use efficiency of maize (Zea mays)'. Field Crops Research 77, 31-41.
41) Kang S, Hu, X., Jerie, P, Zhang J. 2003. 'The effects of partial rootzone drying on root, trunk flow and water balance in an irrigated pear (Pyrus communis L.) orchard.' Journal of Hydrology, 280, 192-206.
42) Khalil AM, Grace J 1993. 'Does xylem sap ABA control the stomatal behaviour of water stressed Sycamore (Acer pseudoplatanus L.) seedlings?' Journal of Experimental Botany 44, 1127-1134.
43) Lascano RJ, Baumhardt RL, Lipe WN (1992) 'Measurement of water flow in young grapevines using the stem heat balance method'. American Journal of Enology and Viticulture 43, 159-165.
44) Liang J, Zhang J, Wong MH (1997) 'How do roots control xylem sap ABA concentration in response to soil drying?' Plant, Cell and Physiology 38, 10-16.
45) Liu F, Jensen CR, Andersen MN (2003) 'Hydraulic and chemical signals in the control of leaf expansion and stomatal conductance in soybean exposed to drought stress'. Functional Plant Biology 30, 65-73.
46) Liu F, Shahnazari A, Andersen MN, Jacobsen S, Jensen CR (2006) 'Physiological responses of potato (Solanum tuberosum L.) to partial root-zone drying: ABA signalling, leaf gas exchange and water use efficiency'. Journal of Experimental Botany 57, 3327-3735.
47) Loveys BR, Dry PR, Stoll M, McCarthy MG (2000) 'Using plant physiology to improve the water use efficiency of horticultural crops'. Acta Horticulturae 537, 187-197.
48) Loveys BR, Stoll M, Davies WJ (2004) 'Physiological approaches to enhance water use efficiency in agriculture: exploiting plant signalling in novel irrigation practice'. In: Bacon MA, ed. Water use efficiency in plant biology. Oxford: Blackwell Publishing, 113-141.
49) Lovisolo C, Hartung W, Schubert A (2002) 'Whole-plant hydraulic conductance and root-to-shoot flow of abscisic acid are independently affected by water stress in grapevines'. Functional Plant Biology 29, 1349-1356.
50) Lovisolo C, Schubert A (2006) 'Mercury hinders recovery of shoot hydraulic conductivity during rehydration: evidence from a whole-plant approach'. New Phytologist 172 (3), 469-478.

51) Lovisolo C, Schubert A (1998) ‘Effects of water stress on vessel size and xylem hydraulic conductivity in Vitis vinifera L.’ Journal of Experimental Botany 49, 693-700.
52) Lovisolo C, Schubert A, Peterlunger E, Ferraris S (2000) ‘Sap flow and stem conductivity of potted water stressed grapevines’. Acta Horticulturae, 526, 187-190.
53) Lu P, Yunusa IAM, Walker RR, Müller WJ (2003) ‘Regulation of canopy conductance and transpiration and their modelling in irrigated grapevines’. Functional Plant Biology 30, 689-698.
54) Martre P, Morillon R, Barrieu F, North GB, Nobel PS, Chrispeels MJ (2002) ‘Plasma membrane aquaporins play a significant role during recovery from water deficits’. Plant Physiology 130, 2101-2110.
55) McCarthy MG (1997) ‘The effect of transient water deficit on berry development of Shiraz (Vitis vinifera L.)’. Australian Journal of Grape and Wine Research 3,102-108.
56) McCarthy MG, Loveys BR, Dry PR, Stoll M (2002) ‘Regulated deficit irrigation and partial rootzone drying as irrigation management techniques for grapevines’. In: Deficit irrigation practices, FAO Water Reports, Rome, Italy, No. 22, 79-87.
57) Mingo DM, Theobald JC, Bacon MA, Davies WJ, Dodd, IC (2004) ‘Biomass allocation in
58) tomato (Lycopersicon esculentum) plants grown under partial rootzone drying: enhancement of root growth’. Functional Plant Biology 31, 971-978.
59) Netting AG, Windsor, ML, Milborrow BV (1997) ‘Endogenous biosynthetic precursors of (+) abscisic acid’. III Incorporation of 2H2O from 18O2 into precursors. Australian Journal of Plant Physiology 24, 175-184.
60) Patakas A, Noitsakis B (1999) ‘Osmotic adjustment and partitioning of turgor responses to drought in grapevines leaves’. American Journal Enology and Viticulture 50 (1), 76-80.
61) Poni S, Tagliavini M, Neri D, Scudellari D, Toselli M (1992) ‘Influence of root pruning and water stress on growth and physiological factors of potted apple, grape, peach and pear trees’. Scientia Horticulturae 52, 223-236.
62) Possingham, JV (2000) ‘The influence of controlled water inputs on grape quality in warm regions’. Proceedings XXVeme Congrès Mondial da la Vigne et du Vin, 63- 68.
63) Prichard, T.L. (1992) ‘A volume balance approach to quality wine grape irrigation. In: 'Viticultural Practices'. Eds. M.A.Walker and W.M. Kliewer (Univ.California, Davies) pp. 12-23.

64) Prokic L, Jovanovic Z, McAinsh MR, Vucinic Z, Stikic, R (2006) 'Species-dependent changes in stomatal sensitivity to absicisic acid mediated by external pH'. Journal of Experimental Botany 57 (3), 675-683.

65) Ren H, Gao Z, Chen L, Wei K, Liu J, Fan Y, Davies WJ, Jia W, Zhang J (2007) 'Dynamic analysis of ABA accumulation in relation to the rate of ABA catabolism in maize tissues under water deficit'. Journal of Experimental Botany 58 (2), 211-219.

66) Rodrigues, M.L., Chaves, M.M., Wendler, R., David, M.M., Quick, P., Leegood, R., Stitt, M., Pereira, J.S., (1993). 'Osmotic adjustment in water stressed grapevine leaves in relation to carbon assimilation'. Australian Journal of Plant Physiology, 20, 309-321.

67) Sakuratani T, Aoe T, Higuchi H (1999) 'Reverse flow in roots of Sesbania rostrata measured using the constant power heat balance method'. Plant, Cell and Environment 22, 1153-1160.

68) Saliendra NZ, Sperry JS, Comstock J (1995) 'Influence of leaf water status on stomatal response to humidity, hydraulic conductance, and soil drought in Betula occidentalis'. Planta 196, 357-366.

69) Santos T, Lopes C, Rodrigues ML, Souza CR, Silva JR, Maroco JP, Pereira JS, Chaves MM (2003) 'Partial rootzone drying effects on growth and fruit quality of field-grown grapevines (Vitis vinifera)'. Functional Plant Biology 30, 663-671.

70) Santos T, Lopes C, Rodrigues ML, Souza CR, Silva JR, Maroco JP, Pereira JS, Chaves MM.(2005) 'Effects of partial root-zone drying irrigation on cluster microclimate and fruit composition of Castelão field-grown grapevines'. Vitis 44 (3), 117-125.

71) Santos T, Lopes C, Rodrigues ML, Souza CR, Silva JR, Maroco JP, Pereira JS, Chaves MM. (2007) 'Effects of deficit irrigation strategies on cluster microclimate for improving fruit composition of Moscatel field-grown grapevines'. Scientia Horticulturae 112, 321-330.

72) Sauter A, Dietz KJ, Hartung W (2002) 'A possible stress physiological role of abscisic acid conjugates in root-to-shoot signalling. Plant, Cell and Environment 25, 223-228.

73) Schmid J, Schultz HR (2000) 'Influence of two training systems and irrigation on water consumption of grapevines in the field'. Acta Horticulturae 537, 587-595.

74) Schultz HR (2000) 'Climate change and viticulture: a European perspective on climatology, carbon dioxide and UV-B effects'. Australian Journal of Grape and Wine Research. 6, 2-12.

75) Schultz HR (2003) 'Differences in hydraulic architecture account for near-isohydric and anisohydric behaviour of two field-grown Vitis vinifera L. cultivars during drought'. Plant, Cell and Environment 26, 1393-1405.

76) Shashidhar VR, Prasad TG, Sudharshan L (1996) 'Hormonal signals from roots to shoots of sunflower (Helianthus annuus L.). Moderate soil drying increases delivery of absicisic acid and depresses delivery of cytokinins in the xylem sap'. Annals of Botany 78, 151-155.

77) Siefritz F, Tyree MT, Lovisolo C, Schubert A, Kaldenhoff R (2002) 'PIP1 Plasma membrane aquaporins in tobacco: from cellular effects to function in plants'. The Plant Cell 14, 869-876.

78) Smart DR, Carlisle E, Goebel M, Núñez BA (2005) 'Transverse hydraulic redistribution by a grapevine'. Plant, Cell and Environment 28, 157-166.

79) Soar CJ, Speirs J, Maffei SM, Loveys BR (2004) 'Gradients in stomatal conductance, xylem sap ABA and bulk leaf ABA along canes of Vitis vinifera cv. Shiraz: molecular and physiological studies investigating their source'. Functional Plant Biology 31, 659-669.

80) Soar CJ, Speirs J, Maffei SM, Penrose AB, McCarthy MG, Loveys BR (2006) 'Grape vine varieties Shiraz and Grenache differ in their stomatal response to VPD: apparent links with ABA physiology and gene expression in leaf tissue'. Australian Journal of Grape and Wine Research 12, 2-12.

81) Sobeih WY, Dodd IC, Bacon MA, Grierson D, Davies, WJ (2004) 'Long-distance signals regulating stomatal conductance and leaf growth in tomato (Lycopersicon esculentum) plants subjected to partial rootzone drying'. Journal of Experimental Botany 55, 2353- 2363.

82) Souza, C., Maroco J, Santos, T, Rodrigues ML, Lopes C, Pereira JS, Chaves MM (2005) 'Control of stomatal aperture and carbon uptake by deficit irrigation in two grapevine cultivars'. Agriculture, Ecosystems and Environment 106, 261-274.

83) Steppe K, Lemeur R. (2004) 'An experimental system for analysis of the dynamic sap flow characteristics in young trees: results of a beech tree'. Functional Plant Biology 31, 83-92.

84) Stoll M, Loveys B, Dry P (2000) 'Hormonal changes induced by partial rootzone drying of irrigated grapevine'. Journal of Experimental Botany 51, 1627-1634.

85) Tarara JM, Ferguson JC (2001) 'Device for simulating high rates of sap flow in grapevines'. American Journal Enology Viticulture 52, 260-265.

86) Tardieu F, Davies WJ (1992) 'Stomatal responses to abscisic acid is a function of current plant water status'. Plant Physiology 98, 540-545.

87) Tardieu 1 F, Zhang J, Gowing DJG (1993) 'Stomatal control of both [ABA] in the xylem sap and leaf water status: a test of a model for droughted or ABA-fed field-grown maize'. Plant, Cell and Environment 16, 413-420.

88) Tardieu F, Lafarge T, Simonneau T (1996) 'Stomatal control by fed or endogenous xylem ABA in sunflower interpretation of correlations between leaf water potential and stomatal conductance in anisohydric species'. Plant, Cell and Environment 19, 75-84.

89) Trejo CL, Clephan AL, Davies WJ (1995) 'How do stomata read abscisic acid signals?' Plant Physiology 109, 803-811.

90) Trejo CL, Davies WJ, Ruiz L (1993) 'Sensitivity of stomata to abscisic acid. An effect of the mesophyll'. Plant Physiology 102, 497-502.

91) Zhang J, Schurr U, Davies WJ (1987) 'Control of stomatal behaviour by abscisic acid, which apparently originates in the roots'. Journal of Experimental Botany 38, 1174-1181.

92) Wakrim R, Wahbi S, Tahi H, Aganchich B, Serraj R (2005) 'Comparative effects of partial root drying (PRD) and regulated deficit irrigation (RDI) on water relations and water use efficiency in common bean (Phaseolus vulgaris L.)'. Agriculture, Ecosystems and Environment 106, 275-287.

93) Wample RL, Smithyman R (2002) 'Regulated deficit irrigation as a water management strategy in Vitis vinifera production'. Water Reports, FAO Publication number 22, Rome, pp. 89-101.

94) Wilkinson S, Davies WJ (1997) 'Xylem sap pH increase: a drought signal received at the apoplastic face of the guard cell that involves the suppression of saturable abscisic acid uptake by the epidermal symplast'. Plant Physiology 113, 559-573.

95) Wilkinson S, Davies WJ (2002) 'ABA-based chemical signalling: the co-ordination of responses to stress in plants'. Plant, Cell and Environment 25, 195-210.

96) Wilkinson S (2004) 'Water use efficiency and chemical signalling'. In MA Bacon ed., Water Use efficiency in Plant Biology. Blackwell Publishing CRC Press, pp 75-112.

97) Williams LE, Ayars JE (2005) 'Grapevine water use and the crop coefficient are linear functions of the shaded area measured beneath the canopy'. Agricultural and Forest Meteorology 132, 201-211.

98) Yunusa IAM, Walker RR, Loveys BR, Blackmore DH (2000) 'Determination of transpiration in irrigated grapevines: comparison of the heat-pulse technique with gravimetric and micrometeorological methods'. Irrigation Science 20, 1-8.